

Electronic Thesis and Dissertation Repository

---

8-20-2018 2:30 PM

## Vibrating-wire Rheometry

Cameron C. Hopkins, *The University of Western Ontario*

Supervisor: de Bruyn, John R., *The University of Western Ontario*

A thesis submitted in partial fulfillment of the requirements for the Doctor of Philosophy degree in Physics

© Cameron C. Hopkins 2018

Follow this and additional works at: <https://ir.lib.uwo.ca/etd>



Part of the [Statistical, Nonlinear, and Soft Matter Physics Commons](#)

---

### Recommended Citation

Hopkins, Cameron C., "Vibrating-wire Rheometry" (2018). *Electronic Thesis and Dissertation Repository*. 5584.

<https://ir.lib.uwo.ca/etd/5584>

This Dissertation/Thesis is brought to you for free and open access by Scholarship@Western. It has been accepted for inclusion in Electronic Thesis and Dissertation Repository by an authorized administrator of Scholarship@Western. For more information, please contact [wlsadmin@uwo.ca](mailto:wlsadmin@uwo.ca).

## Abstract

This thesis consists of two projects on the behaviour of a novel vibrating-wire rheometer and a third project studying the gelation dynamics of aqueous solutions of Pluronic F127. In the first study, we use COMSOL to perform two-dimensional simulations of the oscillations of a wire in Newtonian and shear-thinning fluids. Our results show that the resonant behaviour of the wire agrees well with the theory of a wire vibrating in Newtonian fluids. In shear-thinning fluids, we find resonant behaviour similar to that in Newtonian fluids. In addition, we find that the shear-rate and viscosity in the fluid vary significantly in both space and time. We find that the resonant behaviour of the wire can be well described by the theory of a wire vibrating in a Newtonian fluid if the viscosity in the theory is set equal to the viscosity averaged over the circumference of the wire and over one period of the wire's oscillation at the resonant frequency. In the second study, we present the design and operation of our vibrating-wire rheometer and use it to measure the properties of Newtonian and viscoelastic fluids. We find that our device can accurately measure small viscosities. In homogeneous polymer solutions, we find that the viscoelastic moduli measured using our device are consistent with measurements at lower frequencies using a shear rheometer. In addition, we find that our device can measure the microrheological properties of an aging Laponite clay suspension that is heterogeneous on the micron scale. In the third project, we study the gelation dynamics of aqueous solutions of Pluronic F127. Using shear rheometry we find that when slowly heating the solutions, they undergo a transition from sol to gel around room temperature, followed by a gel to sol transition at a higher temperature. Our results show that these transitions take place over a temperature range of a few degrees. When cooling the solutions, the reverse transitions occur over a larger range of temperature and the width in temperature of the gel phase is larger. At temperatures near the phase transitions, we find that the rheological relaxation time becomes very long.

**Keywords:** Rheology, rheometry, viscometry, vibrating wire, complex fluids, Pluronic, COMSOL

## Co-Authorship Statement

Chapter 2 has been published as: Cameron C. Hopkins and John R. de Bruyn, Vibrating Wire Rheometry, *Journal of Non-Newtonian Fluid Mechanics*, **238**, 2016. I did all of the experiments, data analysis and writing of early drafts of the paper. John R. de Bruyn supervised the project and provided editorial comments on the paper.

A version of chapter 3 is being prepared for submission. I did all of the simulations, data analysis, and writing of the early drafts of the paper. John R. de Bruyn supervised the project and provided editorial comments.

A version of chapter 4 will be submitted for publication in the *Journal of Rheology*. I did all of the experiments, data analysis, and writing of the early drafts of the paper. John R. de Bruyn supervised the project and provided editorial comments.

# Acknowledgments

First, I must thank my advisor, Dr. John R. de Bruyn. I have grown considerably, both personally and professionally, over my time here in no small part thanks to his mentorship and patience. His guidance over the years has shaped me into an effective scientist. I feel like I am well prepared for a future in science thanks to him.

I gratefully acknowledge the funding received towards my PhD from the National Sciences and Engineering Research Council, Ontario Graduate Scholarship, University of Western Ontario, and the Canada Foundation for Innovation.

The work in chapter 3 was made possible by the facilities of the Shared Hierarchical Academic Research Computing Network (SHARCNET:www.sharcnet.ca) and Compute/Calcul Canada, and the provision of the COMSOL Multiphysics license by CMC Microsystems.

I am grateful for the guidance my advisory committee, Dr. Silvia Mittler and Dr. Michael G. Cottom, have given me over the years.

Frank Van Sas and Brian Dalrymple manufactured the parts for my vibrating-wire rheometer, and Doug Hie helped develop the electronics. Without their expertise this project would not have been possible.

I want to thank fellow graduate student Nirosh Getangama, and former colleagues Yang Liu and Masha Goiko, for their helpful discussions over the course of my PhD.

Thank you to my parents and brother for their unconditional support and encouragement over the duration of my studies.

Finally, I must thank my wife, Ellie, for her unwavering support and patience over the last year. I would not have been able to do this without her.

# Contents

<b>Abstract</b>	<b>i</b>
<b>Co-Authorship Statement</b>	<b>iii</b>
<b>Acknowledgements</b>	<b>iv</b>
<b>List of Figures</b>	<b>viii</b>
<b>List of Tables</b>	<b>xviii</b>
<b>List of Symbols</b>	<b>xix</b>
<b>List of Abbreviations</b>	<b>xxi</b>
<b>1 Introduction</b>	<b>1</b>
1.1 Fluids . . . . .	1
1.1.1 Shear Thinning and Shear Thickening . . . . .	3
1.1.2 Yield Stress . . . . .	5
1.1.3 Viscoelasticity . . . . .	7
1.1.4 Small-Amplitude Oscillatory Shear . . . . .	8
1.1.5 Shear Rheometry . . . . .	11
1.2 Summary of Present Work . . . . .	12
1.2.1 Overview . . . . .	12

1.2.2	Numerical Simulations of the Forced Oscillations of a Wire in a Fluid . . . . .	13
1.2.3	Vibrating-wire Rheometry . . . . .	13
1.2.4	Gelation Dynamics of Aqueous Solutions of Pluronic F127 . . . . .	14
1.2.5	Appendices . . . . .	14
	Bibliography . . . . .	15
<b>2</b>	<b>Numerical Simulations of the Forced Oscillations of a Wire in a Fluid</b>	<b>18</b>
2.1	Introduction . . . . .	18
2.2	Theory . . . . .	20
2.3	Geometry . . . . .	21
2.4	Model . . . . .	23
2.5	Results . . . . .	29
2.5.1	Newtonian Fluids . . . . .	29
2.5.2	Shear-thinning fluids . . . . .	34
2.6	Discussion . . . . .	46
2.7	Conclusion . . . . .	48
	Bibliography . . . . .	49
<b>3</b>	<b>Vibrating-wire Rheometry</b>	<b>52</b>
3.1	Introduction . . . . .	52
3.2	Theory . . . . .	54
3.2.1	Newtonian fluids . . . . .	54
3.2.2	Viscoelastic fluids . . . . .	56
3.3	Experiment . . . . .	56
3.3.1	Vibrating-wire rheometer . . . . .	56
3.3.2	Rheometric Measurements . . . . .	59
3.3.3	Sample Preparation . . . . .	60
3.4	Results . . . . .	61

3.4.1	Newtonian fluids . . . . .	61
3.4.2	Viscoelastic polymer solutions . . . . .	62
3.4.3	Aging and gelation of a clay suspension . . . . .	65
3.5	Discussion and Conclusion . . . . .	69
	Bibliography . . . . .	70
<b>4</b>	<b>Gelation Dynamics of Aqueous Solutions of Pluronic F127</b>	<b>73</b>
4.1	Introduction . . . . .	73
4.2	Materials and Methods . . . . .	76
4.3	Results . . . . .	78
4.3.1	Dynamic Rheology . . . . .	78
4.3.2	Phase Transitions . . . . .	81
4.3.3	Rheological Relaxation . . . . .	83
4.4	Discussion . . . . .	92
4.5	Conclusions . . . . .	97
	Bibliography . . . . .	98
<b>5</b>	<b>Discussion, Conclusions, and Future Work</b>	<b>101</b>
	Bibliography . . . . .	105
	<b>Appendix A Additional Measurements and Analysis</b>	<b>106</b>
A.1	Temperature Dependence . . . . .	106
A.2	Dependence of the resonance curve on $G'$ and $G''$ . . . . .	111
	Bibliography . . . . .	112
	<b>Appendix B Vibrating-wire Rheometry of Aqueous Solutions of Pluronic F127</b>	<b>113</b>
	<b>Curriculum Vitae</b>	<b>120</b>



# List of Figures

1.1	A cross-section segment of a material subject to a shear stress $\tau$ , with the bottom edge held stationary. The material will experience a strain $\gamma = dl/l$ . . . . .	2
1.2	Comparison of the viscosity vs. shear rate predicted by the Carreau model and the power-law model. For both models, $n = 0.5$ , while for the Carreau model, $\eta_\infty = 10^{-3}$ Pa·s, $\eta_0 = 1$ Pa·s, $\lambda = 10^{-4}$ s. . . . .	6
1.3	Graphical schematic of the Maxwell model of a viscoelastic fluid, consisting of a viscous dashpot and an elastic spring connected in series. $\lambda_M = \eta/G$ is the characteristic relaxation time of the model. . . . .	7
1.4	$G'$ and $G''$ vs. $\omega$ for the Maxwell model with $\lambda_M = 0.1$ s and $\eta = 10^5$ Pa·s. The crossover frequency $\omega = \lambda_M^{-1}$ is indicated with an arrow. . . . .	10
1.5	Common geometries used for shear rheometry. (a) Cone-and-Plate, (b) Parallel Plate, and (c) the Couette, or concentric cylinder, geometry. [2] . . . . .	11
2.1	(a) The simulation geometry. Fluid space is coloured blue. The tungsten wire is shaded gray. (b) The simulation mesh. (c) A magnified view of the mesh near the wire. The region shown in (c) is approximately square, with side length $16R_w$ . . . . .	21
2.2	Plots of viscosity vs. shear rate for the Carreau model with $\eta_0 = 1$ Pa·s $\eta_\infty = 10^{-3}$ Pa·s, and several different values of $\lambda$ and $n$ . . . . .	26

2.3	The $x$ -components of the (a) position, (b) velocity, and (c) acceleration of the center of the wire as a function of time for a simulation of a wire vibrating in a Newtonian fluid with $\eta = 3 \times 10^{-3}$ Pa·s and $f = 900$ Hz. The lines connect the data points to aid the eye. Note the difference in units between the plots. The simulation time extends to 0.089 s, but only the first 0.04 s are plotted here to emphasize the early-time transient. . . . .	29
2.4	The velocity in the $x$ direction of the center of the wire vs. normalized time $ft$ for simulations of a wire vibrating in a Newtonian fluid at a frequency near the resonance frequency with a) $\eta_{sim} = 3 \times 10^{-3}$ , b) $\eta_{sim} = 3 \times 10^{-2}$ , and c) $\eta_{sim} = 3 \times 10^{-1}$ Pa·s. The early-time transient damps out faster for higher viscosities. . . . .	31
2.5	Example fit of Eq. 2.22 (red curve) to the late-time velocity data from Fig. 2.3 (b). . . . .	32
2.6	The velocity resonance curves for the Newtonian-fluid simulations with viscosities shown in the legend. The inset is a magnified view of the smaller-amplitude resonance curves obtained at higher viscosities. The lines connect the data points to aid the eye. . . . .	32
2.7	(a) The resonant frequency $f_r$ , (b) the full width at half maximum $\Delta f$ , and (c) the quality factor $Q$ vs. $\eta$ for simulations of a wire vibrating in a Newtonian fluid. The curves in each plot are theoretical predictions calculated using Eq. 2.1.	33
2.8	(a) Real and imaginary components, and (b) magnitude and phase of the simulated velocity of a wire vibrating in a Newtonian fluid with $\eta = 10^{-2}$ Pa·s plotted vs. frequency. The lines are fits of Eq. 2.1 to the data. . . . .	33
2.9	(a) $\eta_{fit}$ vs. $\eta_{sim}$ from fits of the real component of Eq. 2.1 to the real component of the resonance curves for simulations of a wire vibrating in a Newtonian fluid. (b) The magnitude of the % difference between $\eta_{fit}$ and $\eta_{sim}$ vs. $\eta_{sim}$ . . . . .	34

- 2.10 Snapshots from a simulation of a wire vibrating in the  $x$  direction in a shear-thinning fluid described by Eq. 2.10 with  $n = 0.5$  and  $\lambda = 10^2$  s. The wire was driven at  $f = 680$  Hz, which was close to its resonant frequency. (a) - (g) show the spatial variation of the velocity of the fluid near the wire at times covering a half-period of the wire's oscillation. The magnitude of the velocity is given by the surface plot, while the arrows show velocity direction and logarithmic magnitude. (h)  $v(t)$ , the velocity of the vibrating wire. The labelled time points in (h) indicate the times of the corresponding velocity plots. The coordinate system is explicitly labelled in subplot (a). A video showing the full domain and all times for this simulation is included in the supplementary media. . . . . 36
- 2.11 Snapshots from a simulation of a wire vibrating in the  $x$  direction in a shear-thinning fluid described by Eq. 2.10 with  $n = 0.5$  and  $\lambda = 10^2$  s. The wire was driven at  $f = 680$  Hz, which was close to its resonant frequency. (a) - (g) show the spatial variation of the shear rate near the wire at times covering a half-period of the wire's oscillation. (h)  $v(t)$ , the velocity of the vibrating wire. (i)  $\dot{\gamma}_r(t)$ , the shear rate averaged around the circumference of the wire, as described in the text. The labelled time points in (h) and (i) indicate the times of the corresponding shear rate plots. The coordinate system is explicitly labelled in subplot (a). A video showing the full domain and all times for this simulation is included in the supplementary media. . . . . 37

2.12	Snapshots from a simulation of a wire vibrating in the $x$ direction in a shear-thinning fluid described by Eq. 2.10 with $n = 0.5$ and $\lambda = 10^2$ s. The wire was driven at $f = 680$ Hz, which was close to its resonant frequency. (a) - (g) show the spatial variation of the viscosity near the wire at times covering a half-period of the wire's oscillation. (h) $v(t)$ , the velocity of the vibrating wire. (i) $\bar{\eta}_r(t)$ , the viscosity averaged around the circumference of the wire, as described in the text. The labelled time points in (h) and (i) indicate the times of the corresponding viscosity plots. The coordinate system is explicitly labelled in subplot (a). A video showing the full domain and all times for this simulation is included in the supplementary media. . . . .	38
2.13	Fluid viscosity and shear rate as a function of (a) $x$ , along the line $y = 0$ , and (b) $y$ , along the line $x = 0$ , at the time of Fig. 2.12 (a). The gap in the data in the center of each plot corresponds to the location of the wire. . . . .	40
2.14	The velocity in the $x$ direction of the center of the wire vs. normalized time $ft$ for simulations of a wire vibrating in a shear-thinning fluid described by the Carreau model (Eq. 2.10) with (a) $n = 0.7$ , $\lambda = 10^3$ s, (b) $n = 0.5$ , $\lambda = 10^3$ s, (c) $n = 0.7$ , $\lambda = 10^4$ s, and (d) $n = 0.5$ , $\lambda = 10^4$ s. Note that for the simulation in subplot (d), the simulation time extends to $ft = 40$ , but only the first 20 oscillations are plotted here to emphasize the early-time transient. . . . .	41
2.15	Velocity resonance curves (black curves) and the spatiotemporal average viscosity $\bar{\eta}(f)$ (gray curves), for the full parameter space covered by our shear-thinning simulations. Note the difference in velocity scale between subplots. . .	42
2.16	$\bar{\eta}(f_r)$ plotted against $1/\lambda$ for simulations of a wire vibrating in shear-thinning fluids. . . . .	43
2.17	(a) The resonant frequency $f_r$ , (b) the full width at half maximum $\Delta f$ , and (c) the quality factor $Q$ plotted against $1/\lambda$ for the simulations of a wire vibrating in shear-thinning fluids. . . . .	44

2.18	(a) The resonant frequency $f_r$ , (b) the full width at half maximum $\Delta f$ , and (c) the quality factor $Q$ for the simulations of a wire vibrating in shear-thinning fluids plotted against $\bar{\eta}(f_r)$ and compared to the theoretical predictions calculated from Eq. 2.1 (black curves). . . . .	44
2.19	(a) Real and imaginary components, and (b) the magnitude and phase of the of the velocity vs. frequency with fits of Eq. 2.1 to each component for the simulation of a wire vibrating in a shear-thinning fluid with $n = 0.5$ and $\lambda = 10^3$ s. . . . .	45
2.20	(a) $\eta_{fit}$ vs. $\bar{\eta}(f_r)$ for the simulations of a wire vibrating in shear-thinning fluids. Results with the same $n$ are plotted with the same colour, and the same $\lambda$ are plotted with the same symbol. (b) The magnitude of the % difference between the two viscosities vs. $\bar{\eta}(f_r)$ . The error bars are the standard deviation between the $\eta_{fit}$ values determined by independent fits of the components of the resonance curves to Eq. 2.1. . . . .	45
3.1	Photographs of the vibrating-wire rheometer (left) and the temperature-controlled housing and magnets (center), and a schematic diagram of the instrument as seen looking through the face of the magnet (right). Colour online. . . . .	57
3.2	A schematic diagram of the experimental setup. . . . .	59
3.3	Voltage induced in the vibrating wire as a function of frequency for ethanol at 9.7 °C. The curves are independent fits the real and imaginary parts of Eq. 3.1 to each component. . . . .	62
3.4	The viscosity determined from fits to vibrating-wire data as in Fig. 3.3, $\eta_f$ , plotted against expected viscosity, $\eta_e$ . The solid line is $\eta_f = \eta_e$ . The fluids were ethanol and silicone oil at temperatures ranging from 5 to 60 °C. Uncertainties in the measured viscosities are smaller than the size of the symbol. Inset: Difference between the measured and expected values. . . . .	63

3.5	In-phase and out-of-phase components of the measured voltage for a 3.5 wt% aqueous solution of HEC. The black lines are independent fits of the real and imaginary parts of Eq. 3.1 to the components with the complex viscosity substitution, Eq. 3.8. Only every 10th data point is plotted for clarity. . . . .	64
3.6	Viscoelastic moduli for a 3.5 wt% solution of HEC in water. The data spanning 1 – 100 Hz (open symbols) were obtained from a shear rheometer using time-temperature superposition. The data at approximately 1000 Hz (solid symbols) were obtained with vibrating-wire rheometers with lengths $L = 5$ and 6 cm, as described in the text. . . . .	64
3.7	Viscoelastic moduli of a 1 wt% Laponite suspension vs. frequency after approximately 4 h of aging. Data in (a) were measured using a shear rheometer. Data in (b) were determined from dynamic light scattering (open symbols) and with the vibrating-wire rheometer (solid symbols). . . . .	66
3.8	The in-phase component of the voltage measured with the vibrating-wire rheometer for an aging Laponite clay suspension. From largest to smallest amplitude, the curves correspond to aging times of 40 min, 22 h, 52 h, and 144 h. . . . .	67
3.9	Viscoelastic moduli of the 1% Laponite suspension measured with the vibrating-wire rheometer plotted as a function of aging time. Error bars are not shown for clarity, but are similar to those plotted in Fig. 3.6. . . . .	67
4.1	$G'$ (filled symbols) and $G''$ (open symbols) vs. strain amplitude $\gamma$ at an angular frequency $\omega = 1$ rad/s for the 18 wt. % Pluronic solution at temperatures that increase counter-clockwise from $T = 10^\circ\text{C}$ in (a), to $T = 85^\circ\text{C}$ in (f). The data are at temperatures in: (a) the low-temperature sol state, (b) the low-temperature sol-gel transition, (c) the gel state, a few degrees warmer than the sol-gel transition, (d) the gel state, a few degrees cooler than the gel-sol transition (e) the high-temperature gel-sol transition, and (f) the high-temperature sol state. Data in rheologically similar states share the same row. . . . .	79

4.2	<p><math>G'</math> (filled symbols) and <math>G''</math> (open symbols) vs. angular frequency <math>\omega</math> at a strain amplitude <math>\gamma = 0.2\%</math> for the 18 wt. % Pluronic solution at temperatures that increase counter-clockwise from <math>T = 10^\circ\text{C}</math> in (a), to <math>T = 85^\circ\text{C}</math> in (f). The data are at temperatures in: (a) the low-temperature sol state, (b) the low-temperature sol-gel transition, (c) the gel state, a few degrees warmer than the sol-gel transition, (d) the gel state, a few degrees cooler than the gel-sol transition (e) the high-temperature gel-sol transition, and (f) the high-temperature sol state. Data in rheologically similar states share the same row. . . . .</p>	80
4.3	<p><math>G'</math> (black) and <math>G''</math> (gray) measured at <math>\omega = 1\text{ rad/s}</math> and <math>\gamma = 1\%</math> for aqueous solutions of Pluronic with concentrations 16 wt. % (left), 18 wt. % (center) and 20 wt. % (right) while heating (top) and cooling (bottom) at a rate of <math>6^\circ\text{C}</math> per hour. . . . .</p>	82
4.4	<p>(a) <math>G'(t)</math> (black) and <math>G''(t)</math> (gray) measured at <math>\omega = 1\text{ rad/s}</math> and <math>\gamma = 1\%</math> during an experiment in which the temperature of the 18 wt. % solution was changed in discrete steps. (b) The temperature as a function of time. The steps indicated by the arrows in (a) correspond to the relaxation curves shown in Fig. 4.7. . . .</p>	84
4.5	<p><math>G'(t)</math> (black) and <math>G''(t)</math> (gray) measured at <math>\omega = 1\text{ rad/s}</math> and <math>\gamma = 1\%</math> in the high temperature regime of the discrete temperature study of the (a) 18 wt. % and (b) 20 wt. % solutions. The temperature profile is the red step-like curve (see color figure online) using the right axis. The vertical arrow indicates the change in behaviour discussed in the text. The transition temperatures <math>T_2</math> and <math>T_3</math> determined from the continuous heating and cooling ramp experiments are shown with the labelled arrows. . . . .</p>	85

4.6	Temperature-concentration phase diagram for aqueous solutions of Pluronic F127. The results of the present work are displayed as the hatched bars, as described in the legend. For a given concentration, the left half of the bar shows the states observed when heating, while the right half shows the states observed when cooling. The width of the bars has no physical significance. Results from previous work are shown by the symbols, with corresponding references given in the legend. . . . .	87
4.7	Relaxation of the moduli of the 18 wt. % Pluronic solution following a step change in temperature. The four subplots correspond to the steps labeled in Fig. 4.4. The red dashed lines (see color figure online) are independent fits to $G'(t)$ and $G''(t)$ . a) $T = 24.4$ °C (warming), b) $T = 66$ °C (warming), c) $T = 76$ °C (cooling), and d) $T = 25$ °C (cooling). . . . .	90
4.8	Slow and fast relaxation times, $\tau_s$ , and $\tau_f$ respectively, determined by fitting $G'$ and $G''$ to Eq. 4.1 following a step in $T$ while heating and cooling. Gray symbols indicate relaxation times that are less reliable, as described in the text. The shaded regions show the temperature range over which the transitions occur, as determined from the continuous temperature ramp experiments. . . . .	91
A.1	The temperature measured in the fluid circulating around the vibrating wire vs. time. . . . .	107
A.2	Fits of Eq. A.1 (red curves) to the real component of the measured voltage from the wire vibrating in water at (a) $T = 15$ , (b) 50, and (c) 75 °C. . . . .	107
A.3	The measured resonant frequency $f_r$ and the resonant frequency predicted by Eq. A.1 (red curve) vs. $T$ when (a) heating, and (b) cooling. The theoretical predictions assume that only the fluid density and viscosity change with temperature. . . . .	108



A.4 The viscosity of water (black dots) determined from fits of the real component of Eq. A.1 to the real component of the measured voltage and the temperature in the circulating fluid around the vibrating wire (red dots) vs. time. . . . . 109

A.5 The mean of 5 measurements of  $\eta_{fit}$  near the end of the 30 min waiting time at each temperature plotted against  $T$  when (a) heating and (b) cooling. The standard deviations are smaller than the symbols in all cases. The red curves are the expected viscosity determined from the NIST Chemistry Webbook. (c) The percentage difference between the mean values of  $\eta_{fit}$  and the expected viscosity when heating, and (d) when cooling. For the most part, the standard deviation of the percentage difference is smaller than the symbols. . . . . 110

A.6 Surface plots showing (a) the resonant frequency  $f_r$ , (b) the full width at half maximum  $\Delta f$ , and (c) the quality factor  $Q$  vs.  $G'$  and  $G''$ . . . . . 111

B.1 Fits of the real and imaginary components of Eq. A.1 (black curves) to the real and imaginary components of the measured voltage of the 6 cm wire vibrating in the 18 wt.% Pluronic solution at (a)  $T = 20^\circ\text{C}$  and (b)  $T = 35^\circ\text{C}$ . (c) and (d) show the difference  $\delta V$  between the data and the fit at the same temperatures as (a) and (b), respectively. The imaginary component of the measured voltage, fit, and the resulting  $\delta V$  have been artificially shifted to lower voltage for clarity. Note that in subplot (d) only the data for  $f < 3000$  Hz are shown to emphasize the low-frequency peaks. . . . . 113

B.2 Surface plots showing  $\chi^2$  vs.  $G'$  and  $G''$  from the restricted fitting routine described in the text of the imaginary component of Eq. A.1 to the imaginary component of the measured voltage of the 6 cm wire vibrating in the 18 wt.% Pluronic solution at temperatures spanning 15 to  $85^\circ\text{C}$ , as labeled in the figure. The global minimum in each plot is marked with a red circle. . . . . 116

B.3  $G'_{wire}$  and  $G''_{wire}$  (symbols), measured using the vibrating wire as described in the text, and  $G'_{shear}$  and  $G''_{shear}$  (curves), measured using the shear rheometer as described in Chap 4, for aqueous solutions of Pluronic with concentrations 14, 16, 18, and 20 wt.%, increasing from left to right, while heating (top) and cooling (bottom). . . . . 117

B.4  $G'$  and  $G''$  vs.  $\omega$  measured using the shear rheometer (data at  $\omega < 10^3$  rad/s) as described in Chap. 4, and the vibrating-wire rheometer (data at  $\omega > 10^3$  rad/s) at temperatures  $T =$  (a) 10, (b) 35, (c) 55, and (d) 85 °C. The error bars plotted for the high-frequency vibrating-wire data show the full width at half maximum of the resonance curves. Except in Fig. B.4 (a), the error bars are smaller than the data symbols. The dashed lines in (a) and (d) show  $G'' \sim \omega^1$ . . 118

# List of Tables

2.1	Details of the simulation meshes. Symbols are defined in the text. . . . .	23
4.1	a) Temperatures $T_i$ at the start of a phase transition and the corresponding width of the transition $\Delta T_i$ measured from the continuous heating and cooling ramps shown in Fig. 4.3. The uncertainties in $T_i$ and $\Delta T_i$ are approximately $\pm 0.01$ °C. b) Temperatures $T_i$ at which the the rheological relaxation time becomes long, and the corresponding range of temperatures over which long relaxation times $\Delta T_i$ are observed, obtained from the temperature-step experiments shown in Figs 4.4-4.8. The uncertainties in the last digit of the entries in part (b) are given in parentheses and depend on the step size used in the experiment, as discussed in Sec. 4.3.3. . . . .	84

# List of Symbols

$\tau$	Shear stress
$F$	Force
$A$	Area
$\gamma$	Shear strain
$l$	Deformation length
$G, G'$	Elastic modulus
$G''$	Viscous modulus
$\dot{\gamma}$	Shear rate
$\eta$	Dynamic viscosity
$K$	Fluid consistency index
$n$	Power-law index
$\eta_{\infty}$	Viscosity at infinite shear rate
$\eta_0$	Viscosity at zero shear rate
$\lambda$	Relaxation time
$\tau_y$	Yield stress
$\omega$	Angular frequency
$f$	Frequency
$t$	Time
$M$	Torque
$R$	Cylinder radius
$L$	Length
$\theta$	Angular displacement
$V$	Voltage

$\Lambda$	Voltage amplitude
$f_0$	Resonant frequency of a vibrating wire in vacuum
$\Delta_0$	Self-damping of a vibrating wire
$\beta$	Added mass
$\beta'$	Viscous damping
$\rho$	Density
$m$	Mass
$g$	Gravitational acceleration
$v$	Velocity
$e$	Size of computational mesh element
$N_e$	Number of mesh elements
$\rho_e$	Density of mesh elements
$\mathbf{A}$	Arbitrary vector
$\underline{\mathbf{A}}$	Arbitrary tensor
$p$	Pressure
$\tau_f$	Fast relaxation time
$\tau_s$	Slow relaxation time

# List of Abbreviations

HEC	2-hydroxyethyl cellulose
PPO	Poly(propylene oxide)
PEO	Poly(ethylene oxide)
DLS	Dynamic light scattering
SAXS	Small angle X-ray scattering
SANS	Small angle neutron scattering

# Chapter 1

## Introduction

Rheology is the study of how materials flow or deform. Materials of interest to rheology range from simple Newtonian fluids like water or vegetable oil, to viscoelastic polymeric materials like plastics used in injection moulding, to asphalt used to pave our streets. Even the mantle of our planet can be described as a viscoelastic material [1]. Studying how materials behave when deformed is essential for fundamentally understanding what they are made of and how to manipulate their properties for industrial and commercial use. In this chapter we will build up the physical framework used in studying the rheological behaviour of materials.

### 1.1 Fluids

A diagram depicting the deformation of a two-dimensional cross-section of a region of material is shown in Fig. 1.1 [2]. With the bottom edge held stationary, the material will deform in response to an applied shear stress

$$\tau = \frac{F}{A}, \quad (1.1)$$

where  $F$  is the applied shearing force and  $A$  is the surface area. The deformation, or the shear strain, is

$$\gamma = \frac{dl}{l}, \quad (1.2)$$

where  $l$  is the height of the fluid region and  $dl$  is the deformation length. For small shear strains,  $\gamma$  is approximately the angle shown in the figure. For ideal elastic materials, the constitutive

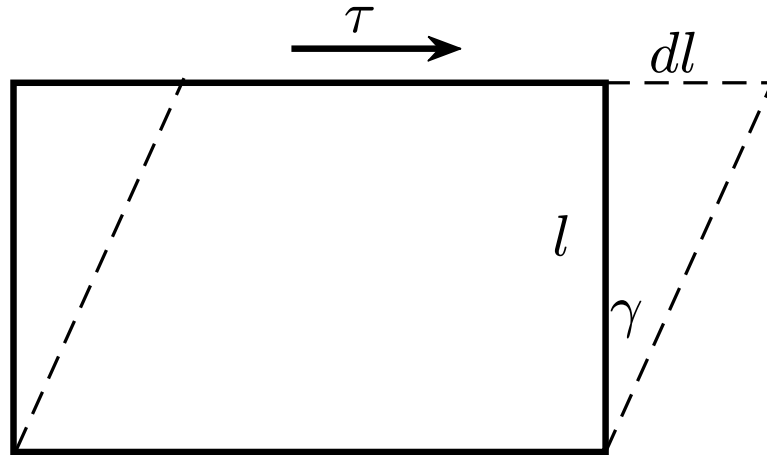


Figure 1.1: A cross-section segment of a material subject to a shear stress  $\tau$ , with the bottom edge held stationary. The material will experience a strain  $\gamma = dl/l$ .

relationship, i.e., the relationship between stress and strain, is given by

$$\tau = G\gamma, \quad (1.3)$$

where  $G$  is the elastic modulus. As long as the applied shear stress (or shear strain) is small, the material will return to its original position when the applied stress is removed. This is the 2-dimensional form of Hooke's law. For large strains, irreversible deformation like stretching or fracture may occur, in which case Eq. 1.3 no longer applies and the relationship between stress and strain is nonlinear.

For Newtonian fluids, the shear stress is related to the rate of deformation, i.e., the shear rate

$$\dot{\gamma} = \frac{d\gamma}{dt}, \quad (1.4)$$



through Newton's law of viscosity

$$\tau = \eta \dot{\gamma}, \quad (1.5)$$

where  $\eta$  is the dynamic (shear) viscosity. Even for a very small stress, a Newtonian fluid will deform irreversibly, i.e., it will flow.

The discussion above is a simple two-dimensional view of stresses and strains. In general, constitutive relationships are three-dimensional and stress, strain and related quantities are described by tensors [3]. A complete discussion of tensorial constitutive relationships is beyond the scope of this work, and we will restrict our discussion to simple two-dimensional models.

The constitutive relationships described above apply only to a small subset of materials. Solid materials such as ceramics and metals will obey Hooke's law for small strains, but fracture when the strain is too large [3]. Many simple fluids such as water, honey, or vegetable oil obey Newton's law of viscosity [4]. There are, however, many materials, called complex fluids, that behave somewhere between ideal viscous or ideal elastic materials, i.e., they are *viscoelastic*. We will begin our discussion of complex fluids by discussing non-Newtonian viscous behaviour.

### 1.1.1 Shear Thinning and Shear Thickening

For Newtonian fluids at constant temperature and pressure, viscosity is independent of shear stress or shear rate. For many fluids this is not the case, and viscosity depends on the shear rate. A simple constitutive model that illustrates this non-Newtonian behaviour is the power-law model:

$$\tau = K \dot{\gamma}^n, \quad (1.6)$$

where  $K$  is the fluid consistency index and  $n$  is the power-law index. The viscosity of a power-law fluid is the ratio of the shear stress to the shear rate:

$$\eta = \tau / \dot{\gamma} = K \dot{\gamma}^{n-1}. \quad (1.7)$$

For  $n = 1$  the fluid is Newtonian; the viscosity is independent of shear rate. For  $0 < n < 1$  the fluid is shear-thinning, i.e., the viscosity decreases with increasing shear rate. Many polymeric solutions and particle dispersions exhibit shear-thinning behaviour[3]. A few examples are blood, ketchup, and paint. Blood, a complex fluid consisting of different types of cells in solution, forms aggregates of red blood cells when at rest [5]. These aggregates give blood a rigid structure that must be broken apart before the material will flow, i.e., the material possesses a yield stress, as discussed below. Break-up of the aggregates when the blood is sheared results in shear-thinning [5, 6]. Ketchup is a complex suspension of tomato matter, i.e., cell wall fragments and cellular material in a mixture of water, vinegar, and other additives. The suspended cellular particles aggregate when at rest, forming a rigid structure that gives ketchup a yield stress [7]. Shear-thinning arises then from the break-up of that structure when the ketchup is sheared. The previous two fluids are examples of colloidal suspensions. Colloidal suspensions may also exhibit shear-thickening, as discussed below. Shear-thinning is also found in polymer solutions. In dilute polymer solutions, shear-thinning is due to a reduction in the drag on a polymer chain when it is stretched in the flow direction [3]. Ultimately the mechanism behind shear-thinning is the rearrangement of micro-structure in the fluid when it is sheared.

If  $n > 1$  in Eq. 1.7, viscosity increases with increasing shear rate; the fluid is shear-thickening. Shear-thickening is found most prevalently in concentrated dispersions of particles, although some polymer systems have been observed to shear thicken under specific conditions [8]. One example of a shear-thickening dispersion is cornstarch in water. At the microscopic scale, cornstarch is irregularly shaped particles with a diameter of approximately  $5 - 20 \mu\text{m}$  [9]. Shear-thickening in cornstarch dispersions arises from the jamming together of cornstarch particles in response to an applied force, giving them the ability to resist motion and dissipating energy. This mechanism is common among all shear-thickening dispersions of particles [8]. Shear-thickening fluids can be exploited in a number of different ways, such as in liquid body armour when integrated with ballistic fabric [10], and shock absorption when sandwiched between composite materials [11].

The power-law model given by Eq. 1.7 is unphysical for many fluids in both the high and low shear-rate limits. In the shear-thinning case, it suggests that as  $\dot{\gamma} \rightarrow 0$ ,  $\eta \rightarrow \infty$ , and as  $\dot{\gamma} \rightarrow \infty$ ,  $\eta \rightarrow 0$ . Although for yield-stress fluids, which will be discussed below, the viscosity is infinite at zero shear rate, it approaches a constant value at high shear rates. In addition, for shear-thinning polymer solutions, at very low and very high shear rates the viscosity is constant [3].

An alternative model that incorporates the plateau viscosities at high and low shear rates is the Carreau model,

$$\eta = \eta_\infty + (\eta_0 - \eta_\infty) \left[ 1 + (\lambda \dot{\gamma})^2 \right]^{(n-1)/2}, \quad (1.8)$$

where  $\eta_\infty$  is the viscosity at infinite shear rate,  $\eta_0$  is the viscosity at zero shear rate, and  $\lambda$  is the relaxation time [4]. The relaxation time determines the location of the crossover between the low shear-rate Newtonian plateau and the intermediate shear-rate power-law behaviour, as shown in Fig. 1.2. The Carreau model and the power-law model are compared in Fig. 1.2. For both models shown, the shear-thinning index is  $n = 0.5$ . The Carreau model exhibits power-law shear-thinning behaviour over a limited range of shear rate.

### 1.1.2 Yield Stress

Some materials cannot flow unless the applied stress exceeds a critical value known as the yield stress. At an applied stress greater than the yield stress, the material behaves like a viscoelastic liquid and will flow. Below the yield stress the material behaves like an elastic solid. The simplest model of a yield stress fluid is the Bingham model [12]. For an applied stress that exceeds the yield stress,

$$\tau = \tau_y + \eta_p \dot{\gamma}, \quad (1.9)$$

where  $\tau_y$  is the yield stress and  $\eta_p$  is the infinite shear-rate ‘plastic’ viscosity. Once yielded, the Bingham model describes a fluid with a viscosity that shear-thins and approaches  $\eta_p$  at high shear-rates.

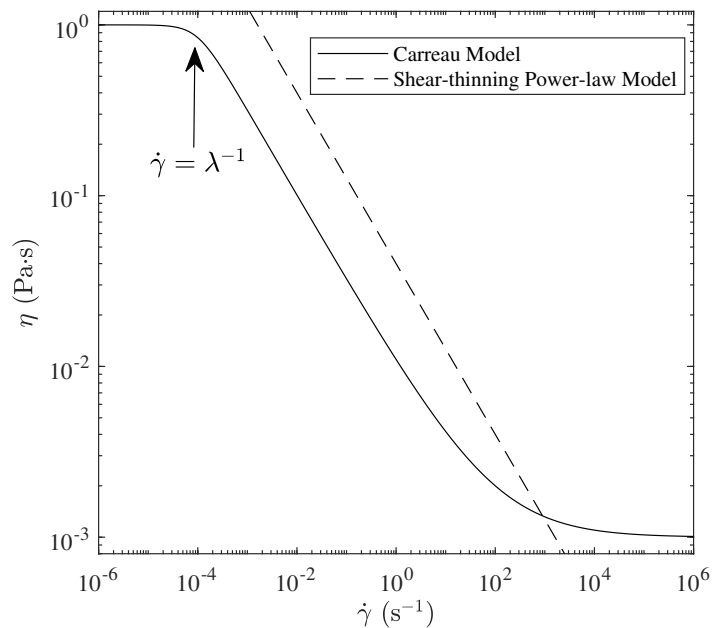


Figure 1.2: Comparison of the viscosity vs. shear rate predicted by the Carreau model and the power-law model. For both models,  $n = 0.5$ , while for the Carreau model,  $\eta_\infty = 10^{-3}$  Pa·s,  $\eta_0 = 1$  Pa·s,  $\lambda = 10^{-4}$  s.

The next simplest model is the Herschel-Bulkley model [13], which describes a yield-stress fluid that allows for a nonlinear increase of stress with shear rate. For this model, again, when the applied stress is less than the yield stress the fluid does not flow ( $\dot{\gamma} = 0$ ). For an applied stress greater than the yield stress,

$$\tau = \tau_y + k\dot{\gamma}^n, \quad (1.10)$$

where  $k$  is the fluid consistency index, similar to the power-law model. Indeed, the second term in this constitutive model is simply the power-law model. In many cases, the behaviour of real yield-stress fluids is better described by the Herschel-Bulkley model than by the Bingham model.

Yield stress fluids are very common in our day-to-day life. They are often found in our bathroom cabinets — shaving gel, toothpaste, or cosmetic creams — or in our refrigerators — mayonnaise, whipped cream, or ketchup. Tooth paste will flow out of the tube when you squeeze it, but it will retain its shape on your toothbrush due to its intrinsic yield stress. Sim-

ilarly, mayonnaise will flow when you spread it on a sandwich, but it retains its shape in its container, even if it is tilted. An understanding of what causes the yield stress, and how to tune it, is important from a practical perspective when designing consumer products. Yield stress fluids are also prevalent in industry. One example arises in the transport of waxy crude oil through pipelines. Waxy crude oil exhibits a yield stress [14], and understanding how the yield stress influences pressure-driven flow in a pipe is of importance to oil transport and recovery [15].

### 1.1.3 Viscoelasticity

The discussion so far has been about how the steady-shear viscosity of non-Newtonian fluids can differ from that of Newtonian fluids. We have mentioned that non-Newtonian flow behaviour arises from the presence of structure within the fluid. This structure may also contribute elasticity to the fluid. Materials that exhibit both viscous and elastic-like behaviour are called viscoelastic. One of the simplest models of a viscoelastic fluid is the Maxwell model. This

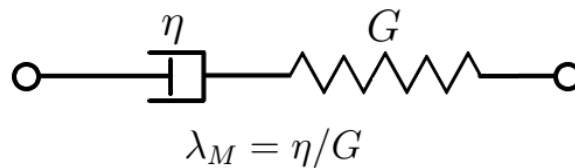


Figure 1.3: Graphical schematic of the Maxwell model of a viscoelastic fluid, consisting of a viscous dashpot and an elastic spring connected in series.  $\lambda_M = \eta/G$  is the characteristic relaxation time of the model.

model was erroneously [3] proposed by James Clerk Maxwell in 1867 to describe gases [16], but it has since been adopted in rheology to describe simple viscoelastic fluids. The Maxwell model incorporates viscous and elastic behaviour into one constitutive equation. The model can be graphically represented by a viscous dashpot and an elastic spring connected in series as shown in Fig. 1.3. The stress-strain relationships for the individual elements have already been introduced in Eqs. 1.3 and 1.5. When subject to a stress, the total strain in a Maxwell material is the sum of the viscous strain due to the dashpot  $\gamma_D$  and the elastic strain due to the

spring  $\gamma_E$ , i.e.,  $\gamma = \gamma_D + \gamma_E$ . The stress acting on each element is the same, i.e.,  $\tau = \tau_D = \tau_E$ . To obtain a relationship between stress and shear rate we differentiate both sides of the strain relation with respect to time

$$\dot{\gamma} = \dot{\gamma}_D + \dot{\gamma}_E. \quad (1.11)$$

The shear rate from the dash-pot is related to stress through Eq. 1.5, while the shear rate from the elastic spring can be calculated from the time-derivative of Eq. 1.3, yielding

$$\dot{\gamma} = \frac{\tau}{\eta} + \frac{1}{G} \frac{d\tau}{dt} \quad (1.12)$$

or, after rearranging and defining the relaxation time  $\lambda_M = \eta/G$ ,

$$\tau + \lambda_M \frac{d\tau}{dt} = G\lambda_M \dot{\gamma}. \quad (1.13)$$

This model describes a material with only one relaxation time. Real materials typically have more than one relaxation time [4]. To account for this, many Maxwell elements can be combined in parallel into the Generalized Maxwell Model [4], where Eq. 1.13 represents the stress and strain in one element, and the total stress in the material is the sum of the stresses in all of the elements.

### 1.1.4 Small-Amplitude Oscillatory Shear

A common experimental method for studying viscoelastic materials is to apply an oscillatory shear strain (or stress) and measure the resulting stress (or strain). For this discussion we will consider an applied strain. We assume here that the amplitude of the applied strain is sufficiently small that the response of the material is linear. We consider an oscillatory shear strain of the form

$$\gamma(t) = \gamma_0 \sin(\omega t), \quad (1.14)$$

where  $\gamma_0$  is the strain amplitude and  $\omega$  is the angular frequency. If this strain is applied to an elastic material that obeys Hooke's law (Eq. 1.3), the resulting stress is

$$\tau(t) = G\gamma_0 \sin(\omega t), \quad (1.15)$$

i.e., the stress is sinusoidal and *in phase* with the applied strain. If the strain is applied to a viscous fluid that obeys Newton's Law of Viscosity (Eq. 1.5), the resulting stress is

$$\tau(t) = \eta\omega\gamma_0 \cos(\omega t), \quad (1.16)$$

i.e., the stress is sinusoidal and  $90^\circ$  *out of phase* with the applied strain. In general, for a viscoelastic fluid, the phase difference  $\phi$  between the applied strain and resulting stress will be somewhere between  $0$  and  $90^\circ$  [17], i.e.,  $\tau(t) = \tau_0 \sin(\omega t + \phi)$ . This can be expanded into in-phase and out-of-phase components:

$$\tau(t) = \tau_0 [\cos(\phi) \sin(\omega t) + \sin(\phi) \cos(\omega t)]. \quad (1.17)$$

The amplitude of the in-phase and out-of-phase components divided by the strain amplitude are known as the elastic modulus  $G'(\omega)$  and the viscous modulus  $G''(\omega)$ , respectively. In general, the moduli depend on frequency. Eq. 1.17 can therefore be written as

$$\frac{\tau(t)}{\gamma_0} = G'(\omega) \sin(\omega t) + G''(\omega) \cos(\omega t). \quad (1.18)$$

Comparing this form to Eqs. 1.15 and 1.16, we can identify the viscoelastic moduli for elastic solids and Newtonian liquids as

$$G'(\omega) = G \quad (1.19)$$

$$G''(\omega) = 0 \quad (1.20)$$

for an elastic solid, and

$$G'(\omega) = 0 \quad (1.21)$$

$$G''(\omega) = \eta\omega \quad (1.22)$$

for a Newtonian liquid. For viscoelastic fluids, the dependence of the moduli on frequency is

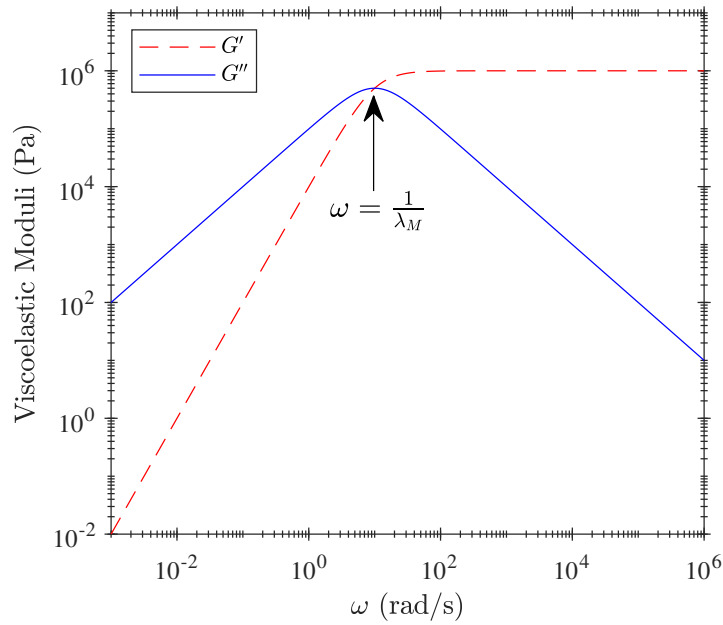


Figure 1.4:  $G'$  and  $G''$  vs.  $\omega$  for the Maxwell model with  $\lambda_M = 0.1$  s and  $\eta = 10^5$  Pa·s. The crossover frequency  $\omega = \lambda_M^{-1}$  is indicated with an arrow.

more complicated. For the Maxwell model presented above, the viscoelastic moduli are [4]

$$G'(\omega) = \frac{\eta\lambda_M\omega^2}{1 + \lambda_M^2\omega^2}, \quad (1.23)$$

$$G''(\omega) = \frac{\eta\omega}{1 + \lambda_M^2\omega^2}. \quad (1.24)$$

The moduli for the Maxwell model are plotted in Fig. 1.4 with  $\lambda_M = 0.1$  s and  $\eta = 10^5$  Pa·s.  $G'$  and  $G''$  cross over at  $\omega = 1/\lambda_M$ , allowing for an easy determination of the relaxation time of a Maxwell material from experimental measurements of the viscous and elastic moduli.



### 1.1.5 Shear Rheometry

One of the more common experimental tools used in rheology is the shear rheometer. Shear rheometers work by confining a fluid within a geometry, applying a strain, and measuring the stress (or applying a stress and measuring the strain). Three common geometries used for shear rheometry are shown in Fig. 1.5. For all three of the geometries shown, one component of the geometry is typically held fixed, e.g., the bottom plate in the Cone-and-Plate or Parallel Plate geometries is held fixed while the top plate is rotated. Most of the shear rheometry done in this thesis used the Couette cell geometry, with the outer cylinder held fixed while the inner cylinder was rotated.

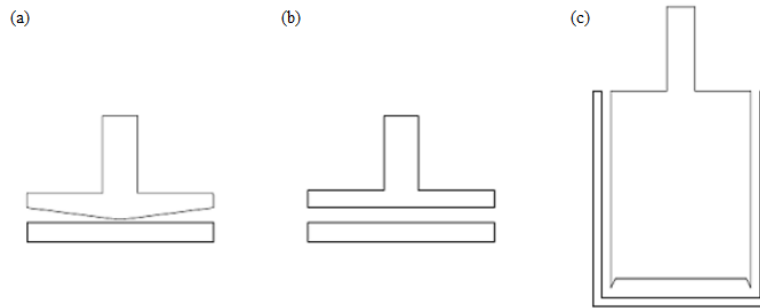


Figure 1.5: Common geometries used for shear rheometry. (a) Cone-and-Plate, (b) Parallel Plate, and (c) the Couette, or concentric cylinder, geometry. [2]

The rheometer used in this thesis was an Anton-Paar MCR-302 shear rheometer. The rheological parameters extracted from an experiment are the shear stress and shear strain, which are then related to material properties such as the viscous and elastic moduli as outlined in the previous section. Rheometers do not directly measure these quantities, however. Instead, they measure the torque  $M$  on the tool and the angular displacement  $\theta$  of the tool, then relate these quantities to the shear stress and shear strain, respectively. The relations between these quantities depend on the geometry being used. For an ideal Couette cell in the small gap limit, the stress is related to the torque through [3]

$$\tau = \frac{M}{2\pi R_i^2 L}, \quad (1.25)$$

where  $R_i$  is the radius of the inner cylinder and  $L$  is its length. The shear strain is related to the angular displacement by

$$\gamma = \theta \frac{R_o + R_i}{2(R_o - R_i)}, \quad (1.26)$$

where  $R_o$  is the radius of the outer cylinder.

There are a few experimental limitations that restrict the range of moduli and frequencies that a shear rheometer can probe [18]. Rheometers have both high and low frequency limits. The low frequency limit is more a limit of practicality, as the measurement time per point at low frequency gets very long. Most shear rheometers, including the one used in this thesis, are restricted to frequencies less than 100 Hz [19]. In addition, the inertia of the instrument and the sample limit the high-frequency operation of the rheometer, causing the instrument to report a quadratic increase in the moduli with frequency at high frequencies [18]. In addition, the capabilities of the instrument put a limit on the smallest and largest torques that can be measured. For the MCR-302 rheometer used in this work, the minimum measurable torque is  $0.01 \mu\text{N}\cdot\text{m}$  and the maximum measurable torque is  $200 \text{ mN}\cdot\text{m}$  [19]. This sets upper and lower limits on the magnitude of the moduli the rheometer can measure. The lower limit also helps motivate the development of the vibrating-wire rheometer discussed in Chap. 2, since it prevents the study of low-viscosity fluids with shear rheometers.

## 1.2 Summary of Present Work

### 1.2.1 Overview

The majority of the work presented in this thesis focusses on the development of a novel rheometer based on a vibrating wire that allows for the measurement of viscoelastic moduli at high frequencies and low viscosities, both regimes which are inaccessible to conventional shear rheometers. This was investigated both experimentally through the construction and testing of a device, and numerically through the 2-dimensional simulation of a vibrating-wire

in Newtonian and shear-thinning fluids using COMSOL Multiphysics.

## 1.2.2 Numerical Simulations of the Forced Oscillations of a Wire in a Fluid

In Chap. 2 we use COMSOL Multiphysics software to numerically study the two-dimensional forced oscillations of a wire vibrating in Newtonian fluids and shear-thinning fluids described by the Carreau model. When the wire is subject to a sinusoidal driving force, it exhibits resonant behaviour that depends on the viscosity of the fluid it is in. The simulations of the wire vibrating in a Newtonian fluid were extremely well described by the theory for a wire vibrating in a Newtonian fluid developed by Retsina *et al.* [20, 21]. Our simulations of a wire vibrating in a Carreau fluid revealed resonant behaviour similar to the behaviour of the wire vibrating in Newtonian fluids. We find that the shear rate and viscosity in the fluid vary significantly in both space and time. The theory of a wire vibrating in a Newtonian fluid could describe the behaviour of a wire vibrating in a Carreau fluid if the viscosity in the theory is set equal to the viscosity averaged spatially around the circumference of the wire and over one period of oscillation.

## 1.2.3 Vibrating-wire Rheometry

In Chap. 3 we describe the design and operation of a novel vibrating-wire rheometer. Our device consists of a tungsten wire under tension and immersed in a fluid in a magnetic field. When an alternating current is passed through the wire it vibrates at the driving frequency, and we measure the voltage induced across the wire as a function of frequency. The resonant frequency of the wire is of order 1000 Hz, and can be tuned by varying its length and the applied tension. We modify an analytic expression for the induced voltage, previously derived for Newtonian fluids, to include a complex viscosity, and determine the viscous and elastic moduli of complex fluids by fitting this expression to our data. Our device gives excellent

results for the viscosity of Newtonian fluids and the viscoelastic moduli of aqueous polymer solutions, at frequencies higher than those accessible using a conventional shear rheometer. Because the amplitude of the wire's vibrations is on the order of a few microns, it can be used to probe the microrheology of fluids that are heterogeneous on that scale. We illustrate this by measuring the micron-scale moduli of a viscoplastic suspension of Laponite clay as it gels.

### 1.2.4 Gelation Dynamics of Aqueous Solutions of Pluronic F127

In Chap. 4 we study the gelation dynamics of solutions of Pluronic F127, a triblock copolymer, using oscillatory rheometry. As a sufficiently concentrated solution is slowly and continuously heated from 10 to 85 °C, it undergoes a transition from sol to gel around room temperature, followed by a gel-sol transition at a higher temperature. The sol-gel transition temperature decreases and the width in temperature of the gel phase broadens with increasing concentration. The transitions occur over a temperature range of a few degrees, over which the viscous and elastic moduli change by more than 5 orders of magnitude. On cooling, the width in temperature of the gel phase is larger and the transitions themselves extend over a larger range of temperature. Near the phase transitions, the rheological relaxation time becomes very long — up to of order  $10^4$  s. Gelation in Pluronic solutions is due to the arrangement of micelles into clusters that grow in size to form a large-scale lattice, and our results indicate that changes in microstructure that accompany the equilibration of these clusters happen very slowly.

### 1.2.5 Appendices

In App. A we present additional measurements using our vibrating-wire rheometer. We study the influence of temperature on the resonant frequency of the wire and the measured viscosity in water. We find that although the resonant frequency of the wire changes significantly with temperature, by allowing it to be a free parameter in our curve fitting routine, the viscosity of water can still be accurately determined. In addition, we investigate how the shape of the resonant curves of the wire depends individually on  $G'$  and  $G''$ .

In App. B we present measurements of the viscoelastic properties of aqueous solutions of Pluronic made using our vibrating-wire rheometer. Allowing for the difference in frequency, our results are fully consistent with measurements of the viscoelastic properties of Pluronic using a shear rheometer presented in Chap. 4.

## Bibliography

- [1] W. R. Peltier. Mantle Convection and Viscoelasticity. *Annu. Rev. Fluid Mech.*, 17:561–608, 1985.
- [2] J. R. de Bruyn and F. K. Oppong. Rheological and microrheological measurements of soft condensed matter. In J. Olafsen, editor, *Experimental and Computational Techniques in Soft Condensed Matter Physics*. Cambridge University Press, 2010.
- [3] Christopher W. Macosko. *Rheology: Principles, Measurements, and Applications*. Wiley-VCH, 1994.
- [4] F. A. Morrison. *Understanding Rheology*. Oxford University Press, 2001.
- [5] J. Goldstone, H. Schmid-Schonbein, and R. Wells. The rheology of red blood cell aggregates. *Microvasc. Res.*, 2:273–286, 1970.
- [6] E. W. Merrill. Rheology of blood. *Physiol. Rev.*, 49, 1969.
- [7] E. Bayod, W. P. Willers, and E. Tornberg. Rheological and structural characterization of tomato paste and its influence on the quality of ketchup. *LWT Food Sci. Technol.*, 41:1289–1300, 2008.
- [8] J. Ding, P. J. Tracey, W. Li, G. Peng, and P. G. Whitten. Review on shear thickening fluids and applications. *Text. Light Ind. Sci. Tech.*, 2:161–173, 2013.
- [9] S. R. Waitukaitis and H. M. Jaeger. Impact-activated solidification of dense suspensions via dynamic jamming fronts. *Nature*, 487:205–209, 2012.

- [10] N. J. Wagner and E. D. Wetzel. Advanced body armour utilizing shear thickening fluids, U.S. Patent 7226878, 2007.
- [11] C. Fischer, S. A. Braun, P-E. Bourban, V. Michaud, C. J. G. Plummer, and J-A. E. Manson. Dynamic properties of sandwich structures with integrated shear-thickening fluids. *Smart Mater. Struct.*, 15:1467–1475, 2006.
- [12] E. C. Bingham. An investigation of the laws of plastic flow. *Bull. Bur. Stds.*, 13:309, 1917.
- [13] W. H. Herschel and R. Bulkley. Konsistenzmessungen von gummi-benzollösungen. *Kolloid-Zeitschrift*, 39, 1926.
- [14] H. P. Rønningsen. Rheological behaviour of gelled, waxy north sea crude oils. *J. Pet. Sci. Eng.*, 7:177–213, 1992.
- [15] Y. Liu and J. R. de Bruyn. Start-up flow of a yield-stress fluid in a vertical pipe. *J. non-Newtonian Fluid Mech.*, 257:50–58, 2018.
- [16] J. C. Maxwell. IV. on the dynamical theory of gases. *Phil. Trans. R. Soc. Lond.*, 157:49–88, 1867.
- [17] J. D. Ferry. *Viscoelastic Properties of Polymers*. John Wiley & Sons, 1980.
- [18] R. H. Ewoldt, M. T. Johnston, and L. M. Caretta. Experimental challenges of shear rheology: how to avoid bad data. In S. Spagnolie, editor, *Complex Fluids in Biological Systems*. Springer, 2015.
- [19] Anton-Paar GmbH. *MCR Series Instruction Manual*, 2018.
- [20] T. Retsina, S. M. Richardson, and W. A. Wakeham. The theory of a vibrating-rod densimeter. *Appl. Sci. Res.*, 43:127–158, 1986.

- [21] T. Retsina, S. M. Richardson, and W. A. Wakeham. The theory of a vibrating-rod viscometer. *Appl. Sci. Res.*, 43:325–346, 1987.

# Chapter 2

## Numerical Simulations of the Forced Oscillations of a Wire in a Fluid

### 2.1 Introduction

In the previous chapter we presented the experimental realization of a vibrating-wire device for measuring the viscosity of Newtonian fluids and the viscoelastic moduli of viscoelastic fluids. Here we present numerical simulations of a wire vibrating in Newtonian and non-Newtonian fluids. Simulations of the wire vibrating in Newtonian fluids allow for a numerical test of the theory of a vibrating-wire viscometer presented by Retsina *et al.* [1, 2]. Simulations in non-Newtonian fluids may help us to better understand the behaviour of our new device and provide some guidance in the interpretation of data on non-Newtonian fluids that are obtained experimentally.

There are many studies in the literature concerning the flow of Newtonian fluids around a stationary body; see, for example, the reviews in Refs. [3, 4]. Under appropriate conditions, a periodic wake forms downstream of the object from the shedding of vortices [3]. This vortex shedding exerts a periodic force on the body, and if the body is flexible it will oscillate. This is seen, for example, in air flow around chimneys, transmission lines, and suspension bridges [3]



and in water flow around underwater cables, pipelines, and off-shore oil rig risers [5]. Flow-induced vibrations are a major cause of structural fatigue and failure [6, 5] and considerable effort has gone into developing damping mechanisms to counteract the vibrations [7].

There are also many computational studies of Newtonian flow around a moving body. Examples include the flow past a cylinder vibrating parallel to the flow [8], the flow past a rotating cylinder [9], the flow-induced vibrations of a rotating cylinder [10], and the flow past a cylinder vibrating with a prescribed displacement perpendicular to the flow [11, 12]. The focus of these studies has been on how the motion of the cylinder affects the wake or the lift and drag forces on the cylinder. There are similar studies of non-Newtonian flows around objects. Examples include studies of the steady flow of shear-thinning and shear-thickening power-law fluids past a cylinder [13] and the flow of Boger fluids past a cylinder [14], among others [15, 16, 17]. The focus of these studies was on understanding the effects of non-Newtonian fluid properties on the drag force on the cylinder and the steady flow.

To the best of our knowledge, there are no numerical studies in the literature concerning forced transverse oscillations of a cylinder in the absence of an externally imposed flow in either Newtonian nor non-Newtonian fluids.

In this chapter we used the commercial software COMSOL Multiphysics version 5.1 (COMSOL Inc.), referred to below simply as COMSOL, to simulate the resonance behaviour of a wire vibrating in Newtonian and non-Newtonian fluids. COMSOL is a finite-element software package that can be used to study a variety of scientific and engineering problems [18]. It includes a number of different pre-built physics “packages,” that include implementations of the equations, numerical solvers, and meshing and boundary condition programming relevant to the problem of interest. In the work described in this chapter, we used COMSOL’s Structural Mechanics and Fluid Flow packages. Stresses in the Structural Mechanics package are described by the Piola-Kirchoff stress tensor [19]. Fluid Flow is described by the Navier-Stokes equations [20]. COMSOL specializes in what they refer to as “multiphysics” simulations, i.e., it natively allows for the coupling of different physics packages. The Fluid-Structure Interac-

tion module used in this chapter allows for the simulation of the effects of the fluid on a solid object and *vice versa*, as discussed more fully below.

## 2.2 Theory

The systems in the literature mentioned above simulate the behaviour of a cylinder immersed in a flowing fluid. Some of these papers concerned forced oscillations of the cylinder, but the vibrational resonance of the cylinder was not investigated. In this chapter, we numerically study the forced oscillations of a cylinder, which from here on we will refer to as a wire, immersed in a fluid that is initially at rest and with no externally imposed flow. This problem was first studied theoretically by Stokes in 1850 [21]. Stokes' work was applied by Tough *et al.* in 1964 in their realization of a vibrating-wire viscometer [22]. More recently, in 1987, Retsina *et al.* expanded upon Stokes' work and developed a more complete theory of how the steady, transverse oscillations of a wire in a Newtonian fluid could be used as the basis for a viscometer [1, 2]. They considered the transverse motion of a long wire with circular cross-section clamped at both ends. The wire was immersed in a fluid in a cylindrical container. They assumed that the wire was significantly longer than its radius so that axial effects could be neglected. This effectively reduces the problem to one where the transverse oscillations of the wire drive motion of the fluid. They considered a two-dimensional cross-section of the wire immersed in a Newtonian fluid and analytically solved the Navier-Stokes equations in polar  $(r, \theta)$  coordinates when the wire is forced to oscillate in the  $r - \theta$  plane. They determined that, when subject to a sinusoidal driving force at frequency  $f$ , the wire will oscillate at the driving frequency with an amplitude that depends on  $f$  and the physical properties of the wire and fluid. They showed that the amplitude of the wire's velocity as a function of  $f$  is given by

$$v(f) = \frac{fFi}{\pi^2 \rho_w R^2 [f_0^2 - (1 + \beta)f^2 + (\beta' + 2\Delta_0)f^2i]}, \quad (2.1)$$

where  $2F$  is the amplitude of the applied force per unit length on the wire,  $i = \sqrt{-1}$ ,  $\rho_w$  is the density of the wire,  $R$  is its radius,  $f_0$  is the resonant frequency of the wire in a vacuum,  $\beta$  is the added mass arising from fluid displacement,  $\beta'$  is a viscous damping term, and  $\Delta_0$  is the self-damping of the wire.  $\beta$  and  $\beta'$  depend on the density and viscosity of the fluid and their full functional forms are given in Chap. 3. Eq. 2.1 describes the resonance behaviour of the wire. In Chap. 3 we will demonstrate that the resonance can be experimentally measured by measuring the voltage induced across an alternating-current-carrying wire placed in a magnetic field. In this case, the force that drives the oscillations is the Lorentz force on the wire. In this chapter, we numerically simulate the motion of such a wire, first in Newtonian fluids to provide a confirmation of the theory, and second in shear-thinning fluids to investigate how the variation of viscosity with shear rate influences the frequency-dependent motion of the wire.

## 2.3 Geometry

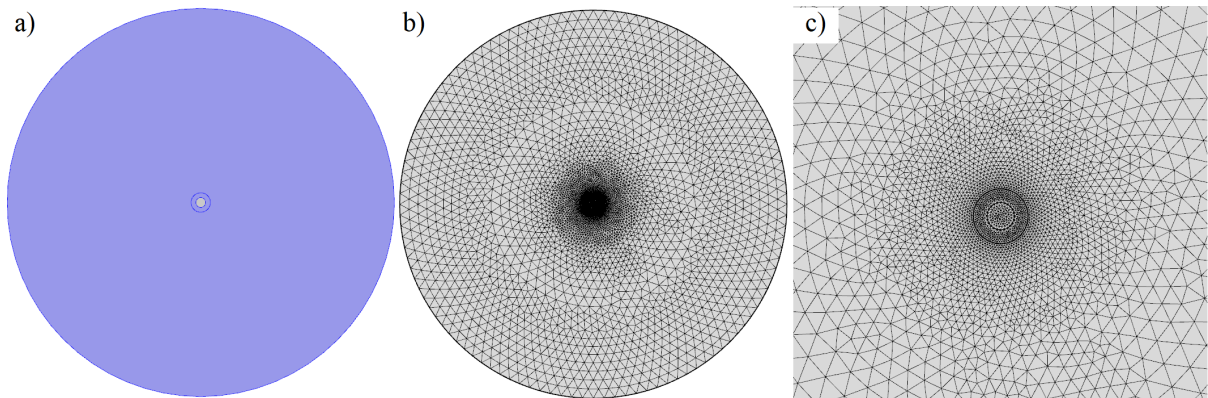


Figure 2.1: (a) The simulation geometry. Fluid space is coloured blue. The tungsten wire is shaded gray. (b) The simulation mesh. (c) A magnified view of the mesh near the wire. The region shown in (c) is approximately square, with side length  $16R_w$ .

We performed two-dimensional simulations of a wire vibrating in Newtonian and non-Newtonian fluids. The simulation domain consisted of a circle, representing the wire, contained within a larger, initially concentric circle representing the fluid. While the fluid volume could be chosen to have any shape, we used a circle for meshing simplicity, symmetry, and so that

we were simulating the same system as studied theoretically by Retsina *et al.* The geometry used is shown in Fig. 2.1 (a). The outer boundary of the simulation space is a circle with radius  $R_c = 3$  mm. The inner circle shown in Fig. 2.1 is the tungsten wire, with radius  $R_w = 0.075$  mm. We can estimate the size of the region of fluid affected by the motion of the wire from the characteristic viscous length  $d = \sqrt{\eta t / \rho}$ , where  $\eta$  is the dynamic viscosity and  $\rho$  is the density of the fluid. If the time-scale  $t$  is taken to be the period of oscillation, then for  $t = 1$  ms ( $f = 1000$  Hz) and  $\eta = 10^{-3}$  Pa·s, we find  $d \sim 0.3$  mm, and for  $t = 1$  ms and  $\eta = 1$  Pa·s,  $d = 1$  mm. For longer periods,  $d$  will be larger. The influence of the wall on the simulations was greatest for higher viscosities. For simulations of a wire vibrating in a Newtonian fluid with  $R_c = 1$  mm, for  $\eta < 0.1$  Pa·s, the qualitative properties of the resonance curves for our simulations, discussed in Sec. 2.5.1, deviated from the theoretical predictions of Retsina *et al.* [1, 2] by less than 0.5%, but for  $\eta = 1$  Pa·s, it deviated by 28%. For our simulation of a wire vibrating in a Newtonian fluid with  $\eta = 1$  Pa·s and  $R_c = 3$  mm, the percentage deviation was 4%, therefore we conclude that  $R_c = 3$  mm was large enough for wall effects to be negligible.

The computational mesh used in our simulations is shown in Fig. 2.1 (b) and (c). The equations presented in the next section are evaluated at each node of the mesh. The most important region for the simulation is near the interface between the tungsten wire and the surrounding fluid, where changes in the shear rate are greatest. With that in mind, the mesh elements in the annular portion of the computational domain lying in the range  $R_w \leq r \leq 2R_w$  were chosen to be smaller than in the surrounding fluid, as shown in Fig. 2.1 (c). The details of the mesh in each region, including the predefined mesh setting selected and imposed by COMSOL, the resulting minimum and maximum mesh element sizes  $e_{\min}$  and  $e_{\max}$ , number of triangular elements  $N_e$ , and mesh density  $\rho_e$ , are listed in Table 2.1. The average mesh quality, as defined in [18], was 0.973, which is close to optimal. To confirm that the mesh size had no effect on the solution, we manually decreased  $e_{\min}$  and  $e_{\max}$  to increase the number of mesh elements and ran test simulations of the wire vibrating in a Newtonian fluid. We observed no noticeable difference between simulations performed with the finer mesh and those performed

using the mesh detailed in Table 2.1. The total number of degrees of freedom, i.e., the number of dependent variables solved for times the number of mesh nodes, was 20941.

For all simulations, convergence at a given time was reached when the root mean square difference (as defined in [18]) between the solutions before and after an iteration, across all degrees of freedom, was less than 1%. To confirm that this convergence criterion was sufficient, we manually decreased it to 0.01% and ran test simulations of the wire vibrating in a Newtonian fluid. We observed no significant difference between simulations performed with convergence criteria of 1% and 0.01%.

Table 2.1: Details of the simulation meshes. Symbols are defined in the text.

Domain	COMSOL Setting	$e_{\min}$ (mm)	$e_{\max}$ (mm)	$N_e$	$\rho_e$ (elements/mm <sup>2</sup> )
Wire	General Physics Extremely Fine	$4 \times 10^{-5}$	0.02	240	13667
High mesh density Fluid	Fluid Dynamics Extremely Fine	$4 \times 10^{-5}$	0.0134	1018	19193
Bulk fluid	Fluid Dynamics Fine	0.0024	0.17	5118	182

To account for the displacement of the wire, we used the Fluid-Structure Interaction module in COMSOL, which allows free deformation of the mesh in response to a load acting on the fluid or structure in the simulation [18]. This allows for two-way coupling between the structure and the fluid. If the structure moves, the fluid is displaced and the mesh is updated for the new system. Similarly, if the fluid displaces or deforms the structure, the mesh is updated.

## 2.4 Model

The motion of the simulated fluids was described by the Navier-Stokes equations [23], which are an expression of the conservation of momentum for the fluid, along with an equation for the conservation of mass. Conservation of mass is given by

$$\frac{\partial \rho}{\partial t} + \nabla \cdot (\rho \mathbf{u}_{\text{fluid}}) = 0, \quad (2.2)$$

where  $\mathbf{u}_{\text{fluid}}$  is the velocity vector of the fluid. Conservation of momentum is given by

$$\rho \frac{\partial \mathbf{u}_{\text{fluid}}}{\partial t} + \rho(\mathbf{u}_{\text{fluid}} \cdot \nabla)\mathbf{u}_{\text{fluid}} = \nabla \cdot [-p\mathbf{I} + \underline{\boldsymbol{\tau}}], \quad (2.3)$$

where  $p$  is pressure,  $\mathbf{I}$  is the identity matrix, and  $\underline{\boldsymbol{\tau}}$  is the viscous stress tensor. The pressure in the simulation was taken to be 1 atm and did not vary. In general, the conservation of momentum equation could include an additional body force term on the right hand side of Eq. 2.3, but since we will not be considering such forces in our simulations, it was not included. The viscous stress tensor incorporates the constitutive model for the fluid. For a Newtonian fluid,

$$\underline{\boldsymbol{\tau}} = \eta \underline{\dot{\boldsymbol{\gamma}}} - \frac{2}{3}\eta(\nabla \cdot \mathbf{u}_{\text{fluid}})\mathbf{I}, \quad (2.4)$$

where  $\underline{\dot{\boldsymbol{\gamma}}} = \nabla \mathbf{u}_{\text{fluid}} + (\nabla \mathbf{u}_{\text{fluid}})^T$  is the strain-rate tensor [23]. Combining Eq. 2.4 with Eq. 2.3 yields the full conservation of momentum equation,

$$\rho \frac{\partial \mathbf{u}_{\text{fluid}}}{\partial t} + \rho(\mathbf{u}_{\text{fluid}} \cdot \nabla)\mathbf{u}_{\text{fluid}} = \nabla \cdot [-p\mathbf{I} + \eta \underline{\dot{\boldsymbol{\gamma}}} - \frac{2}{3}\eta(\nabla \cdot \mathbf{u}_{\text{fluid}})\mathbf{I}]. \quad (2.5)$$

Although we expect the fluid velocity to be small enough that the flow is incompressible, and Retsina *et al.* imposed the incompressibility condition when developing their theory [1, 2], the incompressibility condition was not explicitly imposed in our simulations. To check whether compressibility had an influence on the results, we ran simulations of the wire vibrating in a Newtonian fluid with  $\eta = 1$  Pa·s with and without imposing the incompressibility condition. No significant difference was observed between the two simulations.

At the boundary between the wire and the fluid, COMSOL's "Fluid-Structure Interface" boundary condition was used. This boundary condition ensures that a no-slip condition is imposed at the boundary between the wire and the fluid, i.e., the velocity of the fluid equals the velocity of the wire at the interface, and also that the fluid exerts a force on the wire [18].

Mathematically, the first condition states that at each point on the boundary,

$$\mathbf{u}_{\text{fluid}} = \frac{\partial \mathbf{r}_{\text{solid}}}{\partial \mathbf{t}}, \quad (2.6)$$

where  $\mathbf{r}_{\text{solid}}$  is the displacement of the wire. The second condition is

$$\underline{\boldsymbol{\sigma}} \cdot \mathbf{n} = \underline{\boldsymbol{\Gamma}} \cdot \mathbf{n}, \quad (2.7)$$

where  $\underline{\boldsymbol{\sigma}}$  is the stress on the wire and

$$\underline{\boldsymbol{\Gamma}} = \left[ -p\underline{\mathbf{I}} + \eta\underline{\dot{\boldsymbol{\gamma}}} - \frac{2}{3}\eta(\nabla \cdot \mathbf{u}_{\text{fluid}})\underline{\mathbf{I}} \right] \quad (2.8)$$

is the sum of the pressure and the viscous stress.

At the outer boundary of the simulation domain, COMSOL's "Open Boundary" condition was used. This condition allows for free convective inflow and outflow at the boundary, and ensures that mass is conserved if fluid flows into or out of the simulation domain [20]. Mathematically, at the boundary,

$$\underline{\boldsymbol{\Gamma}}\mathbf{n} = \mathbf{0}. \quad (2.9)$$

For all fluids simulated,  $\rho$  was taken to be  $1000 \text{ kg/m}^3$  and  $\eta$  was varied between simulations. The Carreau model, described in Chap. 1, was used to simulate shear-thinning fluids. In this model, the dynamic viscosity is given by

$$\eta = \eta_{\infty} + (\eta_0 - \eta_{\infty}) \left[ 1 + (\lambda\dot{\boldsymbol{\gamma}})^2 \right]^{(n-1)/2}, \quad (2.10)$$

where  $\eta_{\infty}$  is the infinite shear-rate viscosity,  $\eta_0$  is the zero shear-rate viscosity and  $\eta_0 > \eta_{\infty}$  for shear-thinning,  $\lambda$  is a characteristic relaxation time, and  $n$  is a power-law index [23]. The shear rate  $1/\lambda$  characterizes the cross-over between the low shear-rate Newtonian plateau and the power-law shear-thinning region at intermediate shear rates. Fig. 2.2 shows that increasing

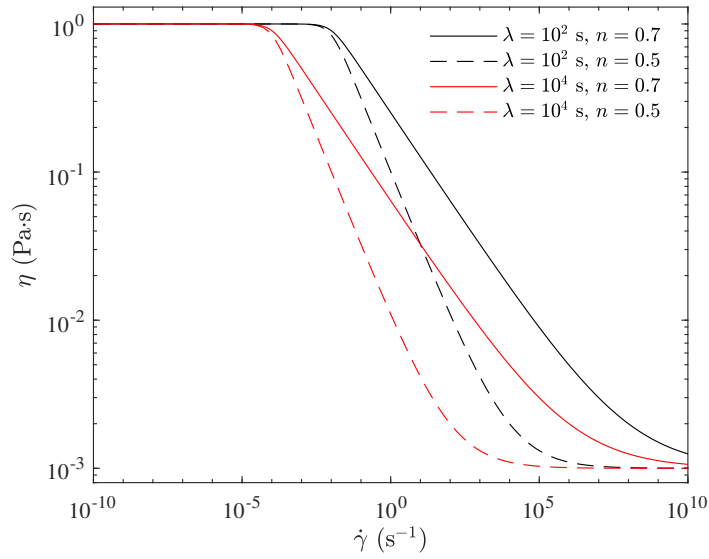


Figure 2.2: Plots of viscosity vs. shear rate for the Carreau model with  $\eta_0 = 1 \text{ Pa}\cdot\text{s}$   $\eta_\infty = 10^{-3} \text{ Pa}\cdot\text{s}$ , and several different values of  $\lambda$  and  $n$ .

$\lambda$  shifts the shear-thinning region to lower shear rates, while decreasing  $n$  decreases its slope.

To simulate the forced oscillatory motion of and the restoring force on the wire, what COMSOL refers to as a “Body Load” was applied to the simulated wire. We applied a sinusoidal driving force of the form  $\mathbf{F}_1 = F_0 \sin(2\pi ft)\hat{x}$  with amplitude  $F_0 = 5.4 \times 10^{-5} \text{ N}$ , chosen to match typical forces applied in the experiments discussed in Chap. 3. The amplitude of the driving force was held constant for each simulation. A force of the form  $\mathbf{F}_2 = -k\mathbf{r}_{\text{solid}}$  was imposed on the wire to approximate the elastic restoring force that would arise due to its tension. The constant  $k$  was chosen to be equal to  $10957 \text{ N/m}$  so that the resonant frequency of the simulated wire, determined using COMSOL’s Solid Mechanics Eigenfrequency Study, was  $1000 \text{ Hz}$ . Despite this, simulations of the wire vibrating in a fluid suggest a vacuum resonance frequency  $f_0$  of approximately  $940 \text{ Hz}$ . Summing these two contributions to the force on the wire gives

$$\mathbf{F}_a = (F_0 \sin(2\pi ft) - kx)\hat{x} - (ky)\hat{y}, \quad (2.11)$$

where  $x$  and  $y$  are the components of  $\mathbf{r}_{\text{solid}}$  in the  $\hat{x}$  and  $\hat{y}$  directions.

The driving frequency used in the simulations was increased from  $20$  to  $1400 \text{ Hz}$  in  $20$



Hz steps using COMSOL's Parametric Sweep Study. At each frequency, a time-dependent simulation was run until the motion of the wire reached a steady state. A simulated time of  $500/(25f)$  was sufficient to achieve this in most cases, but simulations involving low viscosity fluids required longer. For all simulations, the maximum time step was stipulated to be  $1/(25f)$ , although the solver was programmed to use smaller time steps when necessary to ensure convergence.

The time-dependent simulations used COMSOL's implementation of the generalized- $\alpha$  time-stepping algorithm. This algorithm was first described by Chung *et al.* for solving structural dynamics problems [24]. It was then adapted for fluid dynamics by Jansen *et al.* [25]. The generalized- $\alpha$  algorithm is unconditionally stable and provides an optimal combination of high- and low-frequency numerical dissipation [24]. We present here a simplified one-dimensional discussion of the algorithm, based on that of Jansen *et al.* [25]

Suppose the variable of interest is  $y$ , and its time-derivative is  $\dot{y}$ . For a model problem of the form

$$\dot{y} = \lambda y, \quad (2.12)$$

where  $\lambda$  is the complex-valued eigenvalue associated with the solution of the problem, the generalized- $\alpha$  algorithm integrates the model problem from  $t_n$  to  $t_{n+1}$  using the following equations:

$$\dot{y}_{n+\alpha_m} = \lambda y_{n+\alpha_f}, \quad (2.13)$$

$$y_{n+1} = y_n + (t_{n+1} - t_n)\dot{y}_n + (t_{n+1} - t_n)\gamma(\dot{y}_{n+1} - \dot{y}_n), \quad (2.14)$$

$$\dot{y}_{n+\alpha_m} = \dot{y}_n + \alpha_m(\dot{y}_{n+1} - \dot{y}_n), \quad (2.15)$$

and

$$y_{n+\alpha_f} = y_n + \alpha_f(y_{n+1} - y_n), \quad (2.16)$$

where  $\alpha_m$ ,  $\alpha_f$ , and  $\gamma$  are currently free parameters. By defining a solution vector at  $t_n$  as

$\mathbf{y}_n = [y_n, (t_{n+1} - t_n)\dot{y}_n]^T$ , the above system of equations can be written in matrix form as

$$\mathbf{y}_{n+1} = \underline{\mathbf{c}}\mathbf{y}_n, \quad (2.17)$$

where  $\underline{\mathbf{c}}$  is called the amplification matrix and is given by

$$\underline{\mathbf{c}} = \frac{1}{d} \begin{bmatrix} \alpha_m - (\alpha_f - 1)\gamma\Lambda & \alpha_m - \gamma \\ \Lambda & \alpha_m - 1 + \alpha_f\Lambda(1 - \gamma) \end{bmatrix}. \quad (2.18)$$

Here  $\Lambda = \lambda(t_{n+1} - t_n)$ , and  $d = \alpha_m - \alpha_f\gamma\Lambda$ . Eq. 2.17 has the solution

$$y_{n+1} = \text{trace}(\underline{\mathbf{c}})y_n - \det(\underline{\mathbf{c}})y_{n-1}. \quad (2.19)$$

This formulation is second-order accurate in time as long as

$$\gamma = \frac{1}{2} + \alpha_m - \alpha_f \quad (2.20)$$

and

$$\alpha_m \geq \alpha_f \geq \frac{1}{2}. \quad (2.21)$$

The values of the parameters  $\gamma$ ,  $\alpha_m$ , and  $\alpha_f$  are automatically controlled by COMSOL.

The simulations were run on the ‘‘goblin’’ contributed cluster on the Shared Hierarchical Academic Research Computing Network (SHARCNET). The cluster has 648 processors with speeds ranging from 2.0 to 2.6 GHz. A set of simulations at a fixed value of  $\eta$  (for a Newtonian fluid) or fixed values of  $\lambda$  and  $n$  (for a shear-thinning fluid), covering the full frequency range mentioned above, took approximately 4 real-time days to run.

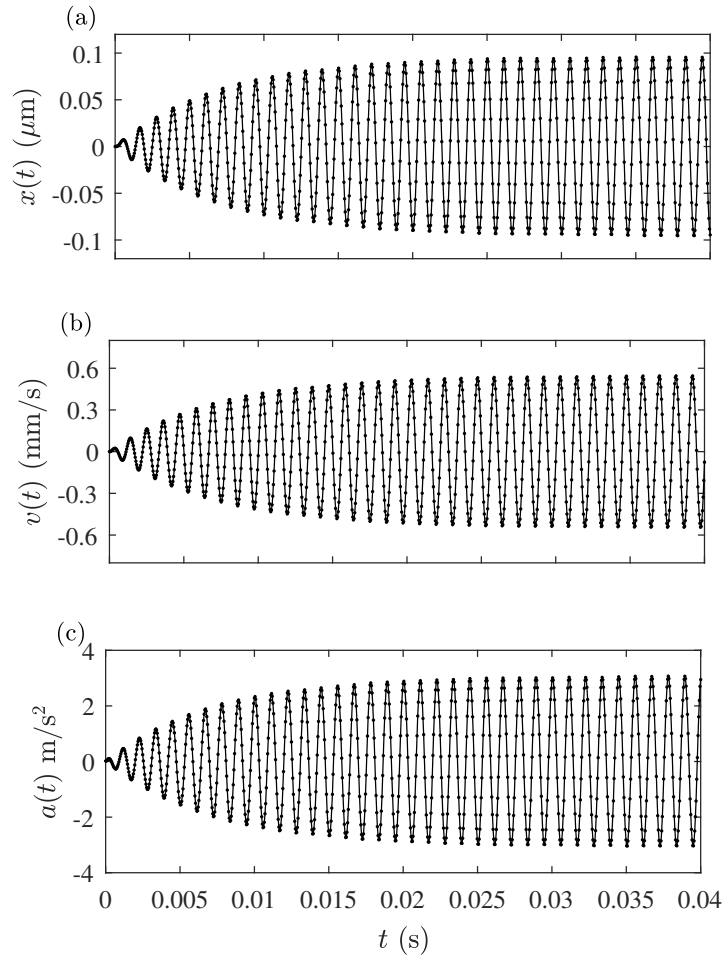


Figure 2.3: The  $x$ -components of the (a) position, (b) velocity, and (c) acceleration of the center of the wire as a function of time for a simulation of a wire vibrating in a Newtonian fluid with  $\eta = 3 \times 10^{-3}$  Pa·s and  $f = 900$  Hz. The lines connect the data points to aid the eye. Note the difference in units between the plots. The simulation time extends to 0.089 s, but only the first 0.04 s are plotted here to emphasize the early-time transient.

## 2.5 Results

### 2.5.1 Newtonian Fluids

We first present the results for the frequency-dependent behaviour of the wire vibrating in Newtonian fluids with a range of viscosities. These results will be compared with the theoretical predictions of Eq. 2.1.

At the start of each simulation, the wire is at rest with its center at the origin and the velocity in the fluid is zero everywhere. The sinusoidally varying applied force given by Eq. 2.11 drives oscillations of the wire. The amplitude of the oscillations initially increases, then approaches a constant value over a transient time that depends on the viscosity of the fluid. For each simulation, we recorded the time evolution of the position  $x(t)$ , velocity  $v(t)$ , and acceleration  $a(t)$  of the center of the wire at each time step. An example of these quantities from a simulation of a wire vibrating in a Newtonian fluid with viscosity  $\eta_{sim} = 3 \times 10^{-3}$  Pa·s and driving frequency  $f = 900$  Hz are shown in Fig. 2.3. In this case, the amplitude of the oscillations has reached its steady state value of  $0.95 \mu\text{m}$  after approximately 0.03 s of simulated time, corresponding to approximately 30 oscillations. In Fig. 2.4 we plot the velocity of the wire vs. dimensionless time  $ft$  for simulations of a wire vibrating in Newtonian fluids with  $\eta = 3 \times 10^{-3}$ ,  $3 \times 10^{-2}$ , and  $3 \times 10^{-1}$  Pa·s at driving frequencies  $f = 900$ , 840, and 660 Hz, respectively. These frequencies are close to the resonance frequency for each simulation. Fig. 2.4 illustrates that the amplitude saturates in fewer oscillations for higher viscosities.

To facilitate comparison of the results of our simulations with the predictions of Eq. 2.1, we fit eight periods of  $v(t)$  in the steady-state of each simulation to a sinusoid with the form

$$v(t) = v_0 \sin(2\pi ft + \phi), \quad (2.22)$$

where the velocity amplitude  $v_0$ , the phase angle  $\phi$ , and the frequency  $f$  were all treated as fit parameters. In all cases the fitted frequency was equal to the driving frequency within  $\pm 0.1$  Hz. A fit of Eq. 2.22 to the data plotted in Fig. 2.3(b) is shown in Fig. 2.5, and describes the data extremely well.

Plots of  $v_0$  vs.  $f$  obtained from simulations of a wire vibrating in Newtonian fluids with viscosities ranging from  $10^{-3}$  Pa·s to 1 Pa·s are shown in Fig. 2.6. For  $\eta_{sim} = 10^{-3}$  Pa·s, i.e., the viscosity of water, the resonance curve is sharply peaked at a resonant frequency  $f_r = 900$  Hz, slightly lower than the vacuum resonance frequency  $f_0 = 940$  Hz. As the viscosity is

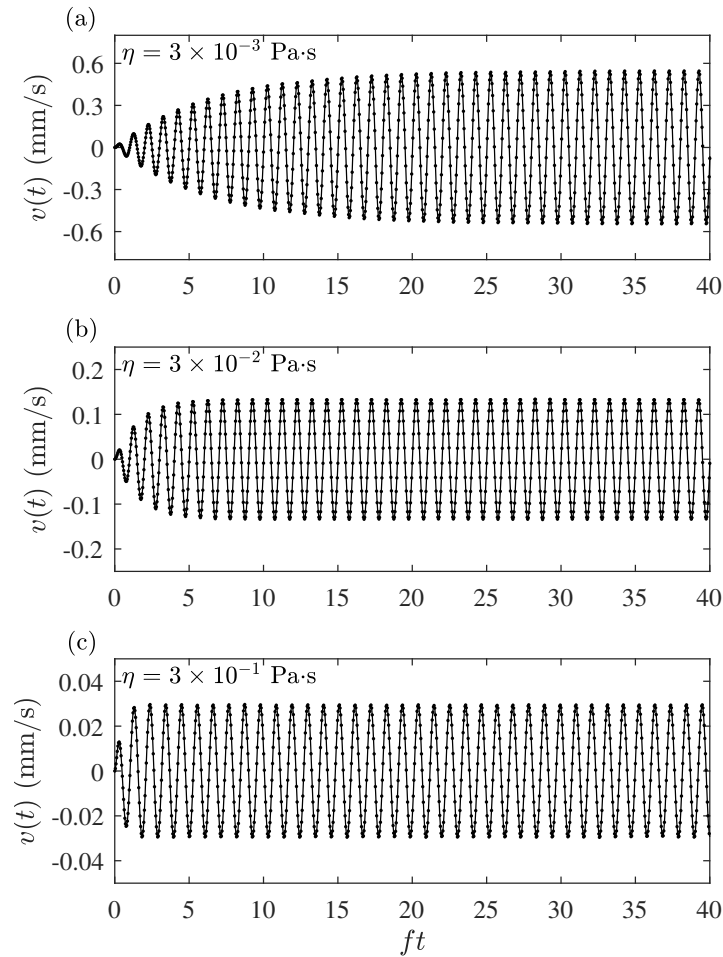


Figure 2.4: The velocity in the  $x$  direction of the center of the wire vs. normalized time  $ft$  for simulations of a wire vibrating in a Newtonian fluid at a frequency near the resonance frequency with a)  $\eta_{sim} = 3 \times 10^{-3}$ , b)  $\eta_{sim} = 3 \times 10^{-2}$ , and c)  $\eta_{sim} = 3 \times 10^{-1}$  Pa·s. The early-time transient damps out faster for higher viscosities.

increased,  $f_r$  shifts to lower frequency and the resonance peak broadens due to the higher viscous dissipation, as expected. The resonance curves for the simulations with the largest viscosities are magnified in the inset of Fig. 2.6.

We quantitatively describe the resonance curves by three parameters: the resonance frequency  $f_r$ , the full width at half maximum  $\Delta f$ , and the quality factor  $Q = f_r/\Delta f$ .  $f_r$  was calculated by fitting three points spanning the peak to a quadratic equation in vertex form,  $v = a(f - f_r)^2 + v_{max}$ . The values of  $f_r$ ,  $\Delta f$ , and  $Q$  obtained from the simulations of the wire

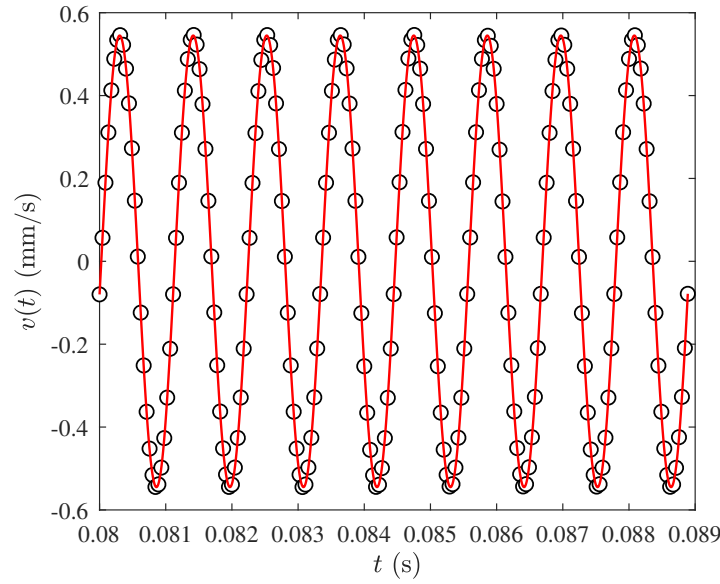


Figure 2.5: Example fit of Eq. 2.22 (red curve) to the late-time velocity data from Fig. 2.3 (b).

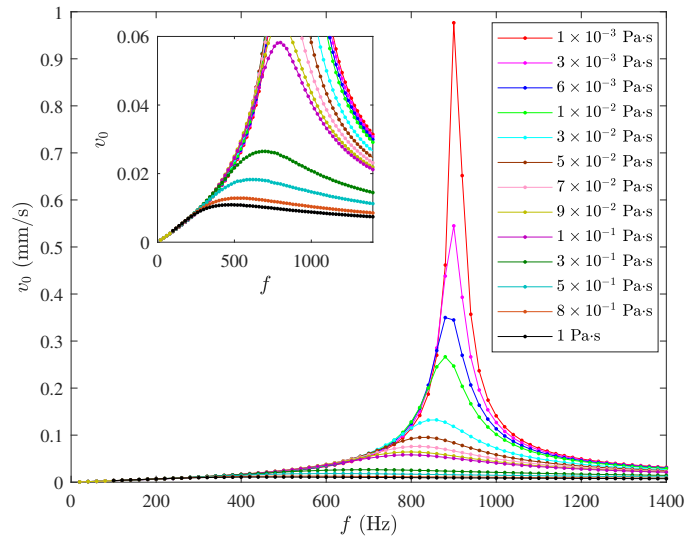


Figure 2.6: The velocity resonance curves for the Newtonian-fluid simulations with viscosities shown in the legend. The inset is a magnified view of the smaller-amplitude resonance curves obtained at higher viscosities. The lines connect the data points to aid the eye.

vibrating in Newtonian fluids are plotted as functions of  $\eta_{sim}$  in Fig. 2.7. Theoretical predictions determined by applying the same analysis to resonance curves calculated from Eq. 2.1 with  $f_0 = 940$  Hz are shown as the black curves in Fig. 2.7. The simulation and theory agree extremely well.

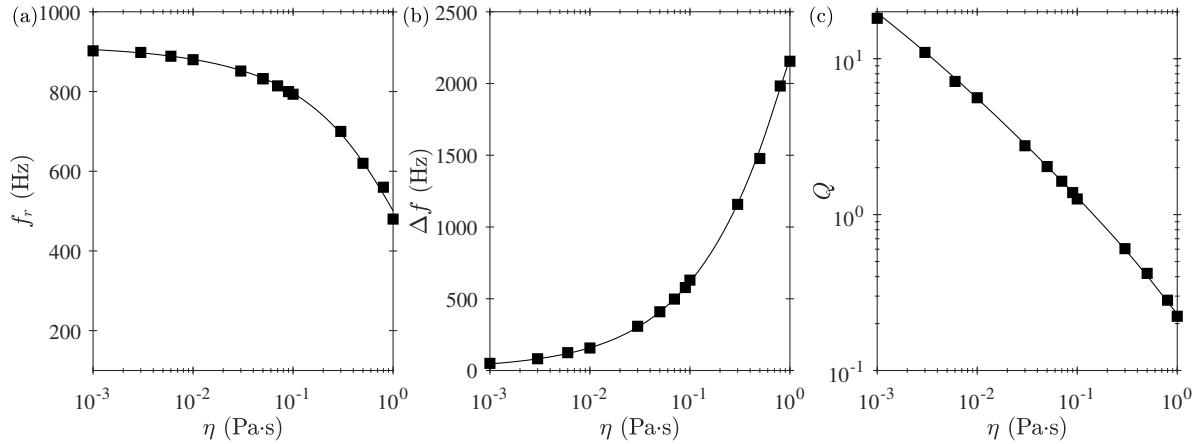


Figure 2.7: (a) The resonant frequency  $f_r$ , (b) the full width at half maximum  $\Delta f$ , and (c) the quality factor  $Q$  vs.  $\eta$  for simulations of a wire vibrating in a Newtonian fluid. The curves in each plot are theoretical predictions calculated using Eq. 2.1.

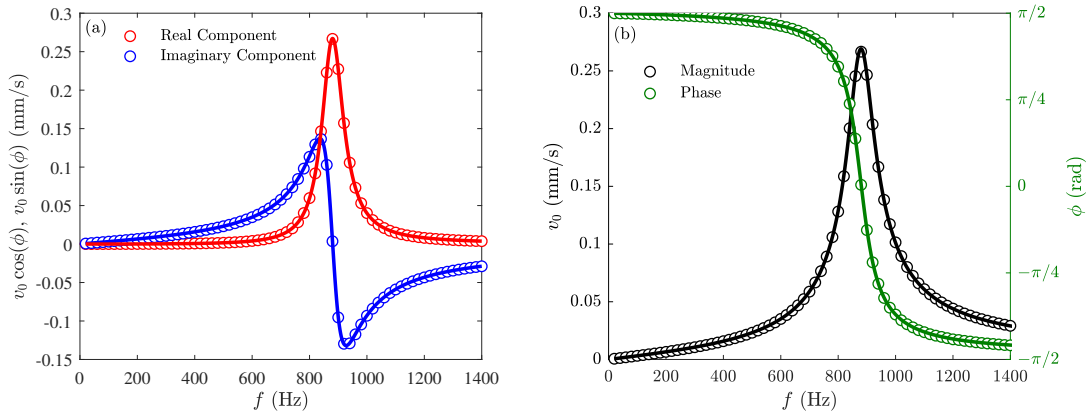


Figure 2.8: (a) Real and imaginary components, and (b) magnitude and phase of the simulated velocity of a wire vibrating in a Newtonian fluid with  $\eta = 10^{-2}$  Pa·s plotted vs. frequency. The lines are fits of Eq. 2.1 to the data.

The resonance curves were also analysed by fitting Eq. 2.1 to the simulated data. To remain consistent with the procedure used in Chap. 3,  $F$ ,  $f_0$  and  $\eta$  were treated as fit parameters, although all three parameters are actually set in the simulation. For all simulations, the fits return values for  $F$  and  $f_0$  that are within 10% of their expected values. We focus now on the fitted viscosity, which we refer to as  $\eta_{fit}$ . Since Eq. 2.1 is complex, we can compare its predictions for the real component, imaginary component, magnitude, and phase of the velocity to the corresponding simulation results. These quantities, determined from simulations of a wire vibrating in a Newtonian fluid with  $\eta_{sim} = 10^{-2}$  Pa·s, are plotted in Fig. 2.8, along with

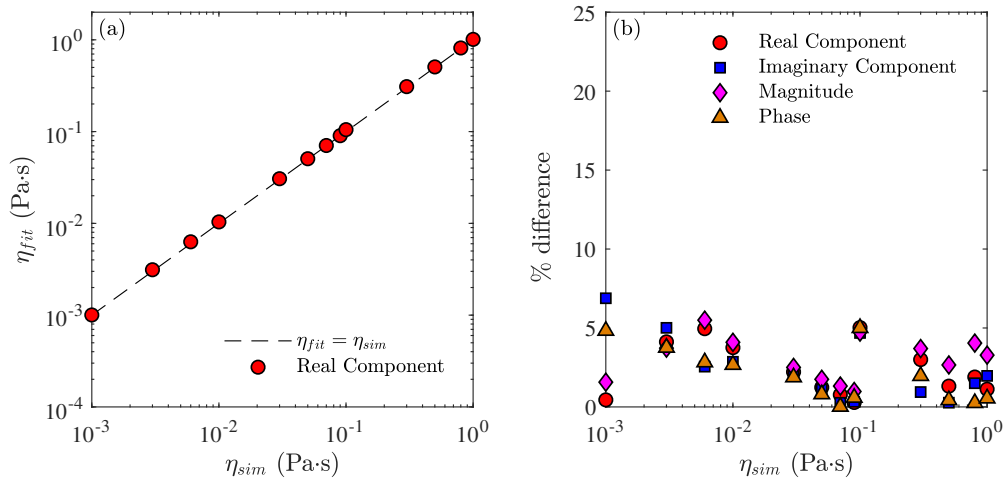


Figure 2.9: (a)  $\eta_{fit}$  vs.  $\eta_{sim}$  from fits of the real component of Eq. 2.1 to the real component of the resonance curves for simulations of a wire vibrating in a Newtonian fluid. (b) The magnitude of the % difference between  $\eta_{fit}$  and  $\eta_{sim}$  vs.  $\eta_{sim}$ .

independent fits of Eq. 2.1 to each quantity. The quality of the fits shown in Fig. 2.8 is excellent, and Fig. 2.9 shows that the viscosity  $\eta_{fit}$  extracted from the four independent fits agree with each other to within a few percent. For all simulated viscosities  $\eta_{sim}$ , the magnitude of the difference between  $\eta_{fit}$  and  $\eta_{sim}$  is always less than 10%.

## 2.5.2 Shear-thinning fluids

For simulations of a wire vibrating in shear-thinning fluids, the fluid space shown in Fig. 2.1(a) was defined to be a Carreau fluid described by Eq. 2.10 with  $\eta_{\infty} = 10^{-3}$  Pa·s and  $\eta_0 = 1$  Pa·s.  $n$  and  $\lambda$  were varied to investigate how the strength of the shear-thinning (determined by  $n$ ) and the crossover shear rate  $1/\lambda$  — as illustrated in Fig. 2.2 — affect the motion and resonant behaviour of the wire. We performed simulations using five values of  $n$ , linearly spaced from 0.5 to 0.9, and five values of  $\lambda$ , logarithmically spaced from  $10^0$  to  $10^4$  s.

The motion of the wire produces a flow in the fluid that varies in both space and time. This is true for both Newtonian and non-Newtonian fluids, but for Newtonian fluids the viscosity of the fluid is independent of shear rate and so remains constant under all conditions. For shear-thinning fluids, however, the spatio-temporal variation of the shear rate implies that the



viscosity of the fluid also varies in both space and time. This will affect the motion of the wire in the shear-thinning case.

A series of snapshots of the velocity of the fluid taken from a simulation of a wire vibrating in a Carreau fluid with  $n = 0.5$  and  $\lambda = 10^2$  s are shown in Fig. 2.10. The frequency used in this simulation was 660 Hz, which was slightly above the wire's resonant frequency, as discussed below. At the time shown in Fig. 2.10 (a), the wire is moving in the  $-x$  direction with a speed near its maximum value. Because of the no-slip boundary condition, the fluid everywhere along the wire's surface is moving with the same velocity as the wire: it is being pushed to the left, pulled from the right, and dragged to the left above and below the wire. The velocity of the fluid rapidly decreases with distance away from the wire and circulates above and below the wire.

Snapshots of the shear rate in the fluid corresponding to the velocity data plotted in Fig. 2.10 are shown in Fig. 2.11. The spatial variation of the shear rate takes the shape of a dumbbell oriented along the direction of the wire's motion, i.e., along the  $x$  axis. For the simulation shown, the shear rate in the fluid varies spatially by 5 orders of magnitude. With the exception of the time shown in Fig. 2.11 (c), the shear rate is highest near the wire and, in general, decreases with distance away from the wire. In the  $y$  direction, the velocity decreases over a relatively short distance, as shown in Fig. 2.10 (a), which results in a high shear rate near the wire. The velocity of the fluid decreases over a longer distance in the  $x$  direction, which contributes to the length of the shear-rate lobes in the  $x$  direction. The lobes extend in the  $y$  direction due to circulation of the fluid above and below the wire.

At the time shown in subplot (c), the shear rate is small near the wire because the wire and fluid are moving in the same direction with approximately the same velocity, as shown in Fig. 2.10 (c).  $\dot{\gamma}$  is larger in a region away from the wire due to the decrease in the velocity of the fluid with increasing distance from the wire. In subplot (d), although the fluid velocity is small near the wire (Fig. 2.10 (d)), the wire is moving to the right, against the flow, which contributes to the high shear rate near the wire shown in Fig. 2.11 (d).

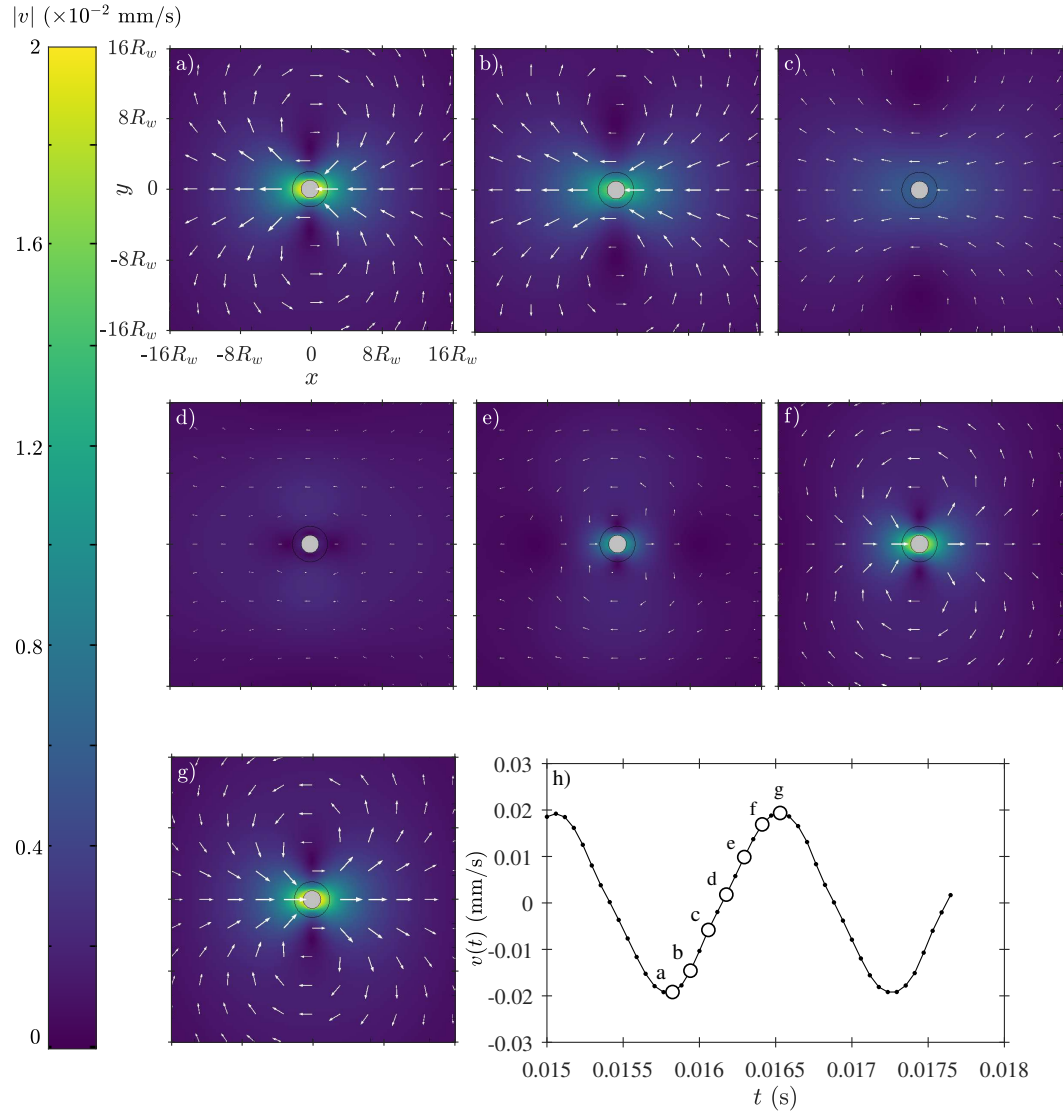


Figure 2.10: Snapshots from a simulation of a wire vibrating in the  $x$  direction in a shear-thinning fluid described by Eq. 2.10 with  $n = 0.5$  and  $\lambda = 10^2$  s. The wire was driven at  $f = 680$  Hz, which was close to its resonant frequency. (a) - (g) show the spatial variation of the velocity of the fluid near the wire at times covering a half-period of the wire's oscillation. The magnitude of the velocity is given by the surface plot, while the arrows show velocity direction and logarithmic magnitude. (h)  $v(t)$ , the velocity of the vibrating wire. The labelled time points in (h) indicate the times of the corresponding velocity plots. The coordinate system is explicitly labelled in subplot (a). A video showing the full domain and all times for this simulation is included in the supplementary media.

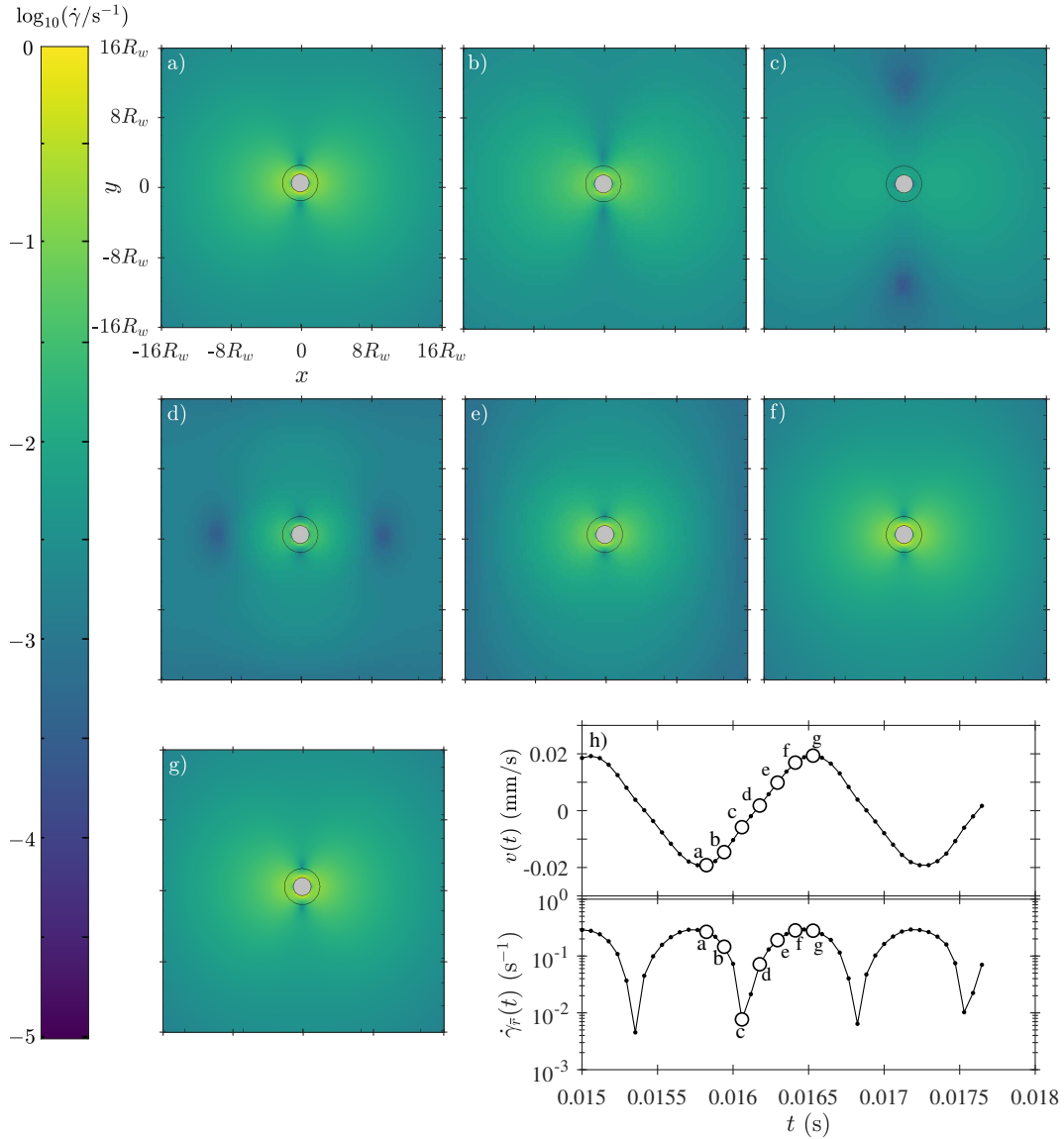


Figure 2.11: Snapshots from a simulation of a wire vibrating in the  $x$  direction in a shear-thinning fluid described by Eq. 2.10 with  $n = 0.5$  and  $\lambda = 10^2$  s. The wire was driven at  $f = 680$  Hz, which was close to its resonant frequency. (a) - (g) show the spatial variation of the shear rate near the wire at times covering a half-period of the wire's oscillation. (h)  $v(t)$ , the velocity of the vibrating wire. (i)  $\dot{\gamma}_{\bar{r}}(t)$ , the shear rate averaged around the circumference of the wire, as described in the text. The labelled time points in (h) and (i) indicate the times of the corresponding shear rate plots. The coordinate system is explicitly labelled in subplot (a). A video showing the full domain and all times for this simulation is included in the supplementary media.

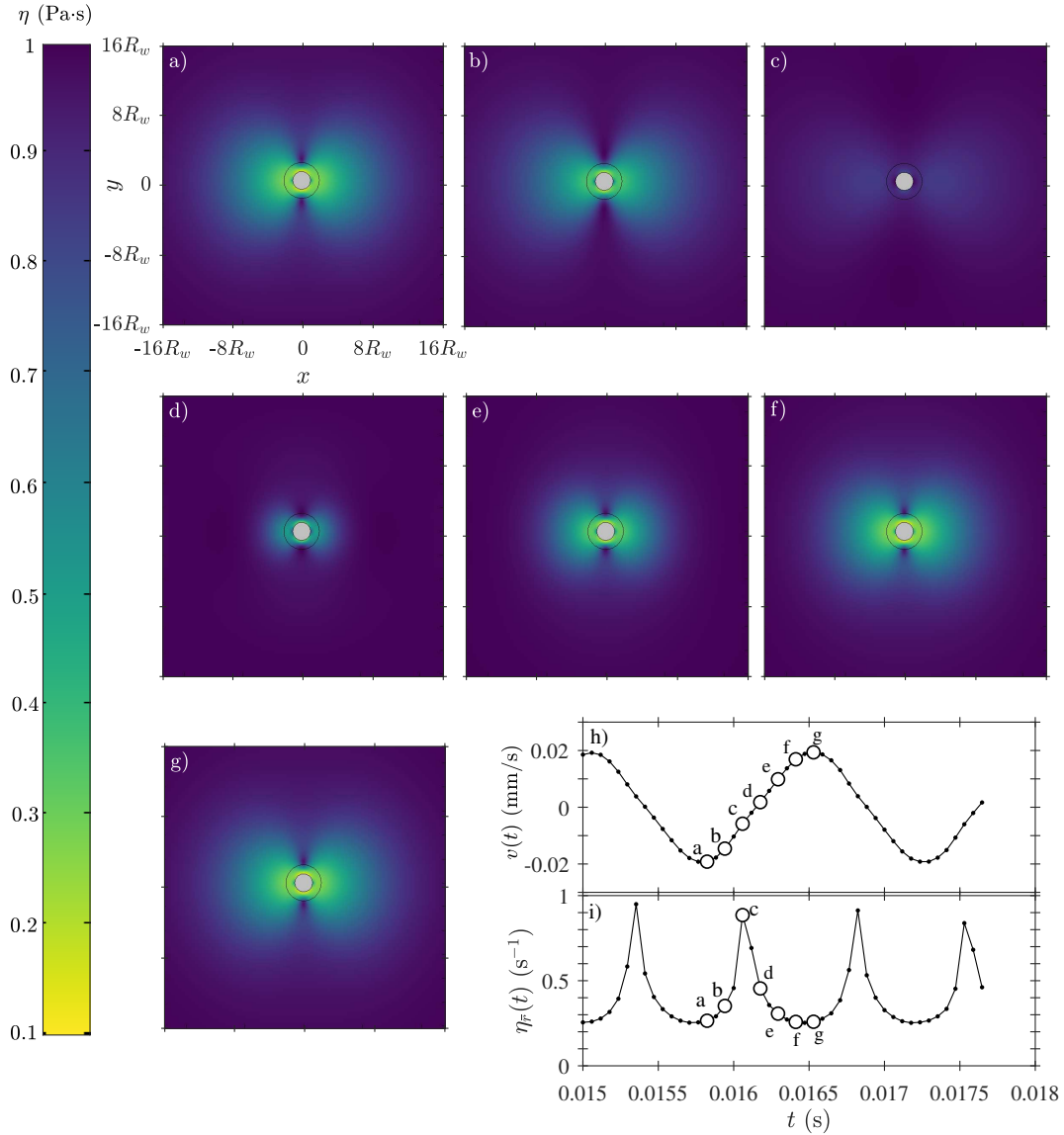


Figure 2.12: Snapshots from a simulation of a wire vibrating in the  $x$  direction in a shear-thinning fluid described by Eq. 2.10 with  $n = 0.5$  and  $\lambda = 10^2$  s. The wire was driven at  $f = 680$  Hz, which was close to its resonant frequency. (a) - (g) show the spatial variation of the viscosity near the wire at times covering a half-period of the wire's oscillation. (h)  $v(t)$ , the velocity of the vibrating wire. (i)  $\eta_{\bar{r}}(t)$ , the viscosity averaged around the circumference of the wire, as described in the text. The labelled time points in (h) and (i) indicate the times of the corresponding viscosity plots. The coordinate system is explicitly labelled in subplot (a). A video showing the full domain and all times for this simulation is included in the supplementary media.

Since the viscosity of the fluid depends on shear rate according to Eq. 2.10, it will also vary with position and time. Snapshots of the viscosity variation corresponding to the shear rate and velocity data plotted in Figs. 2.10 and 2.11 are shown in Fig. 2.12. As with the shear rate, the spatial variation of the viscosity takes the form of a dumbbell with lobes that extend away from the wire in the direction of its motion, the  $x$  direction. The shear rate and viscosity along the line  $y = 0$  at the time corresponding to Fig. 2.12 (a) are shown as red and black curves, respectively, in Fig. 2.13 (a). The shear rate is small near the surface of the wire and initially increases rapidly with distance away from the wire in the  $x$  direction before gradually decreasing again. Since  $\lambda = 10^2$  s for this simulation, the characteristic cross-over shear rate between the low shear-rate Newtonian region and the intermediate shear-thinning region is  $1/\lambda = 10^{-2}$  s $^{-1}$ . Along the line  $y = 0$ , within  $|x| < 1$  mm, the shear rate is greater than  $10^{-2}$ . As a result, the viscosity is appreciably less than 1 Pa-s close to the wire and is smaller where the shear rate is higher. The viscosity and shear rate along the line  $x = 0$  show a more complex dependence on distance from the wire, as plotted in Fig. 2.13 (b). In this direction, the shear rate is large at the surface of the wire, decreases rapidly to a minimum, then shows another maximum further from the wire. The viscosity is correspondingly smallest near the surface of the wire where the shear rate is highest, then passes through a maximum and a local minimum before increasing to its low-shear-rate value far from the wire.

To facilitate comparison with the single value of viscosity that will be obtained by fitting Eq. 2.1 to the velocity resonance curves, it is useful to define an average viscosity appropriate to our simulation results. At each point in time we average the shear rate and viscosity around the circumference of the wire and denote the resulting spatial averages as  $\dot{\gamma}_{\bar{r}}(t)$  and  $\eta_{\bar{r}}(t)$ . These quantities are plotted in Figs. 2.11 and 2.12 (i), respectively. At the time corresponding to subplots (c),  $\dot{\gamma}_{\bar{r}}(t)$  reaches a minimum and  $\eta_{\bar{r}}(t)$  a maximum. We then evaluate the time average of  $\eta_{\bar{r}}(t)$  over one period of the late-time, steady-state oscillations of the wire. The resulting spatiotemporally averaged viscosity, which is a function of frequency as well as the shear-thinning parameters, is denoted  $\bar{\eta}(f)$ . The dependence of  $\bar{\eta}(f)$  on the shear-thinning parameters

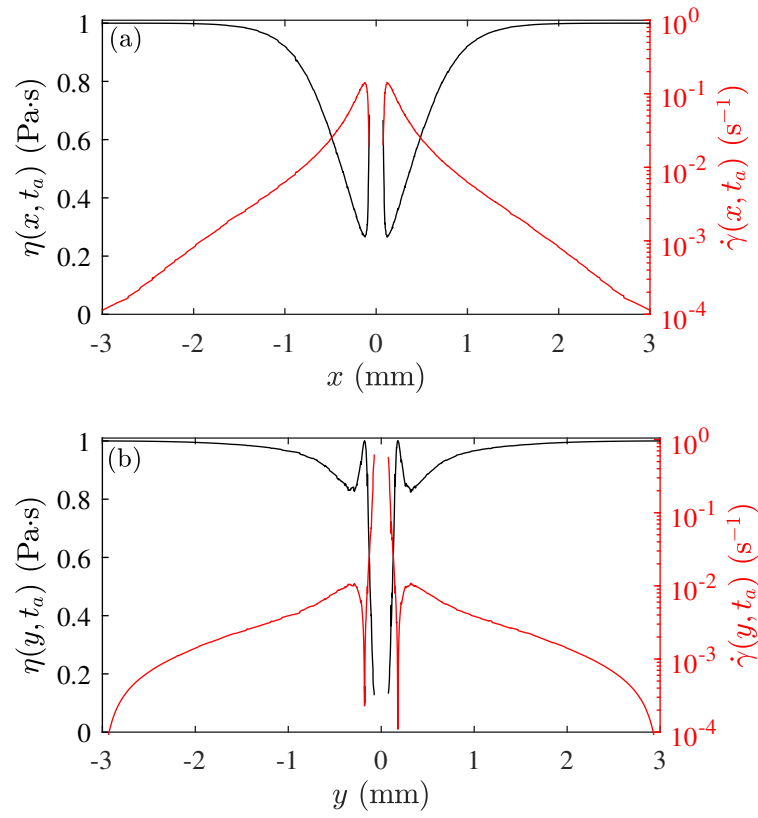


Figure 2.13: Fluid viscosity and shear rate as a function of (a)  $x$ , along the line  $y = 0$ , and (b)  $y$ , along the line  $x = 0$ , at the time of Fig. 2.12 (a). The gap in the data in the center of each plot corresponds to the location of the wire.

is discussed below.

As was found in the simulations using a Newtonian fluid, the sinusoidally-varying force applied to the wire results in steady-state oscillatory motion following an initial transient. In Fig. 2.14 we plot the velocity of the wire vs.  $ft$  for simulations of a wire vibrating in shear-thinning fluids described by the Carreau model (Eq. 2.10) with different  $n$  and  $\lambda$  values. As above, the duration of the transient depended on the viscosity of the fluid. In the shear-thinning case, however, the viscosity was not constant, and the oscillations took longer to reach steady state for lower  $n$  and/or greater  $\lambda$ . The amplitude of the velocity-time curves was again dependent on frequency and showed resonant behaviour similar to that seen in the simulations of the wire vibrating in Newtonian fluids. For the most part, the steady-state oscillations were

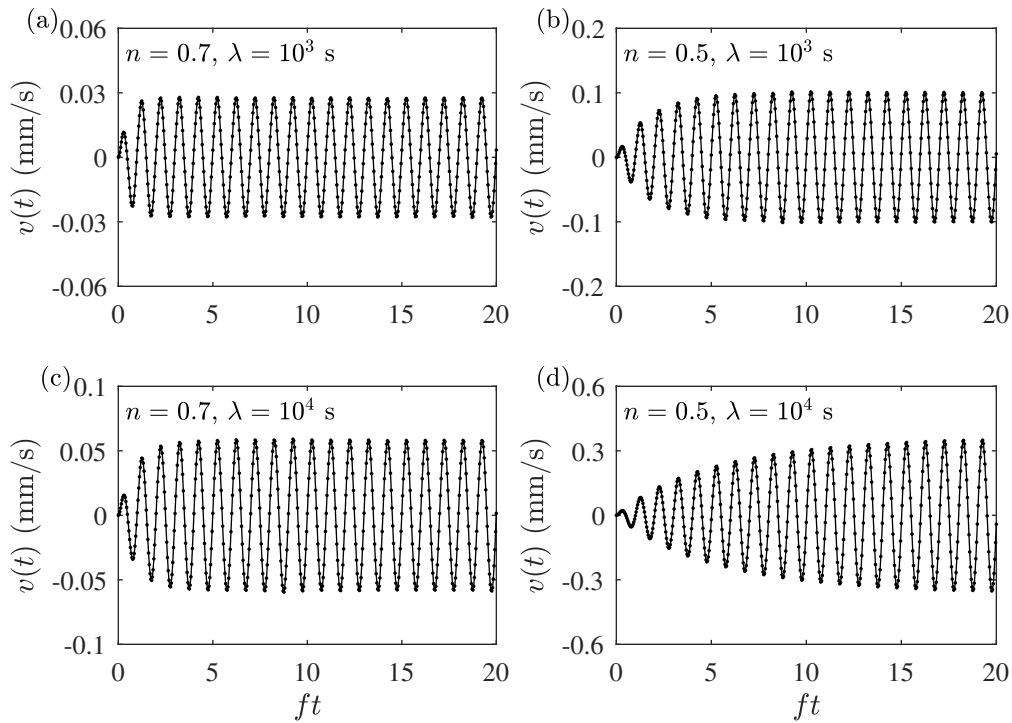


Figure 2.14: The velocity in the  $x$  direction of the center of the wire vs. normalized time  $ft$  for simulations of a wire vibrating in a shear-thinning fluid described by the Carreau model (Eq. 2.10) with (a)  $n = 0.7$ ,  $\lambda = 10^3$  s, (b)  $n = 0.5$ ,  $\lambda = 10^3$  s, (c)  $n = 0.7$ ,  $\lambda = 10^4$  s, and (d)  $n = 0.5$ ,  $\lambda = 10^4$  s. Note that for the simulation in subplot (d), the simulation time extends to  $ft = 40$ , but only the first 20 oscillations are plotted here to emphasize the early-time transient.

sinusoidal. In a few cases slight deviations from sinusoidal behavior were observed. Despite this, Eq. 2.22 was fit to  $v(t)$  for every simulation performed to determine the amplitude and phase of the velocity.

The velocity resonance curves for the wire vibrating in the shear-thinning fluids were calculated in the same manner as for the Newtonian case. The resonance curves and  $\bar{\eta}(f)$  for all of the shear-thinning fluids simulated are plotted in Fig. 2.15. In this figure,  $n$  decreases from top to bottom and  $\lambda$  increases from left to right. The resonance curves show the same general trend as a function of average viscosity as was seen the simulations with Newtonian fluids. This can be seen, for example, in the bottom row of Fig. 2.15. As  $\lambda$  decreases from right to left, the average viscosity seen by the wire increases and as a result the resonance shifts to lower frequency and broadens. Similarly, for a given value of  $\lambda$ , the average viscosity increases and

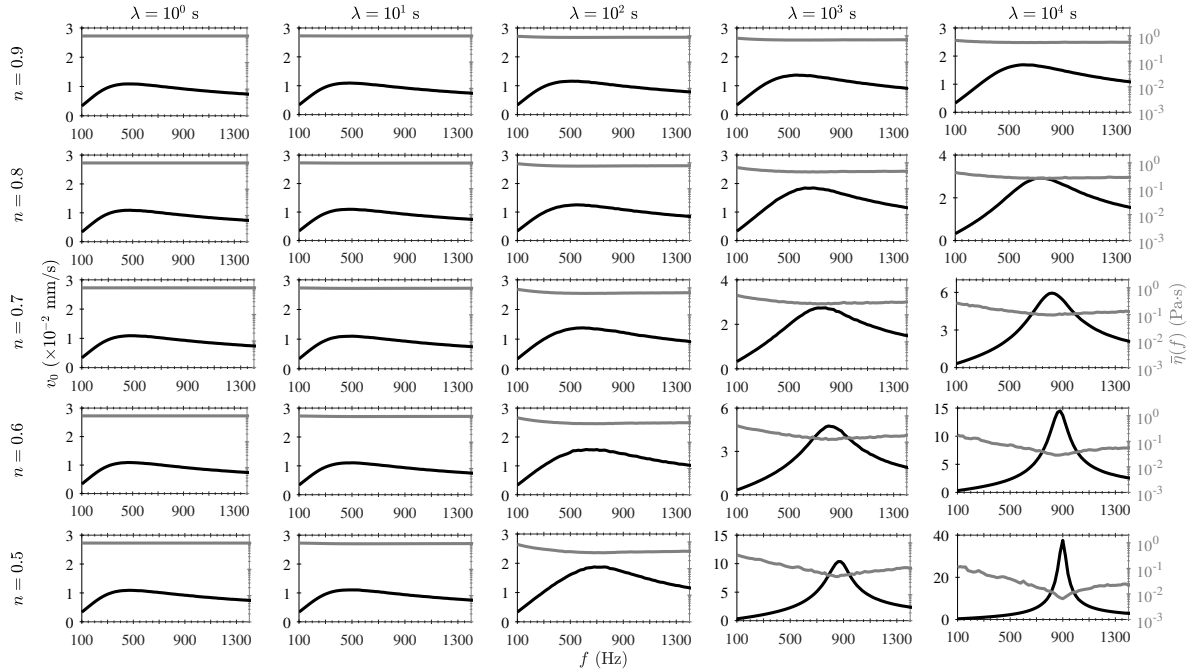


Figure 2.15: Velocity resonance curves (black curves) and the spatiotemporal average viscosity  $\bar{\eta}(f)$  (gray curves), for the full parameter space covered by our shear-thinning simulations. Note the difference in velocity scale between subplots.

the peak broadens as  $n$  increases. Although the data for  $\lambda = 10^0$  s and  $10^1$  s look very similar, there are in fact subtle differences in the velocity and viscosity curves that are difficult to see by eye in Fig. 2.15.

The effect of shear-thinning on  $\bar{\eta}(f)$  is most evident for  $\lambda = 10^4$  s, the highest value of  $\lambda$  studied. These results are plotted in the right-most column of Fig. 2.15. For  $n = 0.9$ , which corresponds to weak shear thinning, the average viscosity decreases only slightly with increasing frequency. As  $n$  is decreased and the fluid becomes more strongly shear-thinning, the variation in  $\bar{\eta}(f)$  becomes more pronounced, and  $\bar{\eta}(f)$  shows a clear minimum at the resonant frequency. In fact, this minimum is present for all values of  $\lambda > 10^0$  s, although it is difficult to discern in the figure in most cases. For  $\lambda = 10^0$  s,  $\bar{\eta}(f)$  deviates only very slightly from  $\eta_0 = 1$  Pa.s at all frequencies and for all values of  $n$ . As the onset of shear-thinning is moved to higher rates, i.e., as  $1/\lambda$  is increased, the viscosity at a given shear-rate will be larger. The dependence of the spatiotemporal average viscosity at the resonant frequency  $\bar{\eta}(f_r)$  on  $n$  and  $1/\lambda$  is shown in



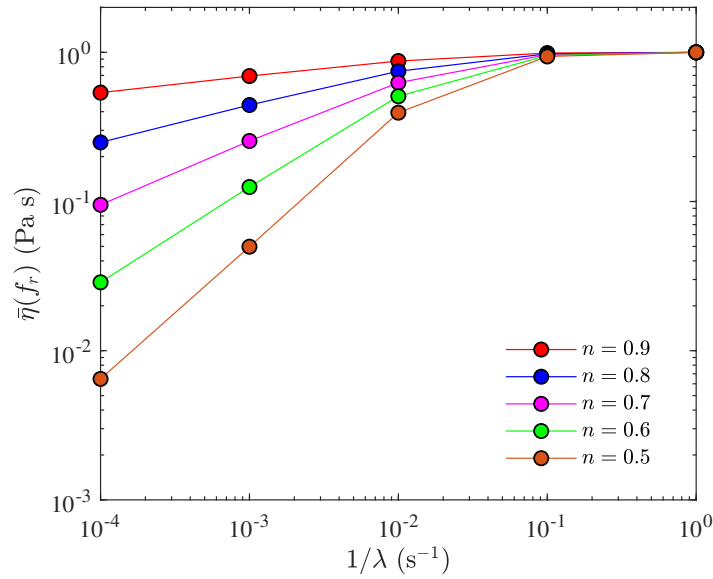


Figure 2.16:  $\bar{\eta}(f_r)$  plotted against  $1/\lambda$  for simulations of a wire vibrating in shear-thinning fluids.

Fig. 2.16. At a fixed  $n$ , as  $1/\lambda$  is increased,  $\bar{\eta}(f_r)$  increases. Similarly, at a fixed  $1/\lambda$ , as  $n$  is increased,  $\bar{\eta}(f_r)$  increases.

The velocity resonance curves plotted in Fig. 2.15 were analyzed in the same way as the results obtained for Newtonian fluids. The dependence of the resonant frequency  $f_r$ , the full width at half maximum  $\Delta f$ , and the quality factor  $Q$  on  $n$  and  $1/\lambda$  is shown in Fig. 2.17. At a fixed  $n$ , as  $1/\lambda$  is increased, i.e., as the onset of shear thinning is moved to higher rates,  $f_r$  decreases,  $\Delta f$  increases, and  $Q$  decreases. For  $1/\lambda = 10^{-1} \text{ s}^{-1}$ ,  $f_r$  depends weakly on  $n$ , which suggests that the maximum shear rate in the fluid is close to the cross-over shear rate  $1/\lambda$ ; the fluid shear thins slightly, but the shear rate is not high enough for the viscosity to decrease significantly. For  $1/\lambda = 10^0 \text{ s}^{-1}$ ,  $f_r$  is independent of  $n$ . The apparent scatter in  $\Delta f$  at  $1/\lambda = 10^{-1}$  and  $10^0 \text{ s}^{-1}$  is probably an approximation issue since the full width of the resonance curves extends beyond the simulated frequency range. For the simulation with  $1/\lambda = 10^0 \text{ s}^{-1}$ , the lack of dependence of  $f_r$  on  $n$  suggests that the shear rate in the fluid is always less than  $1/\lambda$  and that shear thinning does not occur.

In Fig. 2.18 we plot  $f_r$ ,  $\Delta f$ , and  $Q$  as functions of  $\bar{\eta}(f_r)$ , the spatially-averaged viscosity at

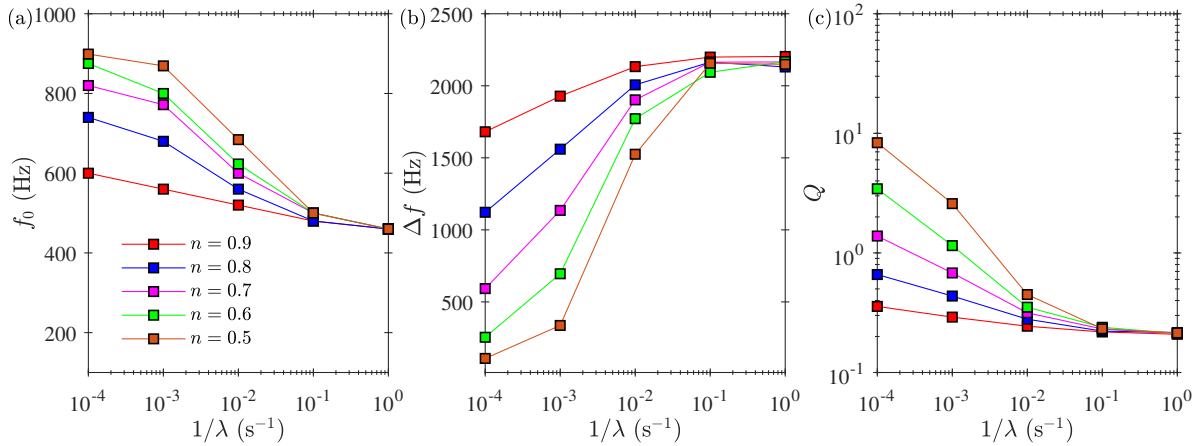


Figure 2.17: (a) The resonant frequency  $f_r$ , (b) the full width at half maximum  $\Delta f$ , and (c) the quality factor  $Q$  plotted against  $1/\lambda$  for the simulations of a wire vibrating in shear-thinning fluids.

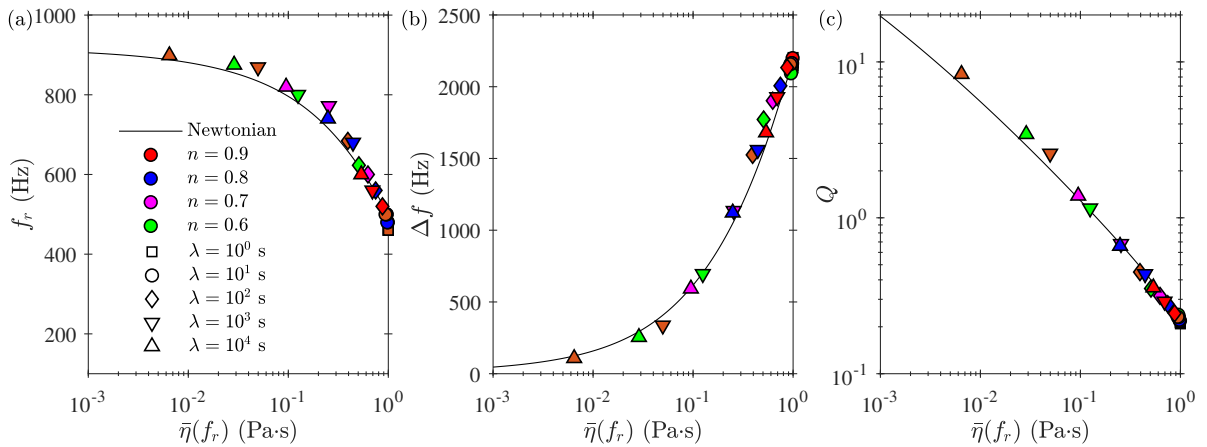


Figure 2.18: (a) The resonant frequency  $f_r$ , (b) the full width at half maximum  $\Delta f$ , and (c) the quality factor  $Q$  for the simulations of a wire vibrating in shear-thinning fluids plotted against  $\bar{\eta}(f_r)$  and compared to the theoretical predictions calculated from Eq. 2.1 (black curves).

the resonant frequency. We also compare the results to the theoretical prediction for a Newtonian fluid calculated from Eq. 2.1, taking the constant viscosity in Eq. 2.1 to be  $\bar{\eta}(f_r)$ . Using  $\bar{\eta}(f_r)$  as an effective viscosity results in good agreement between the simulation results and the theory.

We also fit Eq. 2.1 to the shear-thinning resonance curves, allowing  $F$ ,  $f_0$ , and  $\eta_{fit}$  to be fit parameters as before. Independent fits of Eq. 2.1 to the real component, imaginary component, magnitude, and phase of the simulated resonance curve for the wire vibrating in a

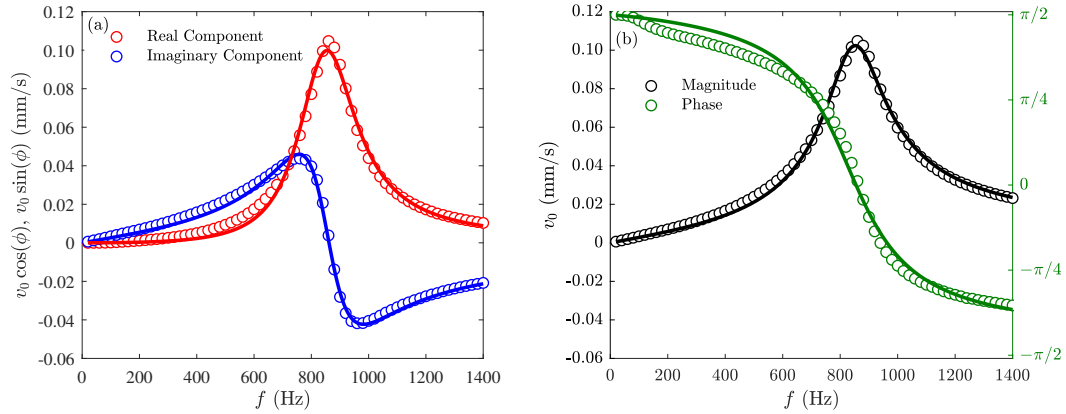


Figure 2.19: (a) Real and imaginary components, and (b) the magnitude and phase of the of the velocity vs. frequency with fits of Eq. 2.1 to each component for the simulation of a wire vibrating in a shear-thinning fluid with  $n = 0.5$  and  $\lambda = 10^3$  s.

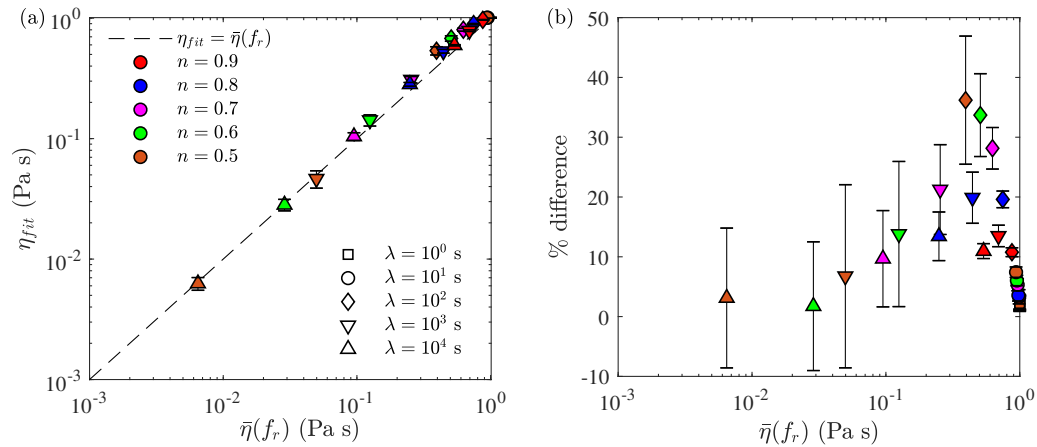


Figure 2.20: (a)  $\eta_{fit}$  vs.  $\bar{\eta}(f_r)$  for the simulations of a wire vibrating in shear-thinning fluids. Results with the same  $n$  are plotted with the same colour, and the same  $\lambda$  are plotted with the same symbol. (b) The magnitude of the % difference between the two viscosities vs.  $\bar{\eta}(f_r)$ . The error bars are the standard deviation between the  $\eta_{fit}$  values determined by independent fits of the components of the resonance curves to Eq. 2.1.

shear-thinning fluid with  $n = 0.5$  and  $\lambda = 10^3$  s are shown in Fig. 2.19. While the quality of the fits is reasonable, they do not accurately reproduce the resonance curves over the full frequency range of the simulations. The largest discrepancies occur at frequencies below the resonance peak, at which the fits underestimate the real and imaginary components and magnitude of the simulated data while overestimating the simulated phase. As was the case when fitting to the resonance curves of the wire vibrating in Newtonian fluids, the values of  $\eta_{fit}$  obtained

from independent fits to the real part, imaginary part, magnitude, and phase of  $v$  were similar. The fitted viscosity  $\eta_{fit}$  is plotted against  $\bar{\eta}(f_r)$  for each of the non-Newtonian simulations in Fig. 2.20 (a). The data points are the average of the values of  $\eta_{fit}$  extracted from the four independent fits and the error bars are the standard deviation. As shown in Fig. 2.20 (b),  $\eta_{fit}$  and  $\bar{\eta}(f_r)$  agree to within 20% when the degree of shear thinning is large, i.e., for large  $\lambda$  or small  $n$ . At intermediate values for  $\lambda$  and  $n$ ,  $\eta_{fit}$  and  $\bar{\eta}(f_r)$  disagree up to approximately 50%. When the shear thinning is weaker, i.e., for small  $\lambda$  or large  $n$ ,  $\eta_{fit}$  and  $\bar{\eta}(f_r)$  agree to within 10%.

## 2.6 Discussion

Our simulations of a wire vibrating in a Newtonian fluid showed resonant behaviour, as expected. We found good agreement between the resonant frequency  $f_r$ , full width at half maximum  $\Delta f$ , and quality factor  $Q$  determined from our simulations and theoretical predictions based on Eq. 2.1 for all viscosities simulated. Eq. 2.1 described the simulated resonance curves extremely well, and the viscosities obtained by fitting the theoretical equation to the simulated resonance curves agreed within 10% with the viscosities used in the simulations. We verified that our numerical solutions were not affected by changes to the computational mesh or convergence criterion. The good agreement between our simulations and the theory gives us confidence that the vibrating-wire rheometer studied in Chap. 3 should accurately measure viscosities up to approximately 1 Pa·s.

Our simulations of a wire vibrating in shear-thinning Carreau fluids showed that the shear rate and viscosity of the fluid vary significantly both spatially throughout the computational domain and in time over the period of the vibrations. Since the motion of the wire depends on fluid viscosity, this spatiotemporal variation in the viscosity will modify the behaviour of the wire. Our simulations also showed that the velocity of the wire exhibits resonant behaviour that can be understood fairly well in terms of an effective viscosity  $\bar{\eta}(f)$  determined by averaging the viscosity around the circumference of the wire and over one period of oscillation. Our results

showed that  $\bar{\eta}(f)$  depended non-trivially on the driving frequency and reached a minimum at the resonant frequency, when the average shear rate in the fluid near the wire was highest. We attempted to model the shear-thinning fluids by using the spatiotemporal average viscosity at the resonant frequency  $\bar{\eta}(f_r)$  in Eq. 2.1, which was derived for a Newtonian fluid. Our results showed that the predictions of  $f_r$ ,  $\Delta f$ , and  $Q$  from using  $\bar{\eta}(f_r)$  in Eq. 2.1 agree reasonably well with the results from the simulations. For  $\bar{\eta}(f_r) \leq 0.4$  Pa·s,  $f_r$  at a given effective viscosity is slightly larger than the resonant frequency of a wire vibrating in a Newtonian fluid with  $\eta = \bar{\eta}(f_r)$ . For  $\bar{\eta}(f_r) > 0.4$  Pa·s,  $f_r$  is smaller than the Newtonian prediction. Similarly, for  $\bar{\eta}(f_r) \leq 0.1$  Pa·s,  $\Delta f$  is slightly smaller and  $Q$  is slightly larger than the Newtonian values, and for  $\bar{\eta}(f_r) > 0.1$  Pa·s  $\Delta f$  is slightly larger, and  $Q$  is slightly smaller, than the Newtonian values. Fitting the Newtonian theory to the velocity resonance curves gave a fitted viscosity that agreed well with the spatiotemporally averaged viscosity obtained from the simulations for strong and weak shear thinning, however for intermediate values of shear thinning, the agreement was not as good.

Our comparison between the simulated behaviour of the wire vibrating in shear-thinning fluids to the theory of a wire vibrating in a Newtonian fluid has some implications for the physical vibrating-wire rheometer. Although we have shown that using a constant effective viscosity  $\bar{\eta}(f_r)$  in Eq. 2.1 gives a reasonable description of the wire's resonance behaviour in shear-thinning fluids, we found that fits of Eq. 2.1 to the resonant curves did not accurately reproduce the details of their full shape. The systematic deviations from the shape predicted by Eq. 2.1 observed here may be measurable using our vibrating-wire rheometer and if so, could be used as a qualitative indication or measure of shear-thinning. Our results showed that the shear rate and viscosity in the shear-thinning fluid depend on the velocity of the vibrating wire. Increasing the amplitude of the wire's velocity by increasing the amplitude of the driving force will change the degree of shear thinning in the fluid, and thus the effective viscosity seen by the wire. This could be investigated further by simulating the behaviour of the wire vibrating in a shear-thinning fluid as a function of the amplitude of the driving force. It could

also be studied experimentally with the vibrating-wire rheometer by measuring the viscosity of a shear-thinning fluid as a function of the driving current. This also suggests the possibility of observing the transition from the low-shear-rate constant-viscosity regime to the intermediate-shear-rate shear-thinning regime using our vibrating-wire rheometer.

Although in this chapter we have focused the vibration of a wire in Newtonian and shear-thinning fluids, the simulation we have described could easily be modified to study shear-thickening fluids. This would be an interesting topic for future work. Many complex fluids are not only shear-thinning, but also elastic. A more complete understanding of the behaviour of our vibrating wire rheometer in complex fluids could therefore be gleaned from simulations of a wire vibrating in viscoelastic fluids, however simulating viscoelastic fluids may require different software.

## 2.7 Conclusion

In this chapter we studied the driven transverse oscillations of a wire in Newtonian and shear-thinning fluids by means of two-dimensional numerical simulations using COMSOL. The results of simulations of a wire vibrating in a Newtonian fluid agree well with the theory developed by Retsina *et al.* [1, 2]. Our simulations of a wire vibrating in a shear-thinning fluid described by the Carreau model showed resonant behaviour similar to that in Newtonian fluids, but with resonant behaviour that depended on the shear-thinning parameters  $n$  and  $\lambda$ . We found that the shear rate and viscosity in the shear-thinning fluid varied significantly in both space and time over a period of the wire's oscillation. We defined an effective viscosity by averaging around the circumference of the wire and over one period of oscillation. A greater degree of shear-thinning, resulting from a lower value of  $n$  or a higher value of  $\lambda$ , led to a lower value of the effective viscosity. We found that for a simulation at fixed  $n$  and  $\lambda$ , the effective viscosity reached a minimum at the resonant frequency. We found that the resonant behaviour of the wire in shear-thinning fluids could be reasonably well described by the theory developed for a

wire vibrating in a Newtonian fluid if the viscosity was set equal to the effective viscosity at the resonant frequency.

## Bibliography

- [1] T. Retsina, S. M. Richardson, and W. A. Wakeham. The theory of a vibrating-rod densimeter. *Appl. Sci. Res.*, 43:127–158, 1986.
- [2] T. Retsina, S. M. Richardson, and W. A. Wakeham. The theory of a vibrating-rod viscometer. *Appl. Sci. Res.*, 43:325–346, 1987.
- [3] R. King. A review of vortex shedding research and its application. *Ocean Eng.*, 4:141–171, 1977.
- [4] T. Sarpkaya. Vortex-induced oscillations - a selective review. *J. App. Mech.*, 46:241–258, 1979.
- [5] D. J. Newman and G. E. Karniadakis. A direct numerical simulation study of flow past a freely vibrating cable. *J. Fluid Mech.*, 344:95–136, 1997.
- [6] O. M. Griffin, J. K. Vandiver, R. A. Skop, and D. J. Meggitt. The strumming vibrations of marine cables. *Ocean Sci. Eng.*, 7:461–498, 1982.
- [7] R. J. McNamara. Tuned mass dampers for buildings. *J. Struct. Div.*, 103:1785–1798, 1977.
- [8] S. Mittal and T. E. Tezduyar. A finite element study of incompressible flows past oscillating cylinders and aerofoils. *Int. J. Numer. Meth. Fluids*, 15:1073–1118, 1992.
- [9] S. Mittal and B. Kumar. Flow past a rotating cylinder. *J. Fluid Mech.*, 476:303–334, 2003.

- [10] R. Bourguet and D. L. Jacono. Flow-induced vibrations of a rotating cylinder. *J. Fluid Mech.*, 740:342–380, 2014.
- [11] H. M. Blackburn and R. D. Henderson. A study of two-dimensional flow past an oscillating cylinder. *J. Fluid Mech.*, 385:255–286, 1999.
- [12] R. Chilukuri. Incompressible laminar flow past a transversely vibrating cylinder. *J. Fluids Eng.*, 109:166–171, 1987.
- [13] A. A. Chhabra, R. P. Soares and J. M. Ferreira. Steady non-newtonian flow past a circular cylinder: a numerical study. *Acta Mech.*, 172:1–16, 2004.
- [14] S. A. Dhahir and K. Walters. On non-newtonian flow past a cylinder in a confined flow. *J. Rheol.*, 33:781–804, 1989.
- [15] M. A. Hulsen, R. Fattal, and R. Kupferman. Flow of viscoelastic fluids past a cylinder at high weissenberg number: Stabilized simulations using matrix logarithms. *J. Non-Newtonian Fluid Mech.*, 127:27–39, 2005.
- [16] P. Townsend. A numerical simulation of newtonian and visco-elastic flow past stationary and rotating cylinder. *J. Non-Newtonian Fluid Mech.*, 6:219–243, 1980.
- [17] A. Nejat, V. Abdollahi, and K. Vahidkhan. Lattice boltzmann simulation of non-newtonian flows past confined cylinders. *J. Non-Newtonian Fluid Mech.*, 166:689–697, 2011.
- [18] COMSOL, Inc. *COMSOL Multiphysics Reference Manual*, v. 5.1, 2015.
- [19] COMSOL, Inc. *COMSOL Structural Mechanics Module User’s Guide*, v. 5.1, 2015.
- [20] COMSOL, Inc. *COMSOL CFD Module User’s Guide*, v. 5.1, 2015.
- [21] G. G. Stokes. On the effect of the internal friction of fluids on the motion of pendulums. *Trans. Cambridge Philos. Soc.*, IX:8–106, 1851.



- [22] J. T. Tough, W. D. McCormick, and J. G. Dash. Vibrating wire viscometer. *Rev. Sci. Instrum.*, 35:1345, 1964.
- [23] F. A. Morrison. *Understanding Rheology*. Oxford University Press, 2001.
- [24] J. Chung and G. M. Hulbert. A Time Integration Algorithm for Structural Dynamics With Improved Numerical Dissipation: The Generalized-alpha Method. *J. Appl. Mech.*, 60:371–375, 1993.
- [25] K. E. Jansen, C. H. Whiting, and G. M. Hulbert. A generalized-alpha method for integrating the filtered navier-stokes equations with a stabilized finite element method. *Comput. Meth. Appl. Mech. Eng.*, 190:305–319, 2000.

# Chapter 3

## Vibrating-wire Rheometry

### 3.1 Introduction

The viscoelastic properties of complex fluids are commonly measured using rotational shear rheometers. These instruments are typically limited to frequencies  $\lesssim 100$  Hz due to the inertia of the rheometer tool [1, 2]. Knowledge of the rheological properties of complex fluids at higher frequencies is important for understanding their dynamical properties, microstructure, and interactions between the components of the fluid. For example, the high-frequency behaviour of the viscoelastic moduli contains information about inter-particle forces in a concentrated colloidal suspension [3]. Very fast relaxation processes in polymer solutions can only be measured using high-frequency methods [4]. In some cases, the high-frequency properties can be inferred by employing time-temperature superposition or time-concentration superposition [5], but there are many fluids for which these techniques cannot be applied due to effects such as evaporation or freezing of the solvent or temperature-induced phase transitions. There is thus a need for new experimental methods that will enable the exploration of the high-frequency dynamics of complex fluids.

Devices based on the vibrations of a wire in a fluid have frequently been used to measure viscosity and density. A brief review is provided in Ref. [6]. Viscosity damps the vibrations. It

can be determined either in the time domain, by measurements of the damping time, or in the frequency domain, through measurements of the wire's resonance curve [6]. In 1850, Stokes analysed the problem of an infinite cylinder oscillating perpendicular to its axis in an infinite fluid [7]. In 1964, Tough *et al.* [8] constructed a vibrating-wire viscometer which they used to measure the viscosity of liquid helium. Retsina *et al.* [9] solved the Navier-Stokes equations for a finite cylindrical rod vibrating in an infinite Newtonian fluid. They developed a set of working equations that relate the motion of the wire to the fluid properties and discussed the effects of the physical dimensions of the device on the accuracy of the viscosity measurements. Kandil and Marsh [10] constructed a vibrating-wire device to measure the viscosity of a range of Newtonian fluids. Forced oscillations were produced by passing an alternating current through a wire under tension in a constant magnetic field. They expanded upon the theory of Retsina *et al.* [9] to derive an expression for the voltage induced in the wire due to its motion in the magnetic field and its dependence on fluid properties. Many other devices of this type have been reported, for use in applications ranging from the petroleum industry to bedside measurements of blood viscosity and under a broad range of environmental conditions [6].

Vibrating objects have been used for rheometrical measurements in non-Newtonian fluids in the past. A patent for a vibrating-wire rheometer was issued in 1996 [11], but we are unaware of any published description of this instrument, nor of any results obtained using it. Fritz *et al.* [1] explored the high frequency dynamics of several complex fluids using torsional resonators. They used cylindrical and double-dumbbell-shaped torsional resonators to perform measurements at discrete frequencies on the order of 10 kHz. Using a simple model of mechanical resonators and comparing measurements in the fluid to reference measurements in air, the properties of several complex fluids were determined. Although Fritz *et al.* successfully measured viscous and elastic moduli using this method, it requires calibration of the device, operates at a single discrete frequency, and the geometry is too complex for a complete theoretical description. Wang *et al.* recently introduced a method for performing measurements over a range of frequencies around the resonance peak of a torsional oscillator [12] and applied it to

determine the viscoelastic moduli of polymer solutions at frequencies from 0 to 400 Hz [13].

Measurements at higher frequencies require smaller devices with higher resonant frequencies. Lemaire *et al.* have investigated the use of vibrating microstructures to measure density and complex viscosity [14]. They fabricated two devices, a microcantilever and a U-shaped vibrating wire, which operated at frequencies in the range from  $10^3$  to  $10^5$  Hz. By estimating the hydrodynamic force on the structures and taking the fluid viscosity to be complex (see Eq. 3.8), they were able to measure the viscous modulus  $G''$  to within 20% of the accepted value. Using nanofabrication techniques, Riesch *et al.* fabricated a viscometer consisting of a suspended plate  $100 \times 100 \mu\text{m}$  in size with a resonance frequency of 16 kHz [15]. While this device was successfully used to measure viscosity, its use was not extended to complex fluids.

In this chapter we describe a novel vibrating-wire rheometer for the measurement of viscoelastic moduli in low- to moderate-viscosity fluids at frequencies around 1 kHz. The construction of the device, experimental setup, and data analysis method are discussed. Measurements in Newtonian fluids and a homogeneous viscoelastic polymer solution are presented to demonstrate the efficacy and accuracy of the device. We also show how the device can be used to probe the time-dependent changes in microstructure of an aging suspension of Laponite clay [16, 17].

## 3.2 Theory

### 3.2.1 Newtonian fluids

Theoretical descriptions of the motion of a wire vibrating in a Newtonian fluid have been presented in [7, 8, 9, 10]. This earlier work was extended by Kandil [18] to consider the voltage induced in a current-carrying wire vibrating in a viscous Newtonian fluid in a magnetic field as a function of fluid parameters and vibration frequency. The amplitude of the wire's oscillation, and therefore the induced voltage, is a maximum at a resonance frequency. The induced voltage

is given by [18]

$$V = a + bf + ci + dfi + \frac{\Lambda fi}{f_0^2 - (1 + \beta)f^2 + (\beta' + 2\Delta_0)f^2i}, \quad (3.1)$$

where the first four terms are due to the electrical impedance of the stationary wire and any background voltage;  $a$ ,  $b$ ,  $c$ , and  $d$  are adjustable parameters determined by curve fitting. The last term is the motional electromotive force and is a function of the fluid properties.  $i$  is the imaginary number  $\sqrt{-1}$ ,  $\Lambda$  is the voltage amplitude,  $f_0$  is the resonance frequency of the vibrating wire in vacuum,  $\Delta_0$  is the self-damping of the wire,  $\beta$  is the added mass arising from fluid displacement, and  $\beta'$  is the viscous damping term.

The density and viscosity of the fluid are contained within  $\beta$  and  $\beta'$ . Retsina *et al.* [9] studied the fluid mechanics of a vibrating wire of density  $\rho_w$  in a fluid of density  $\rho$  and determined  $\beta$  and  $\beta'$  to be given by

$$\beta = k \frac{\rho}{\rho_w}, \quad (3.2)$$

and

$$\beta' = k' \frac{\rho}{\rho_w}, \quad (3.3)$$

respectively, where  $k$  and  $k'$  are

$$k = -1 + 2\Im(\mathbf{A}), \quad (3.4)$$

and

$$k' = 2\Re(\mathbf{A}). \quad (3.5)$$

Here  $\Im$  and  $\Re$  represent the imaginary and real components, respectively.  $\mathbf{A}$  is a complex quantity given by

$$\mathbf{A} = \left( 1 + \frac{2K_1(\sqrt{\Omega}i)}{\sqrt{\Omega}iK_0(\sqrt{\Omega}i)} \right) i, \quad (3.6)$$

where

$$\Omega = \frac{2\pi f \rho R^2}{\eta}. \quad (3.7)$$

$K_0$  and  $K_1$  are the modified Bessel functions of zeroth and first order, and  $\Omega$  is a dimensionless quantity related to the Reynolds number which characterizes the flow around a cylindrical wire of radius  $R$  in a fluid with viscosity  $\eta$ .  $\eta$  is determined by fitting the experimentally-measured voltage across the vibrating wire to Eq. 3.1. For Ethanol at  $T = 20$  °C, with  $f = 1000$  Hz,  $\Omega = 23$ . The Reynolds number based on the displacement of the wire is given by  $Re = \epsilon\Omega$  where  $\epsilon = y/R$  is the dimensionless amplitude of the wire's oscillations [9]. The amplitude of the wire's oscillations is  $\lesssim 1$   $\mu\text{m}$ , yielding  $Re \lesssim 2.3$  for Ethanol. For the more viscous Newtonian fluids and the viscoelastic fluids studied in this chapter,  $Re \ll 1$ .

### 3.2.2 Viscoelastic fluids

To extend the above theory to viscoelastic fluids, we replace the Newtonian viscosity  $\eta$  in Eq. 3.7 by a complex viscosity  $\eta^*$  [5]:

$$\eta \rightarrow \eta^* = \eta' - i\eta'' = \frac{G' + iG''}{i\omega}, \quad (3.8)$$

where  $G'$  and  $G''$  are the elastic and viscous moduli respectively and  $\omega = 2\pi f$  is the angular frequency. This substitution is exact in the limit of linear response [5]. In general  $G'$  and  $G''$  will be functions of frequency, although we will assume them to be constant over the limited frequency range of our experiments, as discussed below. In our experiments, described below, we measure the induced voltage  $V(f)$  and determine  $G'$  and  $G''$  by fitting our data to Eq. 3.1 with this substitution.

## 3.3 Experiment

### 3.3.1 Vibrating-wire rheometer

We constructed several vibrating-wire devices designed to have different resonant frequencies; they differ only in the active length of the wire. One is shown in the left panel of Fig. 3.1

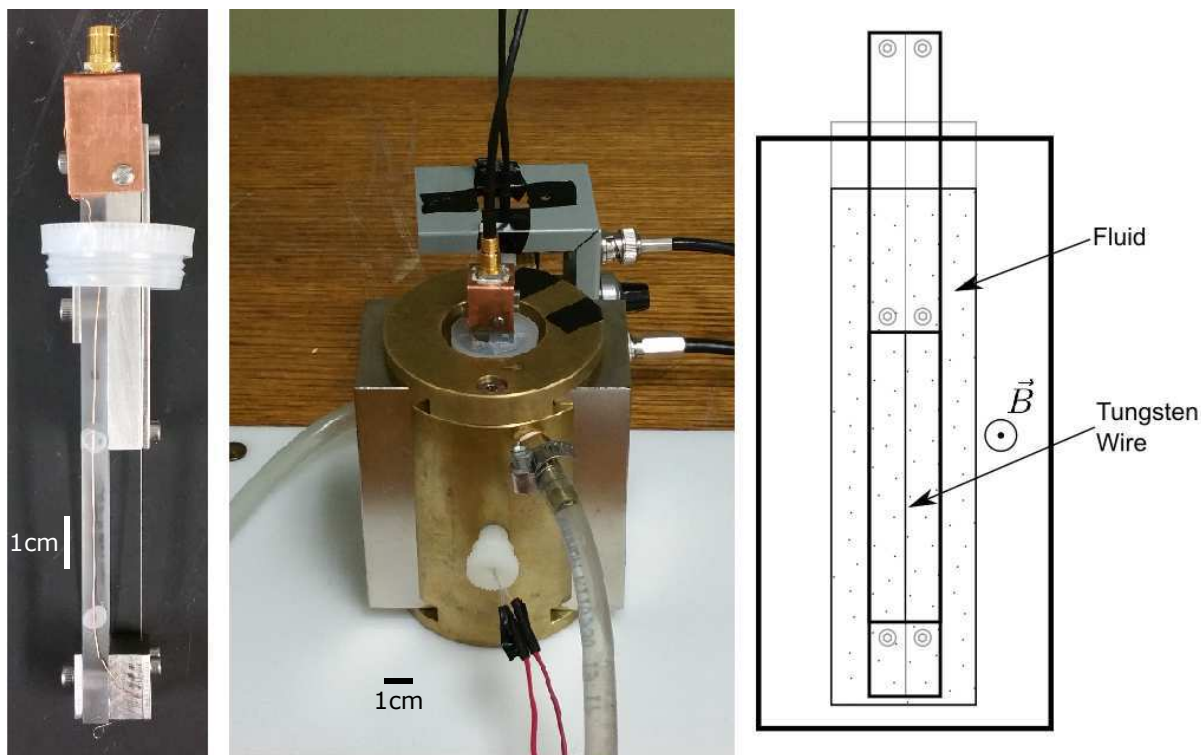


Figure 3.1: Photographs of the vibrating-wire rheometer (left) and the temperature-controlled housing and magnets (center), and a schematic diagram of the instrument as seen looking through the face of the magnet (right). Colour online.

and drawn schematically in the right panel. The operation of the device is similar to that described by Kandil [10, 18]. A tungsten wire is held under tension by two stainless steel clamps. The steel clamps are mounted on a borosilicate glass backbone. This wire holder is placed inside a vial containing the sample fluid, and the vial is immersed in a temperature controlled housing as shown in the center panel of Fig. 3.1.

To ensure wall effects are negligible, the ratio of the radius of the fluid container  $R_c$  to the radius of the wire  $R$  must be large. Retsina *et al.* determined that a ratio  $R_c/R = 33$  contributes an error of less than  $\pm 0.05\%$  to the measured viscosity [9]. In our case the distance to the glass backbone yields a ratio of 67, while the fluid vial yields a ratio greater than this.

Two permanent magnets are mounted on the sides of the housing to produce a magnetic field. An alternating current of frequency  $f$  and amplitude  $\sim 1$  mA is passed through the wire, and the resulting Lorentz force causes the wire to vibrate at the driving frequency.

Tungsten wire of diameter 0.15 mm (Goodfellow, Huntingdon, UK) was chosen for the vibrating wire because of its relatively high Young's modulus,  $E \approx 411$  GPa, and density,  $\rho_w \approx 19300$  kg m<sup>-3</sup>. The high Young's modulus gives a stable resonance and the high density relative to the fluids studied provides more sensitivity through the density ratios in Eqs. 3.2 and 3.3. Borosilicate glass (Specialty Glass Products, Willow Grove, PA) was used as the backbone of the wire holder because its thermal expansivity is closely matched to that of tungsten, ensuring that the tension in the wire remains constant as temperature is varied. The magnetic field is produced by two NdFeB, Grade N52 magnets with dimensions 4"  $\times$  2"  $\times$  1" (K & J Magnetics, Pipersville, PA) which are mounted to the sides of the brass holder as illustrated in Fig 3.1 (center). Each magnet has a surface field strength of 0.42 T, and the two together produce a homogeneous magnetic field at the location of the vibrating wire of roughly 0.8 T. The exact field strength is not important, but should be high enough that the current through the wire can generate a Lorentz force large enough to drive the oscillations while limiting Joule heating. In our case, the amplitude of the alternating current  $I \approx 1$  mA. The temperature of the experimental fluid is controlled by circulating fluid from a temperature controlled bath through the internal cavity of the brass housing shown in Fig. 3.1(center). A calibrated thermistor placed in the circulating fluid is used to measure its temperature and to ensure that steady-state has been reached after the bath temperature is changed.

The wire was installed in the device with a controlled tension by clamping the top of the vibrating section of the wire and suspending a mass from it. After waiting approximately 24 hours for any torsional oscillations to damp out, the bottom of the wire was then carefully clamped in place. The resonant frequency of the vibrating wire depends on the tension as [19]

$$f_0 \approx \frac{1}{2L} \sqrt{\frac{mg}{\rho_w \pi R^2}}, \quad (3.9)$$

where  $m$  is the suspended mass,  $mg$  is the tension force, and  $L$  is the length of the wire. We used wires of length  $L = 4, 5,$  and  $6$  cm, and  $m = 600$  g, which resulted in resonant frequencies



$f_0 \approx 1600, 1300,$  and  $1100$  Hz, respectively. With this value of  $m$ , the stress applied to the wire was in the range of 20–50% of its tensile strength, which is approximately 720 MPa [10]. From the equations of motion for the wire found in Refs. [9, 10, 18], we estimate the amplitude of our wire’s oscillation to be  $\lesssim 1 \mu\text{m}$ . This is an order of magnitude smaller than the wire’s diameter, suggesting that the assumption of linear response implicit in our use of the complex viscosity is justified.

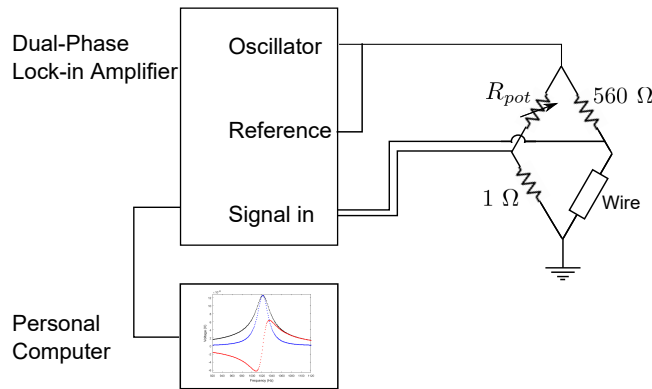


Figure 3.2: A schematic diagram of the experimental setup.

Fig. 3.2 shows the circuit used to drive the oscillations and measure the voltage induced across the wire as it moves in the magnetic field. The vibrating wire, which has a resistance  $\lesssim 1 \Omega$ , is one arm of a Wheatstone bridge. A dual-phase lock-in amplifier (Model 7230, Signal Recovery, Oak Ridge, TN) is used to drive the circuit and to detect the error signal across the bridge. At the beginning of an experiment, a 1 k $\Omega$  potentiometer in another arm of the bridge is adjusted to null the voltage across the bridge far from resonance. The lock-in amplifier detects the in- and out-of-phase components of the signal as the frequency is swept through the wire’s resonance. Data are recorded by a personal computer for later analysis.

### 3.3.2 Rheometric Measurements

Conventional shear rheometric measurements were done using an Anton Paar MCR 302 shear rheometer. The linear viscoelastic properties of the HEC solution were measured using a parallel-plate geometry with a gap of 1 mm. A strain amplitude of 1% was used to ensure

measurements were performed in the linear viscoelastic regime. For the Laponite suspension, a Couette geometry was used due to its low initial viscosity. The temperature of the samples was controlled using a Peltier system with an environmental hood that enclosed the rheometer tool.

Microrheological measurements were done using dynamic light scattering [20, 21]. We used an ALV/CGS-3 Compact Goniometer (ALV, Langen, Germany). Measurements were performed at a single scattering angle, chosen to maximize the strength of the signal due to light scattered by small tracer particles suspended in the fluid of interest. A digital correlator computes the autocorrelation function of the scattered light intensity as a function of delay time, from which the mean-squared displacement of the tracer particles can be determined. The viscoelastic moduli can then be calculated using the generalized Stokes-Einstein relation [22, 23].

### 3.3.3 Sample Preparation

Reagent-grade ethanol and a silicone oil with a viscosity of 20 mPa·s at 25 °C (Clearco Products, Bensalem, PA) were used to verify the device's operation in Newtonian fluids. As sample viscoelastic fluids, we used aqueous solutions of 2-hydroxyethyl cellulose (HEC). HEC with an average molecular weight of  $M_v \sim 1,300,000$  was purchased from Sigma Aldrich Canada. An HEC solution with a similar concentration as studied in this chapter has been characterized by Yiu *et al.* in Ref. [24]. Milli-Q deionised and distilled water was filtered through 0.2  $\mu\text{m}$  filters, then heated to 90 °C on a hotplate. HEC powder was then added slowly to the water and mixed in using a magnetic stirrer. Sufficient time was allowed for the polymer to dissolve completely. The solution was then covered and allowed to sit overnight.

We also used our vibrating-wire device to study the gel transition in a 1 wt% aqueous suspension of Laponite RD (Southern Clay Products, Gonzales, TX). Laponite is a synthetic clay consisting of disk-shaped particles approximately 30 nm in diameter and 1 nm thick. Laponite and  $10^{-3}$  mol/l NaCl were added to room temperature Milli-Q water that had been

passed through a  $0.2\ \mu\text{m}$  filter. The addition of salt controls the ionic strength of the suspension and screens long-range electrostatic interactions between the Laponite particles [16]. This results in attractive van der Waals forces dominating the interaction between particles, leading to the formation of a gel structure [25]. The solution was thoroughly mixed overnight using a propeller-blade mixer. NaOH was then added to raise the  $p\text{H}$  value to 10 to inhibit the sedimentation of the clay particles [26]. For light scattering measurements, polystyrene latex spheres with a diameter of 220 nm (Thermo Scientific, Freemont, CA) were added to the Laponite suspension at a volume fraction of  $1 \times 10^{-5}$ . Immediately after mixing, samples of the suspension were transferred into the Couette cell of the shear rheometer, the sample vial of the vibrating-wire rheometer, and a test tube for use in DLS measurements.

## 3.4 Results

### 3.4.1 Newtonian fluids

We validated our vibrating-wire device by using it to determine the viscosities of ethanol and a silicone oil at temperatures  $T$  from 5 to 60 °C. A representative set of raw data is plotted in Fig. 3.3, which shows the in- and out-of-phase components of the voltage measured across the bridge circuit for a vibrating wire in ethanol at  $T = 9.7\ \text{°C}$ . Independent fits of Eq. 3.1 to the two components of the voltage are shown as curves through the data in Fig. 3.3. There are very slight systematic deviations from the fits in some regions of the resonance curve, but the overall agreement between the theoretical expression and the data is excellent. In the case plotted in Fig. 3.3, the expected viscosity is  $\eta = 1.40\ \text{mPa}\cdot\text{s}$  [27]. The viscosity determined from the fit to the in-phase component was  $\eta = 1.36\ \text{mPa}\cdot\text{s}$ , while the out-of-phase component yielded  $\eta = 1.39\ \text{mPa}\cdot\text{s}$ . In both cases, the viscosities determined from our vibrating-wire device are within 3% of the expected value. While in this example the out-of-phase component agrees more closely with the expected value, neither component gave significantly better results than the other on average. Results presented below are determined from fits to the out-of-phase

component of the induced voltage.

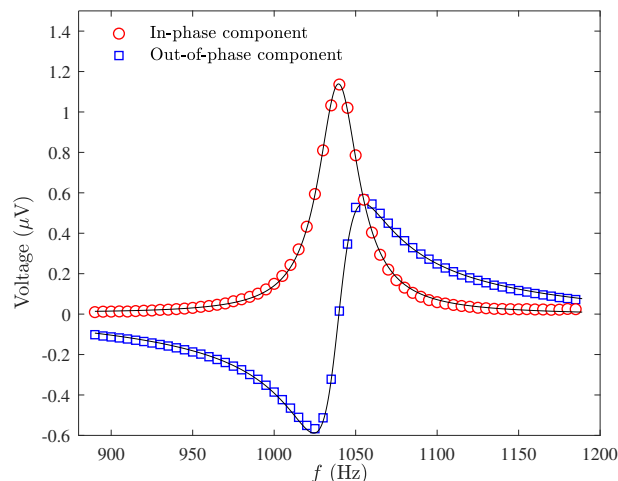


Figure 3.3: Voltage induced in the vibrating wire as a function of frequency for ethanol at 9.7 °C. The curves are independent fits the real and imaginary parts of Eq. 3.1 to each component.

Figure 3.4 compares the viscosity measured with the vibrating-wire device with the expected viscosity for ethanol and silicone oil over a range of temperatures. Ethanol data are compared with values tabulated in Ref. [27], while the viscosity of silicone oil was measured in our laboratory with an Anton Paar MCR 302 shear rheometer. The inset to Fig. 3.4 shows the deviation between the measured and expected values. Over the range of viscosities and temperatures studied, the viscosities determined with our vibrating-wire device were consistently within  $\pm 3\%$  of the accepted values.

### 3.4.2 Viscoelastic polymer solutions

We demonstrated the ability of our device to determine the viscous and elastic moduli of non-Newtonian fluids using a variety of aqueous polymer solutions. Here we present results obtained using a 3.5 wt% aqueous solution of HEC, although similar results were obtained with other concentrations of HEC and with other polymers.

Fig. 3.5 shows the voltage induced in the vibrating-wire rheometer in the 3.5 wt% HEC solution at  $T = 20$  °C. The curves are fits to the data of Eq. 3.1 with a complex viscosity, as in

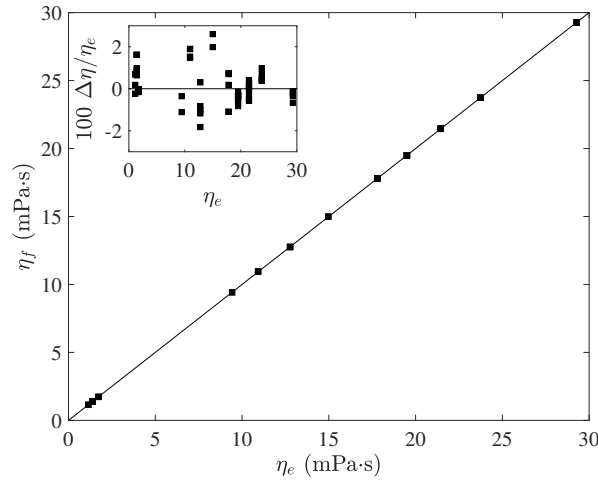


Figure 3.4: The viscosity determined from fits to vibrating-wire data as in Fig. 3.3,  $\eta_f$ , plotted against expected viscosity,  $\eta_e$ . The solid line is  $\eta_f = \eta_e$ . The fluids were ethanol and silicone oil at temperatures ranging from 5 to 60 °C. Uncertainties in the measured viscosities are smaller than the size of the symbol. Inset: Difference between the measured and expected values.

Eq. 3.8. Only every 10th data point is displayed for clarity and to make the fit lines visible. The theoretical expression provides an excellent description of the data. The viscoelastic moduli measured using the vibrating-wire rheometer are compared to data obtained with the Anton Paar rheometer in Fig. 3.6. The shear rheometer was used to measure  $G'(f)$  and  $G''(f)$  for  $0.15 \leq f \leq 32$  Hz at a strain amplitude of 1% and temperatures ranging from 1 to 20 °C. Using time-temperature superposition, master curves for the viscous and elastic moduli were generated at a reference temperature of 20 °C. The longest characteristic relaxation time  $\lambda$  for the 3.5 wt.% HEC solution can be approximated by the frequency where the moduli cross over by  $\lambda = 1/2\pi f_c$  [28]. The crossover frequency is  $f_c = 1.2$  Hz, yielding  $\lambda = 0.13$  s. Measurements with vibrating-wire rheometers having wire lengths  $L = 5$  and 6 cm were also performed at 20 °C. Although the two vibrating-wire devices had different vacuum resonance frequencies (1300 and 1100 Hz respectively), the high viscosity of the HEC solution broadened the resonance curves to the extent that the frequency ranges probed by the two wires overlapped significantly. The frequency of the vibrating-wire rheometers is an order of magnitude higher than that obtainable with the shear rheometer. Comparing the two sets of data indicates that the moduli measured by the vibrating-wire device are consistent with those measured at lower

frequencies by the shear rheometer.

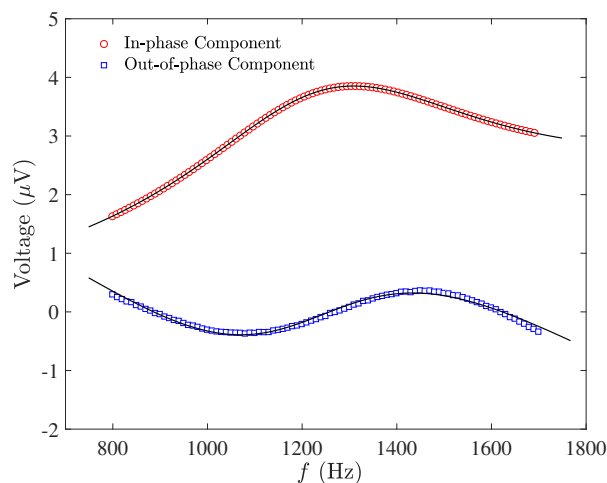


Figure 3.5: In-phase and out-of-phase components of the measured voltage for a 3.5 wt% aqueous solution of HEC. The black lines are independent fits of the real and imaginary parts of Eq. 3.1 to the components with the complex viscosity substitution, Eq. 3.8. Only every 10th data point is plotted for clarity.

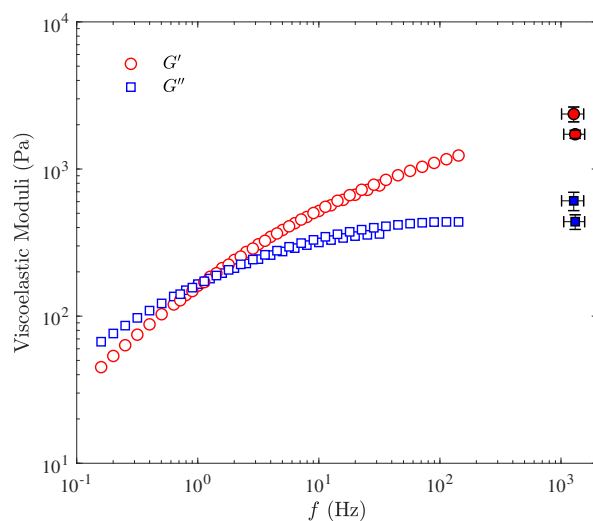


Figure 3.6: Viscoelastic moduli for a 3.5 wt% solution of HEC in water. The data spanning 1–100 Hz (open symbols) were obtained from a shear rheometer using time-temperature superposition. The data at approximately 1000 Hz (solid symbols) were obtained with vibrating-wire rheometers with lengths  $L = 5$  and 6 cm, as described in the text.

Fitting the complex-viscosity version of Eq. 3.1 to the data is difficult due to the fact that the expression contains eight fitting parameters. We assume that  $G'$  and  $G''$  are constant over

the limited range of frequency spanned by the resonance curve of our device. Allowing the moduli to vary with, for example, a power-law dependence on frequency did not improve the quality of the fits, and, in fact, had the opposite effect. We found the fit parameters to vary by  $\pm 15\%$ , depending on the range of frequencies included in the fit.

We incorporated this range-dependence into the reported uncertainty in the moduli as follows. Starting with a small frequency range centred on the resonance frequency, we iterated the fitting routine over increasing ranges of frequency, using the parameter values determined from the previous iteration as the starting point for the next. The moduli plotted in Fig. 3.6 are the means of the several values obtained by this process, and the error bars indicate the standard deviation. The error bars in frequency indicate the full width at half maximum of the resonant peak (the in-phase component of the measured voltage) with the background removed.

### 3.4.3 Aging and gelation of a clay suspension

The above data demonstrate that our vibrating-wire rheometer gives results in good agreement with conventional rheometric measurements on a homogeneous polymer solution. Since the amplitude of the wire's oscillation is  $\lesssim 10 \mu\text{m}$ , however, we would expect it to give results that differ from bulk measurements in complex fluids that are heterogeneous on that length scale. In other words, our device probes the microrheology of such materials [20] in the sense that it measures the local properties of the fluid at the  $10 \mu\text{m}$  scale rather than the bulk properties.

To demonstrate this, we studied the viscoelastic moduli of a suspension of 1 wt% Laponite clay in water as a function of aging time  $\tau$  using the vibrating-wire rheometer, and compared our results with data obtained using conventional shear rheometry and dynamic light scattering microrheology. Depending on ion concentration [25], a Laponite suspension can undergo a transition for a liquid to a gel phase as it ages. Previous work has shown that the viscoelastic properties of the gel-forming Laponite suspension depend on the length scale being probed [16, 17]. These groups used particle-tracking microrheological techniques to measure the micron-

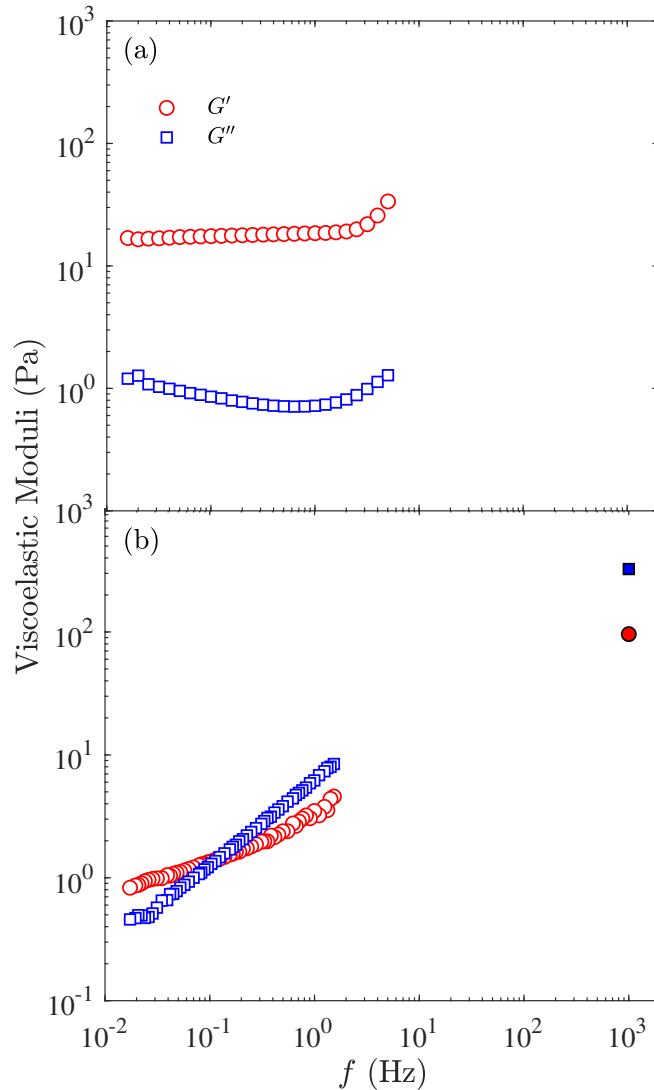


Figure 3.7: Viscoelastic moduli of a 1 wt% Laponite suspension vs. frequency after approximately 4 h of aging. Data in (a) were measured using a shear rheometer. Data in (b) were determined from dynamic light scattering (open symbols) and with the vibrating-wire rheometer (solid symbols).

scale viscous and elastic moduli of the Laponite. Immediately after mixing, they found the microrheological response of the suspension to be primarily viscous, with  $G'' > G'$ . Over time, the suspension undergoes a gel transition, evolving into a viscoplastic material with a bulk yield stress and  $G' > G''$ . The gel transition, at which  $G' = G''$ , occurred much earlier in bulk-scale measurements made with a shear rheometer than in the microrheological measurements [16, 17].



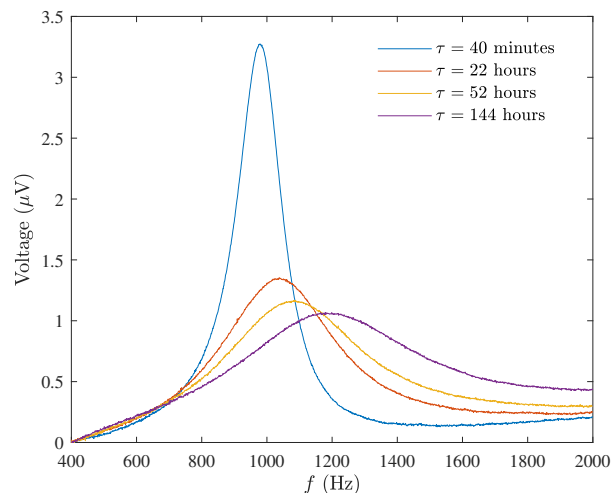


Figure 3.8: The in-phase component of the voltage measured with the vibrating-wire rheometer for an aging Laponite clay suspension. From largest to smallest amplitude, the curves correspond to aging times of 40 min, 22 h, 52 h, and 144 h.

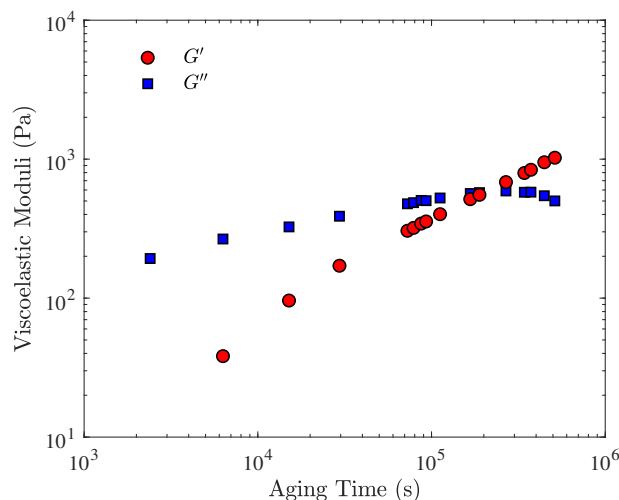


Figure 3.9: Viscoelastic moduli of the 1% Laponite suspension measured with the vibrating-wire rheometer plotted as a function of aging time. Error bars are not shown for clarity, but are similar to those plotted in Fig. 3.6.

At  $\tau = 0$ , our Laponite suspension was very fluid. Figure 3.7 shows data taken using all three experimental methods when the suspension had aged for 4 h. Data from the shear rheometer are shown in Fig. 3.7(a). These data show that, on the mm length scale probed by the rheometer, the suspension had already gelled by this time:  $G'$  is an order of magnitude larger than  $G''$ , and both are approximately independent of frequency. Very different behavior

is seen in the DLS data, shown in Fig. 3.7(b). These data, which probe the properties of the material on the scale of the 200 nm tracer particles, show viscoelastic behavior. At low frequencies the fluid is primarily elastic, with  $G' > G''$ . There is a crossover frequency around  $f = 0.1$  Hz, above which  $G'' > G'$ . The solid symbols in Fig. 3.7(b) are the values of  $G'$  and  $G''$  measured with the vibrating-wire rheometer at  $f = 1000$  Hz. The vibrating-wire results also show  $G'' > G'$  and are consistent with the microrheological measurements obtained by DLS.

Fig. 3.8 shows the effect of aging of the Laponite suspension on the resonance curve of the vibrating wire. The in-phase component of the induced voltage is shown as a function of frequency for aging times ranging from 40 min to 6 days. 20 min after mixing the viscosity of the suspension is approximately 30 times that of water. As the material ages over the course of a week, both the viscosity and elasticity increase significantly. The increase in viscosity broadens the resonance curve, while the increase in elasticity that accompanies the gel formation shifts the resonance to higher frequency.

Fig. 3.9 shows the viscoelastic moduli of Laponite determined with the vibrating-wire rheometer plotted as a function of aging time  $\tau$ . At early times, the solution exhibits viscous, fluid-like behaviour, with  $G'' > G'$ . At  $\tau \approx 2 \times 10^5$  s, however, the elastic modulus becomes greater than the viscous modulus. This crossover point corresponds to the gel transition as measured on the scale of the amplitude of the vibrating wire. For comparison, the data from the shear rheometer plotted in Fig. 3.7(a) indicate that bulk-scale gelation occurred before  $\tau = 1.4 \times 10^4$  s. These results are in agreement with previous microrheological measurements of Laponite suspensions [16, 17], and confirm that our vibrating-wire device can be used as a microrheological probe.

### 3.5 Discussion and Conclusion

We have described the design and operation of a novel vibrating-wire rheometer, and demonstrated its use on homogenous polymer solutions and a viscoplastic clay suspension. The voltage induced across the wire when it vibrates in a magnetic field is measured as a function of frequency using a bridge circuit and two-phase lock-in detection. The viscoelastic moduli of the fluid of interest are determined by fitting a theoretical expression to the data. As a simple viscometer, our device functions very well, giving viscosities within  $\pm 3\%$  of the expected value. The viscous and elastic moduli of a homogeneous aqueous polymer solution are consistent with those measured at lower frequencies by a shear rheometer. In an aging Laponite clay suspension, which is heterogeneous on the micron scale, our device was used to monitor the variation in time of the viscous and elastic moduli as the suspension gelled, and to determine the micron-scale gel time. Our data were consistent with previous results [16, 17].

Our vibrating-wire device has some advantages over conventional shear rheometers. The operating frequency is higher than those easily obtained with a rotational rheometer, and can be tuned by varying the length, diameter, and tension of the wire. In addition, our device can easily measure very low viscosities, a task that is difficult with rotational rheometers. The present instrument allows operation over a rather limited range of temperatures and with any non-corrosive fluid with low to moderate viscosity. The first of these limitations could be overcome by modifying the design of the device to dynamically control the tension in the wire to allow operation at different temperatures, and the second by careful choice of construction materials. The behaviour of our device as a function of temperature is investigated in App. A. This work demonstrates the potential of the vibrating-wire rheometer for characterizing complex fluids and for microrheological studies.

## Bibliography

- [1] G. Fritz, W. Pechhold, N. Willenbacher, and N. J. Wagner. Characterizing complex fluids with high frequency rheology using torsional resonators at multiple frequencies. *J. Rheol.*, 47:15, 2003.
- [2] J. L. Schrag. Deviation of velocity gradient profiles from the “gap loading” and “surface loading” limits in dynamic simple shear experiments. *Trans. Soc. Rheol.*, 21:399–413, 1977.
- [3] R. Buscall, J. W. Goodwin, M. W. Hawkins, and R. H. Ottewill. Viscoelastic properties of concentrated lattices. 2. theoretical-analysis. *J. Chem. Soc., Faraday Trans. 1*, 78:2889–2899, 1982.
- [4] P. E. Rouse. A theory of the linear viscoelastic properties of dilute solutions of coiling polymers. II, A first-order mechanical thermodynamic property. *J. Chem. Phys.*, 108:4628, 1998.
- [5] J. D. Ferry. *Viscoelastic Properties of Polymers*. Wiley, New York, 1961.
- [6] R. A. Secco, M. Kostic, and J. R. de Bruyn. Fluid viscosity measurement. In J. G. Webster and H. Erin, editors, *Measurement, Instrumentation, and Sensors Handbook, 2nd Edition*. CRC Press, Boca Raton, 2014.
- [7] G. G. Stokes. On the effect of the internal friction of fluids on the motion of pendulums. *Trans. Cambr. Philosoph. Soc.*, IX:8–106, 1850.
- [8] J. T. Tough, W. D. McCormic, and J. G. Dash. Vibrating wire viscometer. *Rev. Sci. Instrum.*, 35:1345–1349, 1964.
- [9] T. Retsina, S. M. Richardson, and W. A. Wakeham. The theory of a vibrating-rod viscometer. *Appl. Sci. Res.*, 43:325–346, 1987.

- [10] M. E. Kandil and K. N. Marsh. Vibrating wire viscometer with wire diameters of (0.05 and 0.15) mm: Results for methylbenzene and two fluids with nominal viscosities at  $T = 298$  K and  $p = 0.01$  MPa of (14 and 232) mPas at temperatures between (298 and 373) K and pressures below 40 MPa. *J. Chem. Eng. Data*, 50:647–655, 2005.
- [11] Bohlin; L. US Patent 5,565,620, 1996.
- [12] Y. Z. Wang, X. M. Xiong, and J. X. Zhang. New method of forced-resonance measurement for the concentrated and large-viscous liquid in the low frequency range by torsion resonator. *J. Rheol.*, 52:999–1011, 2008.
- [13] Y. Z. Wang, G. H. Wang, X. M. Xiong, B. Wang, L. M. Zhang, and J. X. Zhang. Viscoelastic measurement of complex fluids using forced oscillating torsion resonator with continuously varying frequency capability. *Rheol. Acta*, 49:1117–1126, 2010.
- [14] E. Lemair, M. Heinisch, B. Caillard, B. Jakoby, and I. Dufour. Fluid characterization using a vibrating microstructure the future of (micro)rheology? In *Proceedings of the 13th Mechatronics Forum International Conference, Linz, Austria*, 2012.
- [15] C. Riesch, E. K. Reichel, A. Jachimowicz, J. Schalko, P. Hudek, B. Jakoby, and F. Keplinger. A suspended plate viscosity sensor featuring in-plane vibration and piezoresistive readout. *J. Micromech. Microeng.*, 19:075010, 2009.
- [16] F. K. Oppong, P. Coussot, and J. R. de Bruyn. Gelation on the microscopic scale. *Phys. Rev. E*, 78:021405, 2008.
- [17] J. P. Rich, G. H. McKinley, and P. S. Doyle. Size dependence of microprobe dynamics during gelation of a discotic colloidal clay. *J. Rheol.*, 55:273–299, 2011.
- [18] M. E. Kandil. *A vibrating wire viscometer and a microwave cavity resonator for the measurement of viscosity, dew points, density, and liquid volume fraction at high temperature and pressure*. PhD thesis, University of Canterbury, Christchurch, New Zealand, 2005.

- [19] A. Bokaian. Natural frequencies of beams under tensile axial loads. *J. Sound Vib.*, 142:481–498, 1990.
- [20] T. A. Waigh. Microrheology of complex fluids. *Rep. Prog. Phys.*, 68:685–742, 2005.
- [21] B. R. Dasgupta, S.-Y. Tee, J. C. Crocker, B. J. Frisken, and D. A. Weitz. Microrheology of polyethylene oxide using diffusing wave spectroscopy and single scattering. *Phys. Rev. E*, 65:051505, 2002.
- [22] T. G. Mason. Estimating the viscoelastic moduli of complex fluids using the generalized stokes-einstein equation. *Rheol. Acta*, 39:371–378, 2000.
- [23] T. M. Squires and T. G. Mason. Fluid mechanics of microrheology. *Annu. Rev. Fluid Mech.*, 42:413–438, 2010.
- [24] Y. Liu, C. C. Hopkins, W. B. Handler, B. A. Chronik, and J. R. de Bruyn. Rheology and heat transport properties of a hydroxyethyl cellulose-based MRI tissue phantom. *Biomed. Phys. Eng. Express*, 3:045008, 2017.
- [25] H. Tanaka, J. Meunier, and D. Bonn. Nonergodic states of charged colloidal suspensions: Repulsive and attractive glasses and gels. *Phys. Rev. E*, 69:031404, 2004.
- [26] D. W. Thompson and J. T. Butterworth. The nature of laponite and its aqueous dispersions. *J. Colloid Interf. Sci.*, 151:236–243, 1992.
- [27] Chemical Engineering and Materials Research Information Center, <http://www.cheric.org>. *Pure Component Properties (Online database)*. Accessed 10 March 2016.
- [28] Christopher W. Macosko. *Rheology: Principles, Measurements, and Applications*. Wiley-VCH, 1994.

# Chapter 4

## Gelation Dynamics of Aqueous Solutions of Pluronic F127

### 4.1 Introduction

Pluronic F-127, referred to below simply as Pluronic, is a commercially available linear ABA triblock copolymer with the A group being poly(ethylene oxide) (PEO) and the B group being poly(propylene oxide) (PPO). Its chemical formula is  $[H-(EO)_x(PO)_y(EO)_x-OH]$ , where  $x$  and  $y$  are not given by Sigma Aldrich, but the molecular weight  $M_w = 12.6$  kDa. Due to their biocompatibility, Pluronics have been investigated extensively for pharmaceutical applications, and in particular for drug delivery; reviews can be found in [1, 2, 3]. At concentrations above approximately 12.5 wt. % [4], aqueous solutions of Pluronic will gel at a transition temperature that is close to room temperature. Below this transition temperature, water is a good solvent for both PEO and PPO. In this case, solutions of Pluronic contain mainly non-interacting unimers [4] and exhibit a Newtonian response to steady shear [5]. As the temperature  $T$  is increased, the hydrophobicity of the PPO block increases and its solubility decreases, leading to the formation of micelles consisting of PPO cores surrounded by a PEO shell [4]. The micelles are made up of aggregates of approximately 50 PEO-PPO-PEO chains and have a core radius of approxi-

mately 4.4 nm, independent of concentration and temperature [4]. At low concentrations these micelles are physically separated and do not interact, but above a certain concentration they organize themselves into a lattice and form a soft solid that is generally referred to as a gel. Using small angle neutron scattering (SANS) on Pluronic dissolved in D<sub>2</sub>O, Prud'homme *et al.* [4] found that in the gel state, the micelles pack into a simple cubic lattice with a degree of micelle overlap that depends on concentration. On the other hand, small angle X-ray scattering (SAXS) measurements by Wu *et al.* [6] suggested face-centred cubic packing of the micelles. Using SANS on Pluronic in the gel state, Wanka *et al.* [7] observed a smooth correlation ring, indicative of nearest-neighbour order, along with high intensity spikes superimposed irregularly on the ring, suggesting the additional presence of large crystalline domains.

A comprehensive study of the steady-shear rheology of Pluronic solutions at varying concentration  $c$ , temperature  $T$ , and strain-rate  $\dot{\gamma}$  was recently reported by Jalaal *et al.* [5]. At temperatures below the gel transition, the solutions were found to be Newtonian, with a viscosity that increased with  $c$ . In the gel state, the material was a shear-thinning yield-stress fluid with a flow curve (shear stress as a function of strain rate) accurately described by the Herschel-Bulkley model [4, 5]. At a temperature well above the sol-gel transition temperature, the flow curves were found to be irreproducible [5]. The authors speculated that the irreproducibility may be due to degradation of the gel structure [5]. The breakup of the gel structure and the return of the material to a Newtonian fluid state at high temperatures have been attributed to increasing dehydration of the PEO shells of the micelles as the temperature increases [4]. Hyun *et al.* carried out a large-amplitude oscillatory shear study of Pluronic [8]. At low temperature they identified a Newtonian sol state. In agreement with past work, they found that the material undergoes a transition to a gel state around room temperature. The gel state, which they refer to as a hard-gel state, consists of micelles packed into a cubic lattice with strong entanglements between the PEO chains in overlapping micelles, consistent with past studies of the structure of Pluronic [4]. At temperatures between the Newtonian sol and the hard-gel states, a so-called soft-gel state was identified. This was described as consisting of clusters of micelles



dispersed in the solvent, with the size of the clusters increasing as the temperature is increased towards the hard-gel state [8, 9].  $V(f)$  There have been many studies of the low-temperature sol-gel phase transition of Pluronic F127 solutions. These have typically been based on rheological measurements, scattering, or a vial-tilting method. In previous rheological studies, the low-temperature sol-gel transition point has been defined to be the temperature at which a measurable yield-stress can be determined from the flow curve [5], or the temperature at which a sharp increase in shear viscosity is observed [10, 11]. Using scattering techniques, the transition to the gel phase has been identified by the appearance of anisotropic spikes superimposed on the correlation rings in SANS studies [12, 4, 7], by the appearance of Bragg diffraction peaks in SAXS studies [6], and by an increase in the hydrodynamic radius measured using dynamic light scattering [6]. A form of the vial-tilting method in which the temperature is increased and then the sample holder is inverted has been used; if no fluidity was observed after a given time then the material was considered to be a gel [13, 14]. Gel permeation chromatography and self-diffusion experiments were used to determine the gel point in Ref. [15]. While the above studies all cite the usage of Pluronic F127, the actual chemical formula quoted differs from study to study: Jalaal *et al.* [5] and Prud'homme *et al.* [4] used  $[\text{H}-(\text{EO})_{100}(\text{PO})_{65}(\text{EO})_{100}-\text{OH}]$ , Wu *et al.* [6] used  $[\text{H}-(\text{EO})_{99}(\text{PO})_{69}(\text{EO})_{99}-\text{OH}]$ , Jalaal and Stoeber [10] and Stoeber *et al.* [11] used  $[\text{H}-(\text{EO})_{106}(\text{PO})_{70}(\text{EO})_{106}-\text{OH}]$ , Mortensen *et al.* [12] and Malmsten *et al.* [15] used  $[\text{H}-(\text{EO})_{99}(\text{PO})_{65}(\text{EO})_{99}-\text{OH}]$ , and Pandit *et al.* [13] do not explicitly state the chemical formula, only that it follows a 2:1 EO:PO monomer number ratio. This suggests that individual samples of Pluronic F127 may differ in their chemical composition. This may have a significant influence on the phase transition temperatures of the solutions and should be taken into account when directly comparing these works.

The present study was motivated by the question of the thermoreversibility of the gelation process and by the irreproducibility of the flow curve at high temperature recently observed by Jalaal *et al.* [5] Previous work has focused on the properties of the sol and gel states themselves. Here we perform a detailed study of both the high- and low-temperature transitions between

the sol and gel phases. We investigate the thermoreversibility and hysteresis of the phase transitions, and the rheological equilibration of the system following a change in temperature. We interpret the results in terms of the physical processes involved in the formation and breakup of the gel state. Understanding these processes may be significant in biomedical applications, since it is important to understand how the gel and the micelles respond to changes in temperature for controlling drug delivery. From a more fundamental perspective, we develop a better understanding of the kinetics of the formation and dissolution of micelles and the gel structure as a function of temperature.

## 4.2 Materials and Methods

Pluronic F127 with a molecular weight of 12.6 kDa was obtained from Sigma Aldrich Canada and was used without any further modification. The chemical formula is approximately  $[H-(EO)_{100}(PO)_{65}(EO)_{100}-OH]$  [5]. Aqueous solutions with polymer concentrations of 5, 10, 14, 16, 18, and 20 wt. % were prepared by mixing the polymer into de-ionized water at 4 °C. The water was passed through a 0.2  $\mu\text{m}$  nylon filter before the polymer was added. The temperature was held at 4 °C while the solution was mixed with a rotary mixer for 24 hours. The solutions were then allowed to sit for at least 48 hours in a refrigerator before use and were typically used within a few weeks.

Rheological measurements were performed using an Anton-Paar MCR302 shear rheometer in strain-controlled mode with a Couette-cell geometry. The Couette cell consists of a rotating inner cylinder with radius 13.328 mm and height 39.984 mm, and a fixed outer cylindrical cup with radius 14.459 mm. This geometry is well-suited for the measurement of low-viscosity fluids and allows for management of evaporation at high temperatures. Solutions were loaded directly from the refrigerator into the cup of the Couette cell, which was held at a temperature of 10 °C, and the measurement bob was immediately lowered into the fluid. This temperature was chosen to ensure that the fluid remained in the sol state during the loading procedure. A

thin layer of 20 cSt silicone fluid (Clearco Products) was then placed on top of the solution to prevent evaporation. No mixing between the oil and the Pluronic solutions was observed, and we confirmed that the oil had no noticeable influence on the measurements. To further limit evaporation, a custom environmental housing containing a small reservoir filled with water covered the sample.

Strain amplitude sweeps and frequency sweeps were carried out as a function of temperature from 10 to 85 °C in 5 °C steps. In addition, to obtain measurements at the phase transition temperatures, the temperature was increased from below the transition in a linear ramp (as described below) until a dramatic change in  $G'$  and  $G''$  was observed, at which point the temperature was fixed. After a change in temperature, the system was allowed to equilibrate for 30 minutes before measurements were taken. The strain amplitude  $\gamma$  was then swept from 0.01% to 100% at a fixed angular frequency of  $\omega = 1$  rad/s. Frequency sweeps were then performed at a strain amplitude of  $\gamma = 0.2\%$  from 300 to 0.01 rad/s. This is within the linear viscoelastic regime, as discussed below.

We also measured the moduli as the temperature was varied in two ways: in a continuous ramp, and in discrete steps. In both cases the temperature was controlled using Anton-Paar's C-PTD 200 Peltier control system, which is designed to minimize vertical temperature gradients in the Couette cell [16]. For the continuous experiments, the temperature was raised from 10 to 85 °C at a constant rate of 6 °C per h, then lowered back to 10 °C at the same rate. In experiments with discrete temperature steps, the temperature was increased or decreased by a discrete amount  $\Delta T$  and held at the new temperature for a time  $\Delta t$  while data were recorded. Approximately 300 seconds were required for the temperature to equilibrate after a step. When the system was in the sol or gel state, far from any phase transition,  $\Delta T$  was chosen to be 1 or 2 °C and  $\Delta t$  was 15 or 30 min. Near a transition,  $\Delta T$  was between 0.1 and 0.5 °C and  $\Delta t$  ranged from 1 to 8 h, depending on how long it took for the rheological properties of the material to reach equilibrium. In both cases,  $\gamma$  and  $\omega$  were fixed at 1% and 1 rad/s, respectively, and  $G'(t)$  and  $G''(t)$  were continuously recorded every 5 seconds.

## 4.3 Results

### 4.3.1 Dynamic Rheology

The viscoelastic behaviour of the 18 wt. % Pluronic solution over the range of temperatures studied is illustrated in Figs. 4.1 and 4.2, which show the dependence of  $G'$  and  $G''$  on strain amplitude  $\gamma$  and frequency  $\omega$ , respectively. These figures show data recorded at six temperatures that increase counter-clockwise from (a) to (f). We will discuss the data in order of increasing temperature.

The amplitude dependence of the moduli at  $\omega = 1$  rad/s is reported in Fig. 4.1. At the lowest temperature studied ( $T = 10$  °C, Fig. 4.1(a)),  $G'' > G'$  for all  $\gamma$ ,  $G'$  is too small to measure, and  $G''$  is independent of  $\gamma$ . This is liquid-like behaviour, confirming that the material is in a sol state at this temperature. The scatter at low strain is due to the fact that these measurements are close to the lower torque limit of the rheometer. At a temperature within the sol-gel transition ( $T = 24.3$  °C, Fig. 4.1(b)),  $G'$  and  $G''$  are approximately constant at low  $\gamma$ , with  $G'$  slightly larger than  $G''$ . At approximately  $\gamma = 1.5\%$ , the moduli cross over before decreasing at higher strain amplitude. At  $T = 35$  and  $55$  °C (Fig. 4.1(c) and (d))  $G'$  is constant at low  $\gamma$  before starting to decrease at  $\gamma \approx 0.4\%$ .  $G''$  is also constant at low  $\gamma$ , then increases to a peak at  $\gamma \approx 2\%$  before decreasing at higher  $\gamma$ . The moduli cross over at  $\gamma \approx 4\%$ . This behaviour is characteristic of the gel state, with the linear viscoelastic regime extending up to  $\gamma \approx 0.4\%$ . The scatter in  $G''$  at low  $\gamma$  increases as the temperature is increased within the gel state.

Within the high-temperature gel-to-sol transition ( $T = 66$  °C, Fig. 4.1(e)), both moduli decrease as  $\gamma$  increases from  $\gamma = 0.01\%$  to  $\gamma \approx 6\%$ , with  $G'' > G'$ . The moduli then increase as  $\gamma$  is increased further to  $\gamma \approx 20\%$ . Above  $\gamma \approx 30\%$ ,  $G''$  and  $G'$  decrease. This is different from the behaviour seen in (Fig. 4.1(b)), presumably due to the material being at a different stage along the transition between sol and gel, as discussed later. This behaviour is very similar to that observed previously [8], as discussed in Sec. 4.4.

At the highest temperature studied ( $T = 85$  °C, Fig. 4.1(f)), the material is again in a

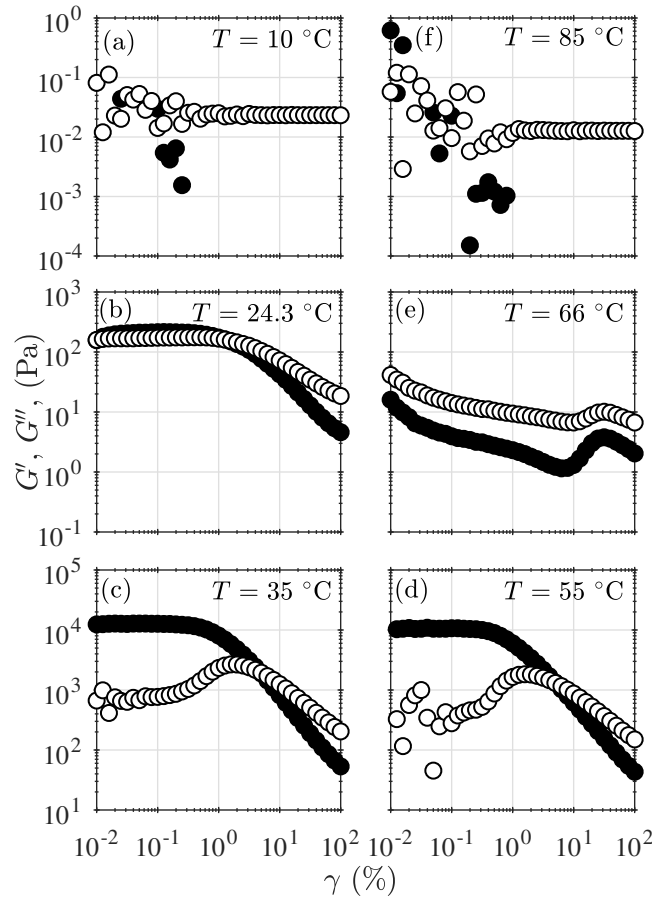


Figure 4.1:  $G'$  (filled symbols) and  $G''$  (open symbols) vs. strain amplitude  $\gamma$  at an angular frequency  $\omega = 1$  rad/s for the 18 wt. % Pluronic solution at temperatures that increase counter-clockwise from  $T = 10$  °C in (a), to  $T = 85$  °C in (f). The data are at temperatures in: (a) the low-temperature sol state, (b) the low-temperature sol-gel transition, (c) the gel state, a few degrees warmer than the sol-gel transition, (d) the gel state, a few degrees cooler than the gel-sol transition (e) the high-temperature gel-sol transition, and (f) the high-temperature sol state. Data in rheologically similar states share the same row.

sol state and exhibits behaviour very similar to that seen in the low-temperature sol state (Fig. 4.1(a)).

The extent of the linear viscoelastic regime varies with temperature, and within a phase transition the moduli depend on strain amplitude down to the smallest values of  $\gamma$  studied. We chose a value of 0.2% for the frequency sweeps presented below. For the temperature ramp studies presented in Sec. 4.3.2 and C we chose  $\gamma = 1.0\%$  to improve the signal-to-noise ratio of the data.

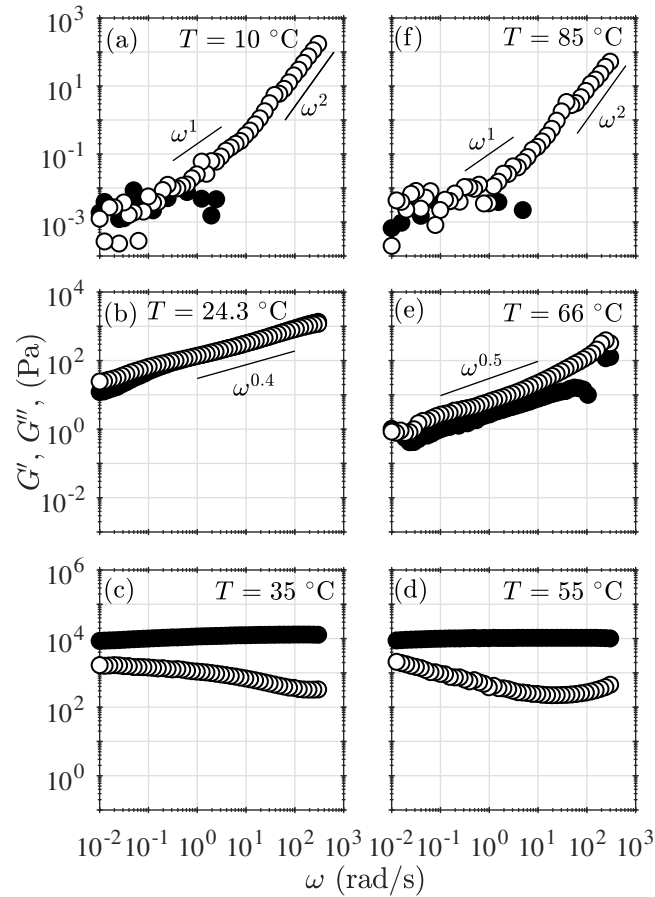


Figure 4.2:  $G'$  (filled symbols) and  $G''$  (open symbols) vs. angular frequency  $\omega$  at a strain amplitude  $\gamma = 0.2\%$  for the 18 wt. % Pluronic solution at temperatures that increase counter-clockwise from  $T = 10^\circ\text{C}$  in (a), to  $T = 85^\circ\text{C}$  in (f). The data are at temperatures in: (a) the low-temperature sol state, (b) the low-temperature sol-gel transition, (c) the gel state, a few degrees warmer than the sol-gel transition, (d) the gel state, a few degrees cooler than the gel-sol transition (e) the high-temperature gel-sol transition, and (f) the high-temperature sol state. Data in rheologically similar states share the same row.

The frequency dependence of  $G'$  and  $G''$  at the same six temperatures is shown in Fig. 4.2. In the low-temperature sol state (Fig. 4.2 (a)), the viscosity of the fluid is small and it is difficult to measure the moduli with our apparatus. At low frequency,  $G''$  appears flat and noisy due to the low-torque limit of the rheometer. The measured values of  $G'$  in this frequency range are likely due to noise and not the material. For  $1 \lesssim \omega \lesssim 10$  rad/s,  $G'' \sim \omega^1$ , consistent with the material being in the sol state. At high frequency,  $G'' \sim \omega^2$ , which reflects the high-frequency inertia limit of the rheometer and not the material properties [17].

Within the low temperature sol-gel transition ( $T = 24.3$  °C Fig. 4.2 (b)), the material is viscoelastic, and at the temperature shown,  $G''$  is slightly larger than  $G'$  at low frequencies. The moduli cross over around  $\omega = 5$  rad/s, and  $G' > G''$  at higher frequencies. The plots of  $G'$  and  $G''$  are approximately parallel and both increase approximately as  $\omega^{0.4}$ , indicating that this temperature is close to the gel point of the material [18].

In the gel state (Fig. 4.2 (c) and (d)),  $G'$  is larger than  $G''$  over the full range of frequencies studied.  $G'$  increases slowly with frequency while  $G''$  has a weak minimum that depends on temperature. This minimum is clearly visible at  $\omega \sim 30$  rad/s for  $T = 55$  °C (Fig. 4.2 (d)), but it is less clear at  $T = 35$  °C (Fig. 4.2 (c)). The low-frequency behaviour suggests the possibility that the moduli may cross over at some frequency below the range studied. A similar crossover may exist at much higher frequencies.

Within the high-temperature gel-sol transition ( $T = 66$  °C, Fig. 4.2 (e)), the material is viscoelastic, and at the temperature shown,  $G'' > G'$  at all frequencies. The plots of  $G'$  and  $G''$  are approximately parallel and both increase approximately as  $\omega^{0.5}$ , indicating that this temperature is slightly higher than the gel point of the material during this transition.

At the highest temperature studied (Fig. 4.2 (f)), the material has returned to a sol state and exhibits behaviour similar to that in the low-temperature sol state (Fig. 4.2(a)).

### 4.3.2 Phase Transitions

We studied the variation of the moduli at  $\omega = 1$  rad/s and  $\gamma = 1\%$  as the temperature was raised at a constant rate from the low-temperature sol state, through the gel state to the high-temperature sol state and back. The heating and cooling curves for concentrations  $c = 16, 18,$  and  $20$  wt. % are shown in Fig. 4.3. A strain amplitude of  $1\%$  was chosen to reduce the scatter in the data; this choice did not qualitatively affect the results.

Initially, at low temperatures, the fluid is in a sol state,  $G'' > G'$ , and  $G'$  is too small to measure with our apparatus. As  $T$  is increased,  $G''$  increases relatively slowly until a characteristic temperature  $T_1$ , at which both  $G'$  and  $G''$  increase dramatically. We define  $T_1$  as the

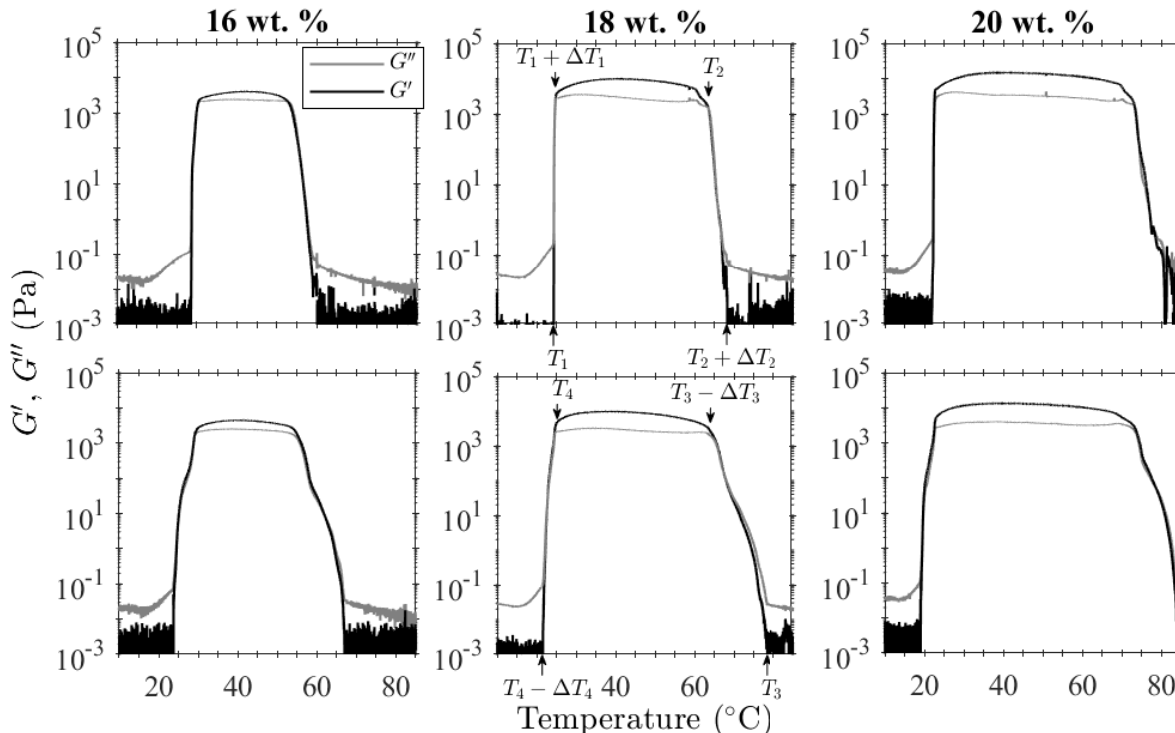


Figure 4.3:  $G'$  (black) and  $G''$  (gray) measured at  $\omega = 1$  rad/s and  $\gamma = 1\%$  for aqueous solutions of Pluronic with concentrations 16 wt. % (left), 18 wt. % (center) and 20 wt. % (right) while heating (top) and cooling (bottom) at a rate of  $6^\circ\text{C}$  per hour.

start of the sol-gel transition. The transition occurs over a temperature range  $\Delta T_1$ . The end of the transition is marked by the sudden change in slope of the moduli as a function of temperature, as indicated in Fig. 4.3 by the arrow at  $T_1 + \Delta T_1$ . While  $G'' > G'$  at the start of the transition, the moduli cross over partway through the transition, so that  $G' > G''$  by the end. The gel state, in which  $G' > G''$  and the moduli depend weakly on temperature, persists up to a second characteristic temperature  $T_2$  at which both  $G'$  and  $G''$  begin to decrease significantly as the material starts to transition to the high-temperature sol state. This transition occurs over a temperature range  $\Delta T_2$ . We define the end of this transition to be the temperature at which  $G'$  is no longer measurable with our apparatus. In the high-temperature sol state,  $G''$  is again greater than  $G'$ , which is too small to measure.

The reverse process is observed on cooling, but with some important differences. As the temperature is lowered,  $G'$  and  $G''$  begin to increase strongly at  $T = T_3$ , which is greater than



$T_2 + \Delta T_2$ , as the material starts to transition from the high-temperature sol state back to the gel state. This transition occurs over a range  $\Delta T_3$ , where  $\Delta T_3 > \Delta T_2$ . Finally, at  $T = T_4$ , which is lower than  $T_1 + \Delta T_1$ ,  $G'$  and  $G''$  start to decrease rapidly as the material transitions back to the original low temperature sol state. The temperatures at which the transitions begin and end when heating and cooling are not equal, and the gel phase exists over a wider temperature range on cooling than on heating. The cooling transitions also span a larger range of temperature than the corresponding heating transitions, i.e.,  $\Delta T_3 > \Delta T_2$  and  $\Delta T_4 > \Delta T_1$ .

The rate at which the moduli change with  $T$  varies across the transitions. Both cooling transitions appear to involve two distinct steps, with distinct shoulders visible partway through the transitions in the lower row of Fig. 4.3. The high-temperature gel-sol transition also occurs in two steps, but the effect is subtle compared to the cooling transitions and is difficult to discern in Fig. 4.3. No clear step is visible during the low-temperature sol-gel transitions seen in the top row of Fig. 3, although a change of slope can be discerned partway through the transition. In all cases the shoulder or change in slope occurs near the temperature at which the moduli cross over.

The moduli of the 14 wt. % solution also increased and then decreased as the temperature of the solution was increased, but  $G''$  remained larger than  $G'$  at all temperatures and no gel state was observed. On cooling,  $G'$  did become larger than  $G''$  during the high-temperature transition, and there was a small range of temperature over which both moduli did not change substantially with temperature which we identified as a gel state. We observed no indication of any phase transition for temperatures up to 45 °C for  $c = 10$  wt. %, and up to 48 °C for  $c = 5$  wt. %. The temperatures and temperature ranges of the phase transitions determined from these temperature-ramp experiments are listed for all of the concentrations studied in Table 4.1(a).

### 4.3.3 Rheological Relaxation

We also studied how the moduli of the 16, 18, and 20 wt. % solutions change with time following a step in temperature. During this experiment, small amplitude oscillations with

Table 4.1: a) Temperatures  $T_i$  at the start of a phase transition and the corresponding width of the transition  $\Delta T_i$  measured from the continuous heating and cooling ramps shown in Fig. 4.3. The uncertainties in  $T_i$  and  $\Delta T_i$  are approximately  $\pm 0.01$  °C. b) Temperatures  $T_i$  at which the rheological relaxation time becomes long, and the corresponding range of temperatures over which long relaxation times  $\Delta T_i$  are observed, obtained from the temperature-step experiments shown in Figs 4.4-4.8. The uncertainties in the last digit of the entries in part (b) are given in parentheses and depend on the step size used in the experiment, as discussed in Sec. 4.3.3.

	$c$ (wt. %)	$T_1, \Delta T_1$ (°C)	$T_2, \Delta T_2$ (°C)	$T_3, \Delta T_3$ (°C)	$T_4, \Delta T_4$ (°C)
(a)	14	38.87, 3.01	41.88, 5.53	38.98, 7.71	48.48, 7.84
	16	28.51, 2.27	52.15, 6.87	67.00, 12.82	29.27, 5.54
	18	24.25, 0.61	62.80, 5.44	78.27, 15.24	24.59, 3.03
	20	21.93, 0.85	72.56, 8.41	83.73, 10.49	22.80, 3.80
(b)	16	26.5(5), 2.9(3)	50(1), 16(1)	73.8(3), 17.8(5)	30.5(5), 7.3(3)
	18	24.1(1), 1.4(3)	61(1), 8.0(7)	81(1), 20(1)	31(1), 9.5(5)
	20	21.25(5), 1.60(4)	67.5(5), 17.5(3)	85(0), 13.0(3)	23.5(0), 7.3(3)

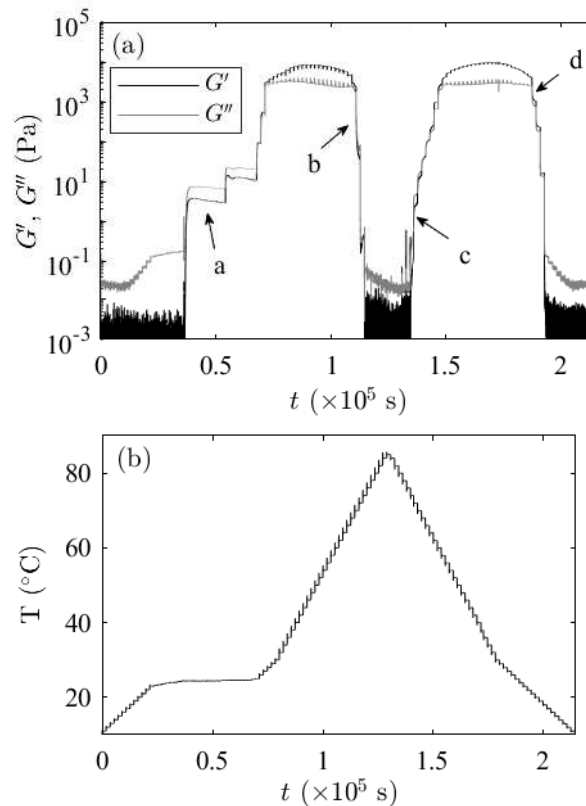


Figure 4.4: (a)  $G'(t)$  (black) and  $G''(t)$  (gray) measured at  $\omega = 1$  rad/s and  $\gamma = 1\%$  during an experiment in which the temperature of the 18 wt. % solution was changed in discrete steps. (b) The temperature as a function of time. The steps indicated by the arrows in (a) correspond to the relaxation curves shown in Fig. 4.7.

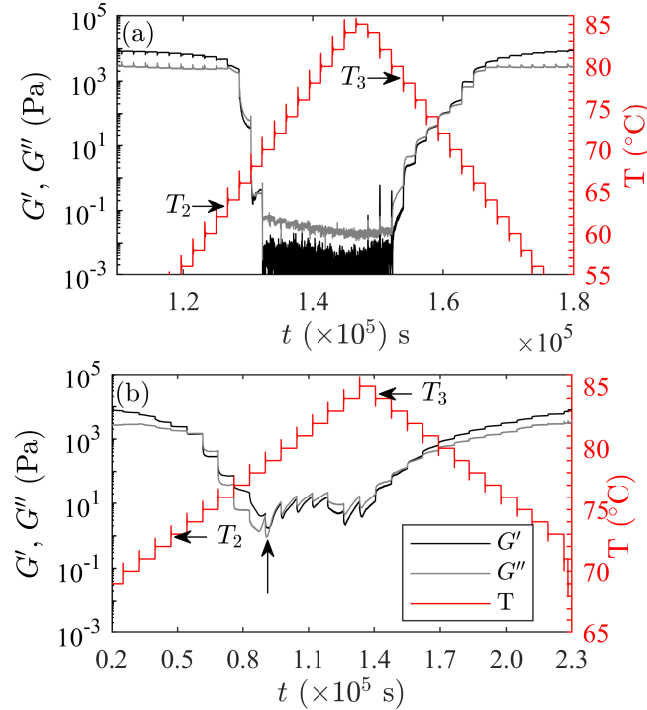


Figure 4.5:  $G'(t)$  (black) and  $G''(t)$  (gray) measured at  $\omega = 1$  rad/s and  $\gamma = 1\%$  in the high temperature regime of the discrete temperature study of the (a) 18 wt. % and (b) 20 wt. % solutions. The temperature profile is the red step-like curve (see color figure online) using the right axis. The vertical arrow indicates the change in behaviour discussed in the text. The transition temperatures  $T_2$  and  $T_3$  determined from the continuous heating and cooling ramp experiments are shown with the labelled arrows.

$\omega = 1$  rad/s and  $\gamma = 1\%$  were applied continuously and  $G'(t)$  and  $G''(t)$  were recorded every 5 seconds. Figure 4.4(a) shows the moduli of the 18 wt. % solution corresponding to the sequence of temperature steps shown in Fig. 4.4(b). The high-temperature portion of the same data is shown in more detail in Fig. 4.5(a). Following a step in temperature, the moduli evolve, eventually approaching a steady-state value corresponding to the new system temperature. As noted above, approximately 300 seconds were required for the temperature controller to settle at the new temperature. At temperatures within the sol or gel states, the moduli of the 18 wt. % solution reach their new equilibrium values within this time, indicating that the rheological relaxation of the material is at least as fast as the equilibration of the system temperature. As seen in Fig. 4.5(a), however, the material relaxation time becomes significantly longer near

the phase transitions, reflecting the time required for significant changes to the microstructure of the material to occur and equilibrate. This is analyzed more quantitatively below. These long relaxation times suggest that the Pluronic is not at rheological equilibrium at temperatures within the phase transitions in the ramp experiments discussed above. This is discussed further in Sec. 4.4.

The behaviour of the 16 wt. % solution was similar to that shown for the 18 wt. % solution in Figs. 4.4 and 4.5(a). The high-temperature behaviour of the 20 wt. % solution was somewhat different, however, and is shown in Fig. 4.5(b). In contrast to what is seen at lower concentrations and in the continuous-ramp experiment, the moduli of the 20 wt. % solution in and above the high temperature phase transition remain roughly 1000 times larger than their values in the other sol states. At the earliest times shown in Fig. 4.5(b), the temperature is increasing towards the high-temperature gel-sol transition, and, as expected, the moduli decrease with each step. At the step indicated by the vertical arrow in Fig. 4.5(b), however, the behaviour changes. Following a step increase in temperature, there is an initial rapid decrease in the moduli followed by a slow increase. Once  $T$  has reached its maximum and cooling begins, the moduli increase monotonically after each decrease in temperature as the material returns to the gel state, in agreement with what is observed for the lower concentrations. During the continuous-ramp experiment, in contrast,  $G'$  and  $G''$  reached low values, consistent with those in the other sol states, at high temperature. Given the long relaxation times observed in the temperature-step experiments, however, these data were likely not at rheological equilibrium. While we observe a low-viscosity sol state at high temperatures for the 16 and 18 wt. % solutions, our data suggest that the equilibrium state at 20 wt. % is instead a viscoelastic liquid with moduli a factor of  $10^3$  larger than at lower concentrations.

We define temperature ranges over which the relaxation of the moduli is slow in analogy with the transition temperatures and ranges discussed in the context of the continuous-ramp experiments. The uncertainties in the  $T_i$  in this case are taken to be half the size of the temperature step. The results are given in part (b) of Table 4.1. The  $T_i$  determined from the step

experiments differ slightly from the those determined from the continuous ramp experiments. This difference can be seen, for example, in Fig. 4.5(a). The moduli increase significantly after the temperature decreases to  $T = 80.00$  °C, while the value of  $T_3$  obtained from the continuous ramp experiments was  $77.47$  °C. This difference is more evident in Fig. 4.8, discussed below.

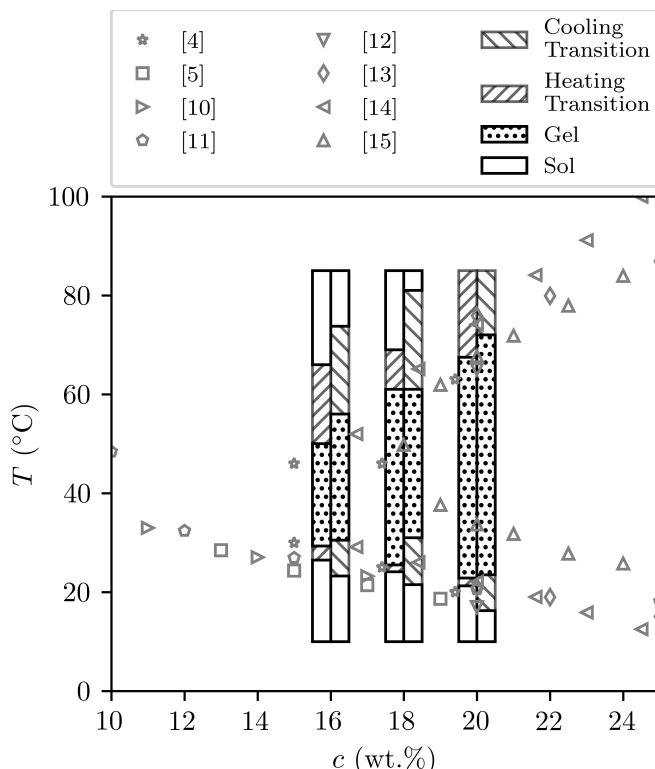


Figure 4.6: Temperature-concentration phase diagram for aqueous solutions of Pluronic F127. The results of the present work are displayed as the hatched bars, as described in the legend. For a given concentration, the left half of the bar shows the states observed when heating, while the right half shows the states observed when cooling. The width of the bars has no physical significance. Results from previous work are shown by the symbols, with corresponding references given in the legend.

The temperature ranges at which long relaxation times were observed for the 16, 18, and 20 wt. % concentrations are listed in Table 4.1(b) and are plotted as a phase diagram in Fig. 4.6. As the concentration is increased, the low-temperature transitions occur at lower temperatures, and the high temperature-transitions occur at higher temperatures. Transition temperatures reported in past work are also shown in Fig. 4.6. Our results for both the low-temperature and high-temperature phase transition temperatures agree with previous results to within a few

degrees, with a few exceptions. In particular, we observe a gel phase for  $c \geq 14$  wt. %. In contrast, the results of Ref. [15] suggest that  $c = 18$  wt. % is the lower concentration limit for the existence of the gel, while several other studies observed a low-temperature sol-gel transition for  $c < 14$  wt. %.

At temperatures within the sol or gel states, the moduli equilibrate within the 300 second equilibration time of the temperature controller. These data are therefore not considered further. Within the phase transitions, however, the relaxation times were substantially longer, as mentioned above. In these cases, we found that the relaxation of the moduli could be described by a decaying exponential function or the sum of two exponentially decaying terms in the form

$$G(t) = G_{\infty} + G_1 e^{-t/\tau_s} + G_2 e^{-t/\tau_f}, \quad (4.1)$$

where  $t = 0$  is chosen to be a time after the temperature controller reached equilibrium.  $G(t)$  is either  $G'(t)$  or  $G''(t)$ ,  $G_{\infty}$  is the equilibrium viscous or elastic modulus at long times,  $\tau_f$  and  $\tau_s$  are ‘fast’ and ‘slow’ relaxation times, respectively, and  $G_1$  and  $G_2$  are coefficients that may be negative or positive, depending on the sign of the change in  $G$ . Eq. 4.1 was fit to the measured moduli using a standard nonlinear least squares fitting routine in Matlab [19]. In many cases, only one exponential term was needed to accurately describe the data. When this was the case, the fitted relaxation time was labeled as  $\tau_s$ . In a few cases, such as the relaxation shown in Fig. 4.7(c) below, the fast relaxation process was well defined, but the slow relaxation process could not be constrained by the fit. In such cases, a constraint on  $G_{\infty}$  was imposed manually to force convergence. The resulting data points are shaded gray in Fig. 4.8 below.

Four typical relaxation curves measured in the 18 wt. % solution and corresponding to the four steps indicated by letters in Fig. 4.4(a), are shown in Fig. 4.7, along with fits of Eq. 4.1 to the curves. These curves illustrate the different types of relaxation behaviour observed within the phase transitions. Fig. 4.7(a) shows the evolution of the moduli observed when the temperature is increased from a temperature within the sol state to a temperature slightly above

$T_1$ , at which point the moduli increase significantly over time. Following the step increase in temperature, the moduli do not start to increase until about five minutes after the temperature equilibrates. For all other steps within this and other transitions, there was no measurable delay. After the delay,  $G'$  and  $G''$  rapidly increase and overshoot their equilibrium values at the new temperature, which are then approached by a subsequent very slow decrease. For this measurement, the temperature was held constant for 5 hours after the initial step. The moduli do not relax to a constant value in this time and  $G''$  remained larger than  $G'$  for the duration of the measurement. Independent fits of Eq. 4.1 to  $G'(t)$  and  $G''(t)$  give similar relaxation times. For  $G'(t)$ , we find  $\tau_f = 939 \pm 1$  s and  $\tau_s = (1.89 \pm 0.01) \times 10^4$  s, while for  $G''(t)$ ,  $\tau_f = 935 \pm 1$  s and  $\tau_s = (3.54 \pm 0.04) \times 10^4$  s, where the uncertainties are  $\pm 1\sigma$  uncertainties calculated by the curve fitting routine. For brevity, the average and standard deviation of  $\tau_f$  and  $\tau_s$  determined from fits to the two moduli will be given below. Relaxation behaviour similar to that shown in Fig. 4.7(a) is also seen following subsequent temperature increases within the low-temperature sol-gel transition. Note the difference in the scale of the time axis between Fig. 4.7(a) and the other plots in this figure.

Temperature steps within the high-temperature gel-sol transition result in the relaxation behaviour plotted in Fig. 4.7(b). The increase in temperature results in a monotonic decrease in  $G'$  and  $G''$  that was accurately fit by a single exponential decay with, in this particular case,  $\tau_s = 392 \pm 5$  s.

The behaviour plotted in Fig. 4.7(c) is observed when cooling through the high-temperature transition from sol to gel. Here a step decrease in temperature results in a monotonic increase in both moduli. For the case shown, the moduli were accurately fit by a single exponential with  $\tau_s = 1100 \pm 200$  s. The relaxation time is sufficiently long in this case that the rheological properties of the system had still not reached equilibrium by the end of the two-hour waiting time used in the experiment. Finally, the relaxation behaviour observed within the gel-sol cooling transition is plotted in Fig. 4.7(d). A single exponential decay with  $\tau_s = 400 \pm 100$  accurately fit both moduli at this temperature.

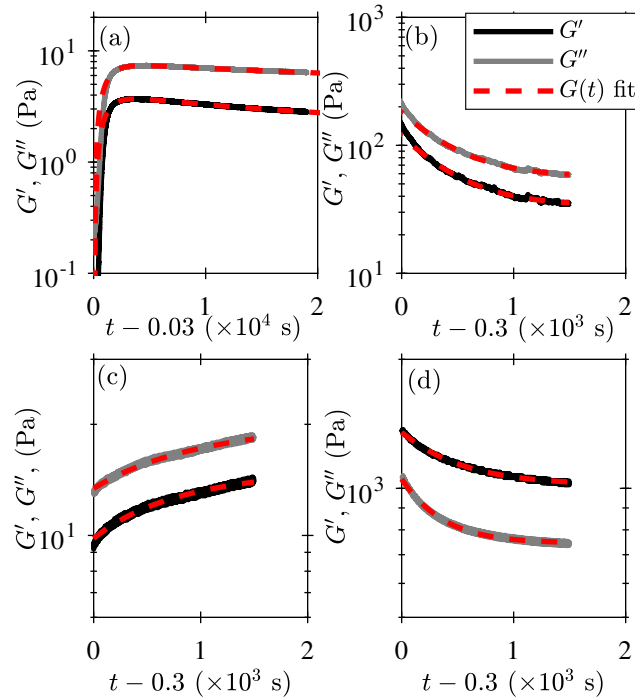


Figure 4.7: Relaxation of the moduli of the 18 wt. % Pluronic solution following a step change in temperature. The four subplots correspond to the steps labeled in Fig. 4.4. The red dashed lines (see color figure online) are independent fits to  $G'(t)$  and  $G''(t)$ . a)  $T = 24.4$  °C (warming), b)  $T = 66$  °C (warming), c)  $T = 76$  °C (cooling), and d)  $T = 25$  °C (cooling).

Figure 4.8 shows the relaxation times for the 16, 18 and 20 wt. % solutions measured following discrete increases and decreases in temperature. For the most part, two exponential terms in Eq. (4.1) were required to fit the relaxations recorded during the low-temperature sol-gel transition, while the relaxations recorded within the two gel-sol transitions and the high-temperature sol-gel transition were well-described by a single exponential decay. The temperature ranges of the transitions determined from the continuous-ramp experiments are also shown for comparison. Although the temperature steps used in the experiments on the 18 wt. % solution were larger than for the 16 and 20 wt. % solutions, the relaxation times measured in the phase transition regions are similar. The temperature ranges over which the relaxation times are long are shifted and broadened compared to the temperature ranges of the transitions measured from the ramp experiments. As noted above, this suggests that the Pluronic falls out of thermal equilibrium when the relaxation becomes slow compared to the time scale of the



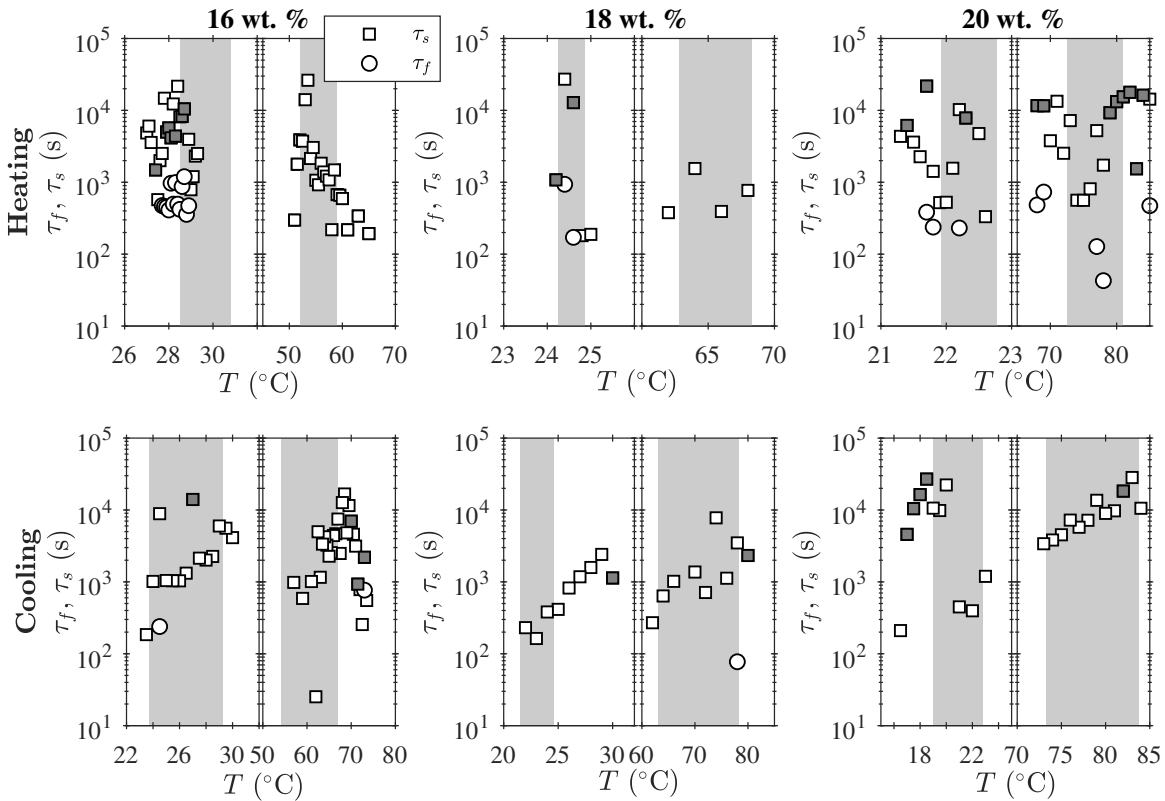


Figure 4.8: Slow and fast relaxation times,  $\tau_s$ , and  $\tau_f$  respectively, determined by fitting  $G'$  and  $G''$  to Eq. 4.1 following a step in  $T$  while heating and cooling. Gray symbols indicate relaxation times that are less reliable, as described in the text. The shaded regions show the temperature range over which the transitions occur, as determined from the continuous temperature ramp experiments.

temperature changes in the ramp experiments. While the relaxation times show some scatter, some trends are apparent. For both cooling transitions, the relaxation times are long at high temperatures and get shorter as the material is cooled through the transition. For the 16 wt. % solution, the relaxation times during the high-temperature gel-sol transition start long, then decrease as the solution is heated through the transition. For the same transition in the 20 wt. % solution, it appears that the relaxation times are again long at low temperatures, decrease on heating in the lower-temperature part of the transition, before then increasing again partway through the transition. This suggests the appearance of a second process driving change in the material and is probably related to the fact that the viscous and elastic moduli are much higher in the high-temperature phase at this concentration than at lower  $c$ . This is discussed in

more detail below. No obvious trend can be identified at the low-temperature sol-gel transition, beyond the fact that the relaxations in this range cannot be described by a single exponential decay. This suggests that more than one physical process is involved in the structural changes that occur during this transition.

## 4.4 Discussion

For  $14 < c < 20$  wt. %, our Pluronic solutions exist in a low-viscosity sol state at low and high temperatures, and are gels at temperatures in between. At  $c = 14$  wt. %, no gel phase was observed when heating the solution, but the material did gel over a small range of temperature when cooling. At  $c = 20$  wt. %, the high-temperature phase is a viscoelastic liquid with moduli  $10^3$  times larger than in the high-temperature sol phase observed at lower concentrations. Our results indicate that both the low-temperature sol state and the high-temperature sol state observed for  $c < 20$  wt. % are Newtonian fluids. Although it is known from previous work that the microstructure in these two sol states is different [4], consisting of non-interacting unimers at low temperature and dehydrated micelles at high temperature, this difference cannot be discerned from our rheological data. Our data show that rheological relaxation of the sols is at least as fast as the relaxation of our temperature control system.

The strain amplitude dependence we observe in the gel phase is typical of that of soft yield-stress fluids, including gels and glasses. Previous results have indicated that Pluronic's gel phase consists of a close-packed cubic array of micelles [4, 6, 7]. When subject to a small strain, the microstructure does not change substantially, and  $G'$  and  $G''$  remain constant. As the strain amplitude increases, the moduli change, indicating that the response of the material has become nonlinear. The decrease in  $G'$  above  $\gamma = 0.5\%$  indicates the breakup of the gel microstructure (i.e., yielding) when the strain is large enough, and Hyun *et al.* suggested that this behaviour can be attributed to the break-up of the cubic gel structure into layers which then slide relative to each other [8]. The dependence of the viscoelastic moduli on frequency seen in

Fig. 4.2(c) and (d) is also typical of gels and soft glassy materials. After a change in temperature within the gel phase, the moduli relax over a time scale governed by the equilibration of the rheometer's temperature control system.

Over the range of temperatures spanned by the sol-gel and gel-sol phase transitions, the rheological properties of the solutions change dramatically, with the moduli increasing by more than five orders of magnitude over the transition from sol to gel. This large increase indicates the development of an interconnected network of micelles that eventually grows to span the sample. Hyun *et al.* have related the strain-amplitude dependence of the moduli within the low-temperature sol-gel transition region to the aggregation of individual micelles into clusters that grow in size until a homogeneous lattice spans the sample [8]. We have measured the rheology at two temperatures between sol and gel that demonstrate how the rheology of Pluronic changes during a transition. During the transition, the material displays a complex strain-amplitude and frequency dependence that varies significantly over the transition. At the temperature plotted in Figs. 4.1(e) and 4.2(e), the magnitudes of the moduli are closer to those measured in the sol state than in the gel state. The rheological response is primarily viscous, however the similar power-law frequency dependence of the moduli indicates that the temperature is slightly higher than the material's gel point [18]. At this temperature, the material is a viscoelastic liquid with some elasticity. This implies the presence of interacting micelles whose structure is weaker than in the gel state. The moduli's dependence on strain amplitude at this temperature is similar to that observed by Hyun *et al.* [8], which they argue is due to strain-induced alignment and additional clustering of micelle clusters. In contrast, the moduli at the temperature plotted in Figs. 4.1(b) and 4.2(b) are larger than in the previous case (subplots (e)) and close to each other in magnitude. This suggests that the micelle clusters at this temperature are larger and interact more strongly than the previous case. This is further supported by our observation that a small applied strain does not alter the microstructure. The similar power-law frequency dependence of the moduli indicates the material is close to its gel point at this temperature [18]. For large enough strain, the moduli decrease due to strain-induced alignment of the clusters as before.

The long relaxation times observed at temperatures within a phase transition indicate that some aspect of the formation and break-up of the large clusters of partially-entangled micelles in this material is extremely slow. When the temperature is increased within the low-temperature sol-to-gel transition,  $G'$  and  $G''$  first increase significantly before then decreasing with a relaxation time of order  $10^4$  s. For most steps within this transition, two exponential terms of opposite sign were needed to fit the data with Eq. 4.1. We attribute the initial increase in moduli to a relatively rapid formation and growth of micelle clusters which overshoots the equilibrium level applicable to the system's new temperature. The subsequent slow decrease of  $G'$  and  $G''$  with time indicates the presence of a competing influence that weakens structure in the fluid. This may be a slow reduction in cluster size or a slow reorganization of the microstructure within clusters. For all concentrations, there was a delay of several min after the first step in temperature from the low-temperature sol state into the sol-gel transition before the moduli began to increase. This may indicate that significant time is required for the initial nucleation of micelles from the unimers in the solution.

When the material is cooled through the same transition, the process is reversed: the material transitions from the gel state to a sol consisting of non-interacting unimers. After a step decrease in temperature from within the gel state to within the gel-sol transition (Fig. 4.7(d)), the moduli slowly decrease. For most steps within this transition, the relaxation of the moduli was well described by a single exponential decay. This suggests that a single physical process is involved in the breakup of the gel, and that this process involves a decrease in the size of the micelle clusters.

The high-temperature gel-sol transition arises from dehydration of the PEO shells of the micelles [4] and the resulting break-up of the gel lattice. After a step increase in temperature within the gel-to-sol transition, the moduli gradually decrease towards an equilibrium state (Fig. 4.7 (b)). This slow relaxation was accurately described by a single exponential decay for the 16 wt. % and 18 wt. % solutions. The behaviour of the 20 wt. % solution is discussed below. Our data suggest that as the temperature is increased within this transition, the equilibrium

microstructure of the system shifts from large clusters with a few dehydrated micelles towards more dehydrated micelles and smaller clusters, and that the decrease in cluster size is a slow process.

When cooling through the high-temperature sol-gel transition (Fig. 4.7 (c)), a step decrease in temperature results in a slow increase over a long time that is well described by a single exponential relaxation. Since the hydration of the micelles is believed to be a very fast process [20], the observed gradual increase in the moduli is likely related to changes in the microstructure as the micelles aggregate into larger clusters.

As presented above, our data suggest that the equilibrium high-temperature phase of the 20 wt. % solution is a viscoelastic fluid with long rheological relaxation times and moduli much larger than those of the Newtonian sol phase seen at lower concentrations. This suggests the presence of some sort of phase transition as a function of concentration at high temperatures, perhaps related to a change in the structure of the micelles that has previously been observed at high temperature [12]. This viscoelastic phase was not seen in our temperature-ramp experiments, presumably because the long relaxation times in this phase prevented the system from equilibrating.

Many physical processes might be expected to influence the microstructural dynamics of Pluronic and so contribute to the observed relaxation of the rheological moduli. The time scales for the insertion of unimers into micelles and the subsequent equilibration of the micelle size distribution have been measured to be of order 10 ms and 100 ms, respectively [21, 22]. Prud'homme *et al.* state that the characteristic relaxation time for a single micelle is on the order of 1 ms [4]. Since the formation and relaxation of micelles are much faster than the time scale of our experiments, and since the structure of the individual micelles does not change once they have formed [4], none of these processes are likely to contribute to the slow rheological relaxation observed in our experiments. The dehydration of PEO at high temperatures has been measured using dielectric spectroscopy to be very fast — on the order of  $10^{-11}$  s [20], which is again too fast to be the relaxation we have observed. In dilute, non-gelling solutions

of Pluronics with a range of molecular weights and PO:EO ratios, Kositzka *et al.* identified a relaxation process with a time scale on the order of 100 ms, which they attributed to the aggregation of micelles near the cloud point at which macrophase separation occurs [23]. This is again much faster than the relaxation we observe. The time scale characteristic of the diffusion of individual micelles in the solution is similarly very short. The relaxation of the moduli we observe is very much slower than all of the above processes, and therefore likely involves structures very much larger than individual micelles.

In the low temperature sol phase, solutions of Pluronic consist of individual unimers. As the temperature is increased, the unimers assemble into micelles, which results in a slight increase in the viscosity of the solution. At a higher temperature the micelles begin to aggregate into clusters, which increase in size as  $T$  continues to increase. The clustering leads to a dramatic increase in both viscosity and elasticity. At some specific temperature the largest cluster of micelles spans the size of the sample. This is the gel point, at which  $G'$  becomes equal to  $G''$  and both moduli display a power-law dependence on frequency [18]. At higher temperatures, the material is rheologically a gel, but it remains heterogeneous on the microscopic scale [24]. As micelles continue to add to the percolation cluster, the moduli continue to increase until essentially all micelles are incorporated into the aggregate and the material is a homogeneous gel. While the addition or removal of an individual micelle from a large cluster is a relatively fast process [22], the clusters as they initially form are likely to be amorphous, with the spatial arrangement of the micelles lacking any long-range order. We suggest that the annealing of this amorphous structure into the crystalline arrangement of micelles observed by neutron and X-ray scattering [6, 7] may be much slower, and is the reason for the slow relaxation of the moduli seen in our experiments.

While past studies have observed the low and high temperature phase transitions in Pluronic solutions, we have investigated the rheology of the material within the transitions in some detail. We have shown that the transitions take place over a range of several degrees and that the transitions observed on cooling occur at different temperatures and over a wider temperature

range than when heating. For the most part, the transition temperatures we have measured agree with previous results to within a few degrees. In contrast to some previous work, we did not observe a gel phase for  $c < 14$  wt. %. This may be due to slight differences in the molecular weight or chemical formula of the Pluronic F127 used, differences in material preparation, or differences in how the transition temperature is defined. Since, as we have observed, the rheological relaxation time of the Pluronic becomes very long near the phase transitions, it is also possible that previous measurements near the phase transitions may not have been performed on samples that were fully in equilibrium.

Jalaal *et al.* [5] reported irreproducibility in the measured flow curve of a concentrated Pluronic solution at high temperature. Based on our results, it seems likely that their material was near or within the high temperature gel-sol transition under the conditions for which irreproducibility was observed. If so, the observed irreproducibility may be a result of the very long rheological relaxation time of the material.

## 4.5 Conclusions

In this chapter we have studied the gelation dynamics of aqueous solutions of Pluronic F127. For  $14 < c < 20$  wt. %, the solutions are Newtonian liquids at temperatures below room temperature. When heated slowly and continuously, the solutions undergo a phase transition to a gel state around room temperature. At a higher temperature, the solutions undergo a second transition back to a Newtonian liquid. Both the sol-gel and gel-sol transitions take place over a range of several degrees. On cooling, the reverse transitions occur at slightly different temperatures and over a larger temperature range, so that the gel phase exists over a broader range of temperature on cooling than on heating. For  $c = 20$  wt. %, the low-temperature behaviour is the same, but the high-temperature phase is a viscoelastic fluid with a long rheological relaxation time rather than a Newtonian liquid. Following a discrete step in temperature, the viscous and elastic moduli relax quickly in the sol and gel phases. At temperatures near the phase tran-

sitions, however, the rheological relaxation time becomes very long. As the gel forms, large aggregates of micelles form and grow, while in the gel-sol transitions these large aggregates break up. The slow relaxation we have observed within the phase transitions may be due to reorganization of the small-scale microstructure within these large aggregates.

## Bibliography

- [1] A. V. Kabanov, P. Lemiux, S. Vinogradov, and V. Alakhov. Pluronic block copolymers: novel functional molecules for gene therapy. *Adv. Drug Deliv. Rev.*, 54:223–233, 2002.
- [2] W. V. Batrakova and A. V. Kabanov. Pluronic block copolymers: Evolution of drug delivery concept from inert nanocarriers to biological response modifiers. *J. Control. Release*, 130:98–106, 2008.
- [3] M. S. H. Akash, K. Rehman, and S. Chen. Pluronic F127-based thermosensitive gels for delivery of therapeutic proteins and peptides. *Polym. Rev.*, 54:573–597, 2014.
- [4] R. K. Prud'homme, G. Wu, and D. K. Schneider. Structure and Rheology Studies of Poly(oxyethyleneoxypropyleneoxyethylene) Aqueous Solution. *Langmuir*, 12:4651–4659, 1996.
- [5] M. Jalaal, G. Cottrell, N. Balmforth, and B. Stoeber. On the rheology of Pluronic F127 aqueous solutions. *J. Rheol.*, 61:139–146, 2017.
- [6] C. Wu, T. Liu, B. Chu, D. K. Schneider, and V. Graziano. Characterization of the PEO-PPO-PEO triblock copolymer and its application as a separation medium in capillary electrophoresis. *Macromolecules*, 30:4574–4583, 1997.
- [7] G Wanka, Heinz Hoffmann, and W Ulbficht. The aggregation behavior of poly-(oxyethylene)-poly-(oxypropylene)- poly-(oxyethylene)-block-copolymers m aqueous solution. *Colloid Polym. Sci.*, 268:101–117, 1990.



- [8] K. Hyun, J. G. Nam, M. Wilhellm, K. H. Ahn, and S. J. Lee. Large amplitude oscillatory shear behavior of PEO-PPO-PEO triblock copolymer solutions. *Rheol. Acta*, 45:239–249, 2006.
- [9] V. Castello, C. Caillet, Fundin J., I. W. Hamley, Z. Yang, and A. Kelarkis. The liquid-solid transition in a micellar solution of a diblock copolymer in water. *J. Chem. Phys.*, 116:10947, 2002.
- [10] M. Jalaal and B. Stoeber. Controlled spreading of thermo-responsive droplets. *Soft Matter*, 1:808–812, 2014.
- [11] B. Stoeber, Z. Yang, D. Liepmann, and S.J. Muller. Flow control in microdevices using thermally responsive triblock copolymers. *J. Microelectromech. Syst.*, 14:207–213, 2005.
- [12] K. Mortensen and Y. Talmon. Cryo-TEM and SANS Microstructural Study of Pluronic Polymer Solutions. *Macromolecules*, 28:8829–8834, 1995.
- [13] N. K. Pandit and J. Kisaka. Loss of gelation ability of Pluronic® F127 in the presence of some salts. *Int. J. Pharm.*, 145:129–136, 1996.
- [14] Y. Lee, H. J. Chung, S. Yeo, C.-H. Ahn, H. Lee, P. B. Messersmith, and T. G. Park. Thermo-sensitive, injectable, and tissue adhesive sol-gel transition hyaluronic acid/pluronic composite hydrogels prepared from bio-inspired catechol-thiol reaction. *Soft Matter*, 6:977, 2010.
- [15] B. Malmsten, M. and Lindman. Self-Assembly in Aqueous Block Copolymer Solutions. *Macromolecules*, 25:5440–5445, 1992.
- [16] G. Raffer. Rotary viscosimeter, U.S. Patent 6,240,770 B1 (2001).
- [17] R. H. Ewoldt, M. T. Johnston, and L. M. Caretta. Complex fluids in biological systems. In S. Spagnolie, editor, *Complex Fluids in Biological Systems*, chapter Experimental challenges of shear rheology: how to avoid bad data. Springer, 2015.

- [18] H. H. Winter and F. Chambon. Analysis of Linear Viscoelasticity of a Crosslinking Polymer at the Gel Point. *J. Rheol.*, 30:367–382, 1986.
- [19] MathWorks. Optimization Toolbox: User’s Guide (R2017a), 2017.
- [20] T. Shikata, M. Okuzono, and N. Sugimoto. Temperature-Dependent Hydration/Dehydration Behavior of Poly(ethylene oxide)s in Aqueous Solution. *Macromolecules*, 46:1956–1961, 2013.
- [21] I. Goldmints, J. F. Holzwarth, K. A. Smith, and T. A. Hatton. Micellar Dynamics in Aqueous Solutions of PEO-PPG-PEO Block Copolymers. *Langmuir*, 13:6130–6134, 1997.
- [22] M. J. Kositzka, C. Bohne, P. Alexandridis, T. A. Hatton, and J. F. Holzwarth. Micellization Dynamics and Impurity Solubilization of the Block-Copolymer L64 in an Aqueous Solution. *Langmuir*, 15:322–325, 1999.
- [23] M. J. Kositzka, C. Bohne, P. Alexandridis, T. Alan Hatton, and J. F. Holzwarth. Dynamics of Micro- and Macrophase Separation of Amphiphilic Block-Copolymers in Aqueous Solution. *Macromolecules*, 32:5539–5551, 1999.
- [24] F. K. Oppong, P. Coussot, and J. R. de Bruyn. Gelation on the microscopic scale. *Phys. Rev. E*, 78:021405, 2008.

# Chapter 5

## Discussion, Conclusions, and Future Work

In this thesis we have presented the simulation, design, and operation of a novel vibrating-wire rheometer. We have also presented a study of the gelation dynamics and long-time relaxation of aqueous solutions of Pluronic F127. In Chap. 2 we showed through two-dimensional numerical simulations using COMSOL that the theory developed by Retsina *et al.* [1, 2] to describe a wire vibrating in a Newtonian fluid accurately describes the simulated behaviour of a wire vibrating in Newtonian fluids with viscosities in the range  $10^{-3} \leq \eta \leq 10^0$  Pa·s. We demonstrated in Chap. 3 that our vibrating-wire device is capable of accurately measuring the viscosity of Newtonian fluids with small viscosities in the range  $3 \times 10^{-4} \lesssim \eta < 3 \times 10^{-2}$  Pa·s, a task that is difficult using conventional shear rheometers. In Appendix A we showed that, although the tension of the wire changes as a function of temperature, our device still accurately measured the viscosity of water at temperatures from 10 to 85°C. Together, these results suggest that our device could serve as a versatile, inexpensive, and accurate viscometer for the measurement of small viscosities.

Chap. 2 also included simulations of the resonant behaviour of a wire vibrating in a shear-thinning fluid described by the Carreau model. Our simulations revealed complex spatial and temporal variation of the shear rate and viscosity in the fluid. This spatiotemporal variation also affected the resonant behaviour of the wire in a way that could be measurable experimentally

and potentially used as a qualitative measure of shear thinning. We found that the theory of a wire vibrating in a Newtonian fluid could describe the resonant behaviour of the wire vibrating in a shear-thinning fluid reasonably well if the viscosity used in the theoretical expression is set equal to the viscosity averaged spatially around the circumference of the wire and temporally over one period of oscillation. The shear rate in the fluid is proportional to the velocity of the wire, which can be tuned by varying the amplitude of the driving force. A larger driving force would result in higher shear rates and therefore a smaller effective viscosity. Future work could focus on amplitude-dependent simulations and experiments in shear-thinning fluids. Such a study could serve to improve our understanding of the behaviour of our device and perhaps allow for the experimental study of shear-thinning behaviour. In addition, the simulation presented in Chap. 2 could easily be modified to simulate the behaviour of a wire vibrating in shear-thickening fluids, which could also be an interesting topic for future research.

We used our new device to measure the viscous and elastic moduli of viscoelastic fluids, a task which has not been done with a vibrating wire device until now. We replaced the dynamic viscosity in the theory for a wire vibrating in a Newtonian fluid with the complex viscosity and fit for the viscous and elastic moduli rather than the viscosity. In Chap. 3 we showed that this modification allowed us to measure the viscous and elastic moduli of a homogeneous polymer solution. Our results were consistent with measurements taken with a shear rheometer. In addition, in App. B we used our device to measure the viscous and elastic moduli of aqueous solutions of Pluronic F127 in both the sol and gel states. The measured viscoelastic moduli in the gel state were again consistent with measurements taken with a shear rheometer. These results demonstrate that in addition to being a good viscometer, our vibrating-wire rheometer is an effective tool for the measurement of the viscoelastic moduli of homogeneous viscoelastic liquids and gels at high frequency. There is a gap in frequency in the data shown in Chap. 3 and App. B between measurements taken using a shear rheometer and those made with our vibrating-wire rheometer. An interesting focus for future research could be to modify the design of our device to measure the viscoelastic moduli at a number of different frequencies

higher than those accessible to standard rotational shear rheometers.

We measured the viscous and elastic moduli of an aging Laponite clay suspension in Chap. 2. Laponite clay suspensions are heterogeneous on the micron scale. Since the amplitude of the wire's oscillations is on the order of microns, our measurements were of the micron-scale rheological properties of the suspension. Measurements of the viscoelastic moduli using a shear rheometer showed that the gel time for the suspension on the macro-scale was on the order of a few minutes, while measurements using our vibrating-wire rheometer revealed a gel time of approximately 2 days. Our results were consistent with past results that used dynamic light scattering and particle tracking methods to measure the gel time at variable length scales [3]. These results show that our device can be used for microrheology. An interesting avenue for future research could be to investigate the dependence of the gel time on the amplitude of the driving force.

In addition to the studies mentioned above, future work could focus on improving the design of the vibrating-wire rheometer. One direction for improvement could be to allow for the tension in the wire to be varied dynamically. In our device, the tension is currently applied by hanging a mass from the wire and then clamping the wire. Once the tension in the wire is set, it cannot be varied without removing it from the fluid and hanging a new mass from it. Our device could be modified to use an auto-tensioning mechanism to dynamically vary the tension in the wire. This could allow for measurements at multiple resonant frequencies without the need to remove the wire from the fluid. For the vibrating-wire rheometer with length  $L = 6$  cm described in Chap. 3, by dynamically varying the tension while maintaining that the tensile stress is within 20-50 % of the tensile yield stress of tungsten, the vacuum resonant frequency could span  $720 < f_0 < 1140$  Hz. By decreasing the wire's length to 5 cm, the upper limit could be extended to 1370 Hz. Furthermore, by using a wire with a smaller radius and shorter length, for example  $R = 0.025$  mm and  $L = 1$  cm, the resonant frequency of the wire could be increased to 6800 Hz. By using an array of wires with different lengths, radii, and tensions, multiple simultaneous measurements could be made at different resonant frequencies. At present our

device requires vibrating-wire holders, a magnet and sample housing, a lock-in amplifier, and a computer for data acquisition. A future iteration of our device could incorporate all of these parts into a single device. Implementing all of the suggestions above into a future iteration of the device should decrease its cost, streamline its operation, and increase the portability and versatility of the vibrating-wire rheometer.

In Chap. 4 we studied the gelation dynamics of aqueous solutions of Pluronic F127 using shear rheometry. For concentrations  $14 < c < 20$  wt.%, the solutions are Newtonian liquids at high and low temperatures and are gels at intermediate temperatures. When the solutions are slowly but continuously heated, they undergo a sol-to-gel transition around room temperature, followed by a gel-to-sol transition at a higher temperature. When they are slowly cooled, the reverse transitions take place over a larger range of temperature so that the width in temperature of the gel phase is larger when cooling than when heating. The solutions gel due to the formation of micelles and subsequent aggregation and ordering of the micelles. We found that when the temperature was changed in small steps near the phase transitions, the rheological relaxation time became very long, up to of order  $10^4$  s. The timescale for the aggregation of micelles is much faster than this and the micelles likely initially pack into structures without long range order. We suggest that the long relaxation time we observed may be due to the annealing of the initial amorphous structure into a more ordered structure that makes up the gel phase. The long relaxation time during the phase transitions could be investigated further through time-resolved small angle neutron scattering, small angle X-ray scattering, and dynamic light scattering.

Overall, in this thesis we have presented a novel device based on the vibrations of a wire under tension for use in viscometry and rheometry. We demonstrated its efficacy through measurements of the viscosity of Newtonian liquids, the bulk-scale viscoelastic properties of homogeneous viscoelastic liquids and gels, and the micron-scale viscoelastic properties of an ageing Laponite clay suspension that is heterogeneous on the micron scale. Our results were consistent with measurements taken with a shear rheometer. Our device can be used in numerous areas of interest in rheology. With careful design modifications, the versatility of our

device could be improved further.

## Bibliography

- [1] T. Retsina, S. M. Richardson, and W. A. Wakeham. The theory of a vibrating-rod densimeter. *Appl. Sci. Res.*, 43:127–158, 1986.
- [2] T. Retsina, S. M. Richardson, and W. A. Wakeham. The theory of a vibrating-rod viscometer. *Appl. Sci. Res.*, 43:325–346, 1987.
- [3] F. K. Oppong, P. Coussot, and J. R. de Bruyn. Gelation on the microscopic scale. *Phys. Rev. E*, 78:021405, 2008.

# Appendix A

## Additional Measurements and Analysis

In this appendix we present additional experimental results and analysis of our vibrating-wire rheometer.

### A.1 Temperature Dependence

We investigated how temperature influenced the behaviour of the vibrating-wire rheometer described in Chap. 2 by measuring the viscosity of de-ionized water at temperatures  $T$  from 10 to 85 °C using a vibrating wire with a length of 5 cm. The temperature was varied using a temperature-controlled circulating bath and was measured using a thermistor placed in the circulating fluid as described in Chap. 2. The temperature was increased in 5 °C steps with a 30 min waiting time between steps. The rate of change of the temperature was limited by the heating and cooling capacity of the circulating bath. The temperature measured in the fluid circulating around the sample vial is shown in Fig. A.1. A single measurement of the resonance curve of the vibrating wire took approximately 2 min, and the data points in Fig. A.1 are the average time and temperature over each measurement. While heating, 30 min was sufficient for the circulating bath to reach a steady temperature. While cooling, 30 min was sufficient except at temperatures between 60 and 50 °C. In this range, the system had not reached thermal equilibrium when the measurements were made.



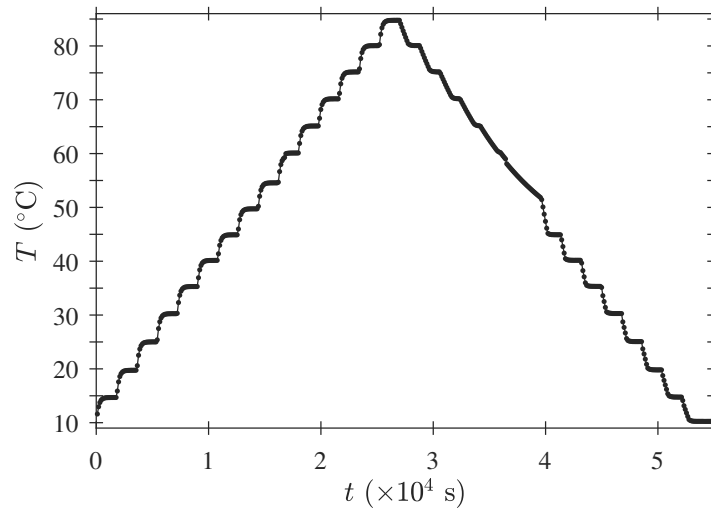


Figure A.1: The temperature measured in the fluid circulating around the vibrating wire vs. time.

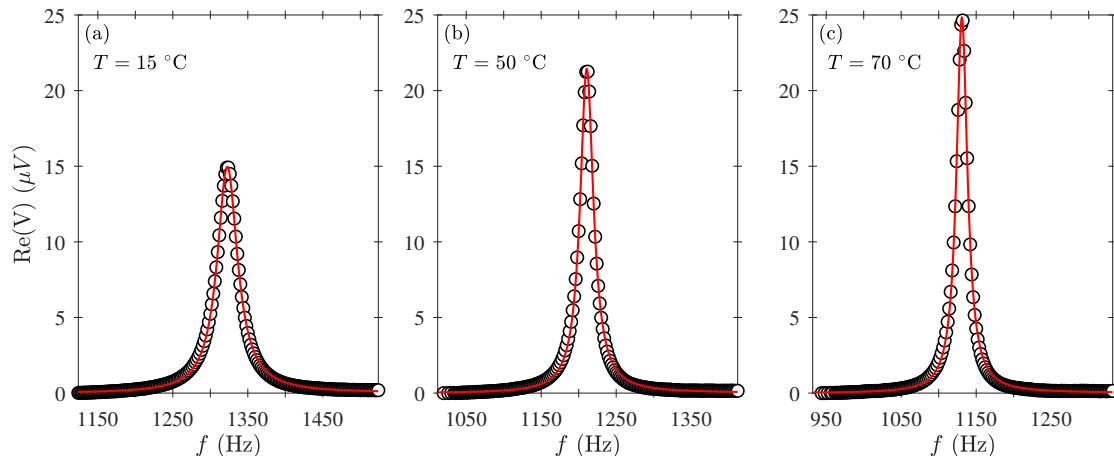


Figure A.2: Fits of Eq. A.1 (red curves) to the real component of the measured voltage from the wire vibrating in water at (a)  $T = 15$ , (b) 50, and (c) 75 °C.

The theoretical expression for the voltage induced in the wire as a function of frequency and fluid properties is re-stated here for convenience:

$$V = a + bf + ic + idf + \frac{\Lambda fi}{f_0^2 - (1 + \beta)f^2 + (\beta' + 2\Delta_0)f^2 i}. \quad (\text{A.1})$$

Fits of the real component of Eq. A.1 to the real component of the induced voltage in the wire in water at  $T = 15$ , 50, and 75 °C are shown in Fig. A.2. For every fit,  $a$ ,  $b$ ,  $c$ ,  $d$ ,  $\Lambda$ ,

$f_0$ , and  $\eta$  were free parameters. The fluid density at each temperature was determined using the NIST Chemistry WebBook [1]. As shown in Fig. A.2, the quality of the fits is excellent at every temperature. As the temperature increases, the resonance curve narrows and shifts to lower frequency. The measured resonant frequency  $f_r$  is plotted against  $T$  in Fig. A.1. As  $T$  increases from 10 to 85 °C,  $f_r$  decreases by almost 300 Hz. On cooling,  $f_r$  increases again, but its value at 15 °C is approximately 10 Hz lower than its starting value prior to heating. This disagrees with what is expected based solely on the properties of water. As  $T$  increases, both the viscosity and density of water decrease; according to Eq. A.1 this should narrow the resonance curve and *increase* the resonant frequency. This discrepancy indicates that the tension in the wire, and therefore its resonant frequency in vacuum  $f_0$ , changes with temperature. Similarly, the difference between the initial and final values of  $f_r$  suggests that the heating-cooling cycle irreversibly changes the tension. The red curve in Fig. A.1 shows the resonant frequency predicted by Eq. A.1, assuming that only the fluid density and viscosity change with temperature. We used borosilicate glass as the backbone of our rheometer because it has a coefficient of thermal expansion similar to that of tungsten. Despite this, Fig. A.3 indicates that we cannot assume that the tension in the wire is independent of temperature.

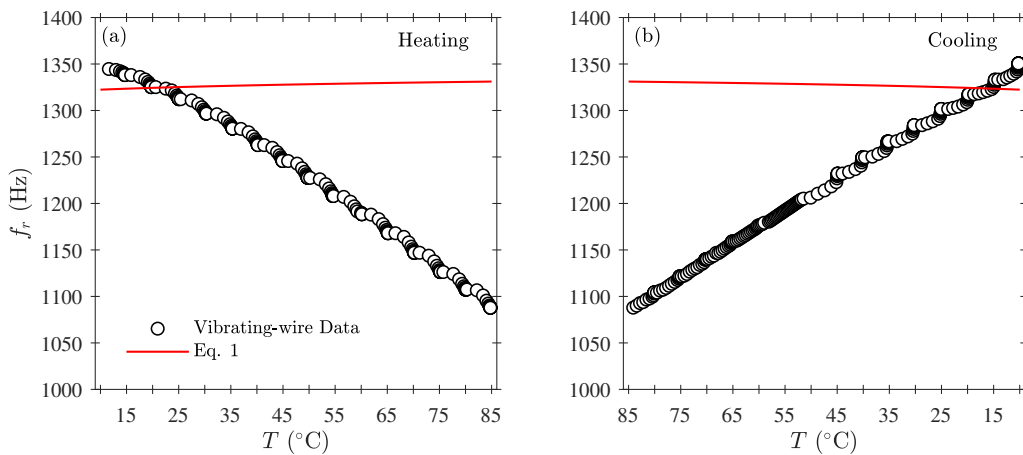


Figure A.3: The measured resonant frequency  $f_r$  and the resonant frequency predicted by Eq. A.1 (red curve) vs.  $T$  when (a) heating, and (b) cooling. The theoretical predictions assume that only the fluid density and viscosity change with temperature.

The viscosity  $\eta_{fit}$  determined from the curve fitting is plotted vs. time in Fig. A.4.  $\eta_{fit}$  is

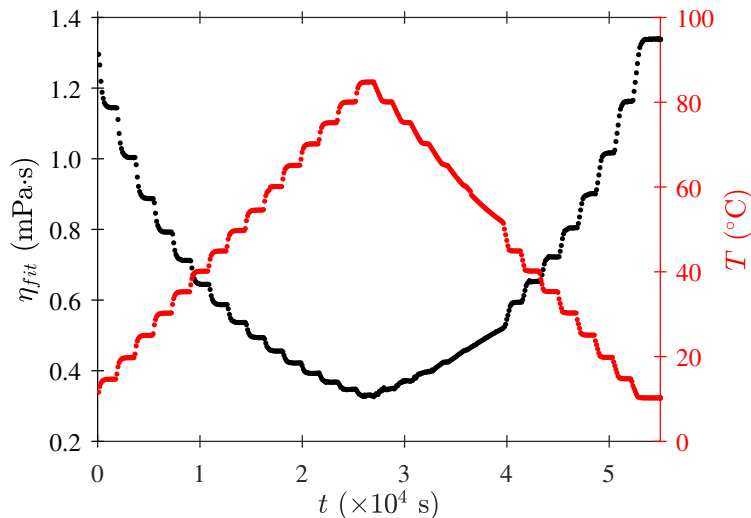


Figure A.4: The viscosity of water (black dots) determined from fits of the real component of Eq. A.1 to the real component of the measured voltage and the temperature in the circulating fluid around the vibrating wire (red dots) vs. time.

smaller at higher temperatures, as expected. The time evolution of the viscosity indicates that, at least for water, the temperature of the fluid in the sample vial follows the temperature of the circulating fluid closely.

The viscosity vs.  $T$  is plotted in Fig. A.5 (a) and (b). Each data point is the mean of 5 measurements at different times near the end of the 30 min waiting time at each step. As mentioned above and shown in Figs. A.1 and A.4, the data are at thermal equilibrium except for a few steps when cooling where the temperature did not reach steady state within the allotted waiting time. For these temperatures,  $\eta_{fit}$  varied more over the 5 measurements than at other temperatures. This variation is reflected in the error bars in Fig A.5 (d) as discussed below. The red curves in Fig. A.5 (a) and (b) show the expected viscosity vs.  $T$ , determined from the NIST Chemistry WebBook [1]. The percentage difference between the fitted and expected viscosities is shown in Fig. A.5 (c) and (d). The viscosities agree to within  $\pm 1\%$  at low temperatures. The percentage difference is larger at higher temperatures but remains within  $\pm 3\%$  except for the point at  $T = 10^\circ\text{C}$  after cooling, where it is closer to 4%. The relatively large error bars on the data in Fig. A.5 (d) between 60 and 50  $^\circ\text{C}$  are due to the fact that, for these temperatures, the

temperature and viscosity had not reached a steady state when the measurements were taken.

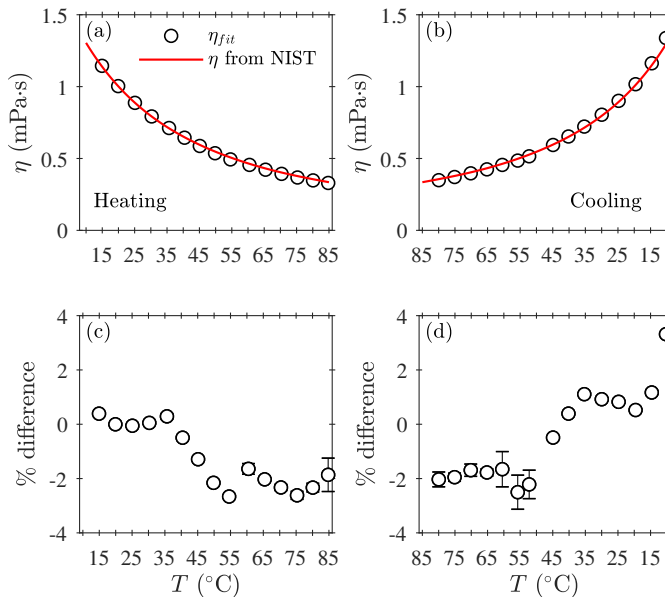


Figure A.5: The mean of 5 measurements of  $\eta_{fit}$  near the end of the 30 min waiting time at each temperature plotted against  $T$  when (a) heating and (b) cooling. The standard deviations are smaller than the symbols in all cases. The red curves are the expected viscosity determined from the NIST Chemistry Webbook. (c) The percentage difference between the mean values of  $\eta_{fit}$  and the expected viscosity when heating, and (d) when cooling. For the most part, the standard deviation of the percentage difference is smaller than the symbols.

Although the agreement between the fitted and expected viscosities becomes poorer at higher temperatures, it is nonetheless quite good over the full range studied. This suggests that our vibrating-wire device is an effective viscometer over the temperature range studied here. The dependence of  $f_0$  on  $T$  indicates that our choice of materials for the construction of the rheometer was not ideal, but since  $f_0$  is treated as a free parameter in our fits, this does not have a significant affect on the results. This in turn validates our procedure of allowing  $f_0$  to be a free parameter in our curve fitting routine.

## A.2 Dependence of the resonance curve on $G'$ and $G''$

When we used Eq. A.1 to study viscoelastic fluids in Chap. 2, we replaced the dynamic viscosity with a complex viscosity,

$$\eta \rightarrow \eta^* = \frac{G' + iG''}{i2\pi f}. \quad (\text{A.2})$$

In Chap 3. we studied how  $\eta$  affected the resonant frequency  $f_r$ , full width at half maximum  $\Delta f$ , and quality factor  $Q$  of the theoretical resonance curves. In this section we study how the viscous and elastic moduli  $G''$  and  $G'$  individually affect  $f_r$ ,  $\Delta f$ , and  $Q$ . We calculated

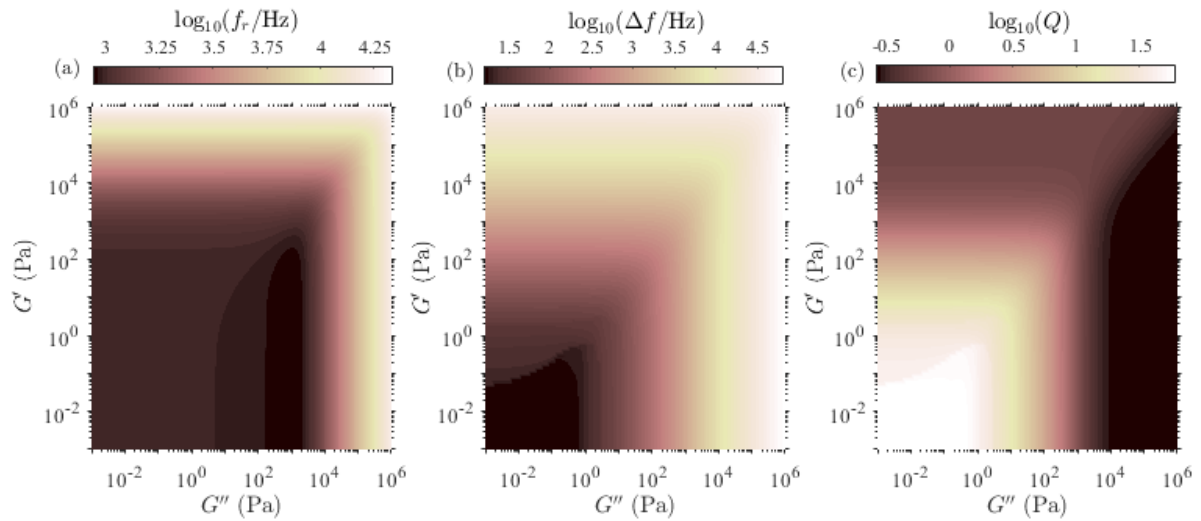


Figure A.6: Surface plots showing (a) the resonant frequency  $f_r$ , (b) the full width at half maximum  $\Delta f$ , and (c) the quality factor  $Q$  vs.  $G'$  and  $G''$ .

resonance curves from Eq. A.1 with  $a, b, c$ , and  $d = 0$ ,  $f_0 = 1000$  Hz, and for values of both  $G'$  and  $G''$  ranging from  $10^{-3}$  to  $10^6$  Pa. Surface plots showing the dependence of  $f_r$ ,  $\Delta f$ , and  $Q$  on  $G'$  and  $G''$  are shown in Fig. A.6. Darker colours show lower values, and lighter colours show higher values. As  $G''$  increases for fixed  $G'$ ,  $f_r$  decreases, reaches a minimum, then increases again. This is easiest to see in Fig. A.6 (a) for  $G' < 10^3$  Pa, however  $G''$  reaches a minimum for higher values of  $G'$  as well. For  $G' \lesssim 10^0$  Pa,  $\Delta f$  decreases to a minimum as  $G''$  increases, before increasing at higher  $G''$ . For higher values of  $G'$ ,  $\Delta f$  increases monotonically as  $G''$

is increased. Similarly, for  $G' \lesssim 10^0$  Pa,  $Q$  increases to a maximum before decreasing as  $G''$  increases. For higher values of  $G'$ ,  $Q$  decreases monotonically. In contrast, for fixed  $G''$ ,  $f_r$  and  $\Delta f$  increase as  $G'$  increases, while  $Q$  decreases. Although the surfaces for  $f_r$  and  $\Delta f$  look approximately symmetric about the line  $G' = G''$  for larger values of  $G'$  and  $G''$ , the subtle differences alluded to above are clearly visible in the plot of  $Q$ . These results suggests we should, at least in principle, be able to uniquely determine  $G'$  and  $G''$  from measurements of the resonance curve of our vibrating-wire rheometer in a viscoelastic fluid.

## Bibliography

- [1] E. W. Lemmon, M. O. McLinden, and D. G. Friend. Thermophysical properties of fluid systems. In *NIST Chemistry WebBook, NIST Standard Reference Database Number 69*. National Institute of Standards and Technology, Gaithersburg, MD, 20899, (retrieved July 8, 2018).

## Appendix B

# Vibrating-wire Rheometry of Aqueous Solutions of Pluronic F127

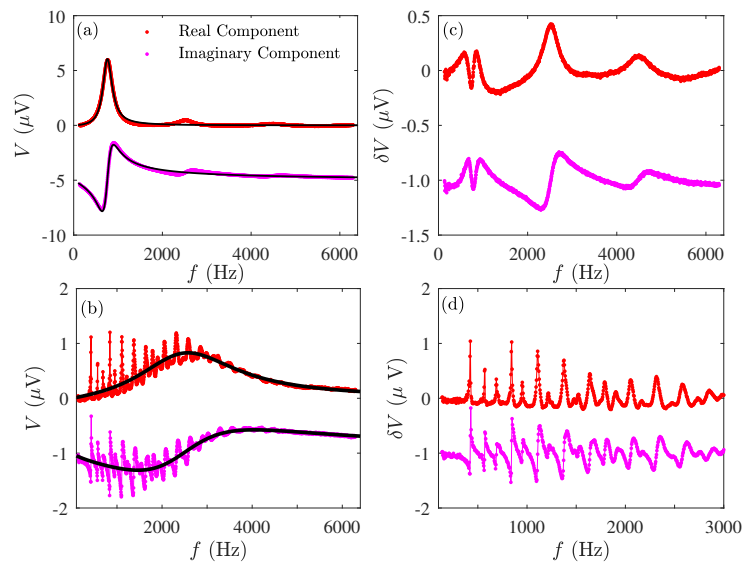


Figure B.1: Fits of the real and imaginary components of Eq. A.1 (black curves) to the real and imaginary components of the measured voltage of the 6 cm wire vibrating in the 18 wt.% Pluronic solution at (a)  $T = 20\text{ }^{\circ}\text{C}$  and (b)  $T = 35\text{ }^{\circ}\text{C}$ . (c) and (d) show the difference  $\delta V$  between the data and the fit at the same temperatures as (a) and (b), respectively. The imaginary component of the measured voltage, fit, and the resulting  $\delta V$  have been artificially shifted to lower voltage for clarity. Note that in subplot (d) only the data for  $f < 3000$  Hz are shown to emphasize the low-frequency peaks.

In this Appendix we present measurements of the viscoelastic moduli of aqueous solutions

of Pluronic F127 using the vibrating-wire rheometer described in Chap. 2. As in Chap. 4, we studied Pluronic solutions with concentrations of 14, 16, 18, and 20 wt.% at temperatures from 10 to 85 °C. We measured the voltage resonance curves using a vibrating-wire rheometer with a length of 6 cm. The temperature was varied using a temperature-controlled circulating bath and measured using a thermistor placed in the fluid circulating around the sample vial. The temperature was raised from 10 to 85 °C, and then lowered back to 10 °C, in 5 °C steps with a waiting time of 60 min after each step. The amplitude of the alternating current passed through the wire was  $I \sim 2.5$  mA and the driving frequency was increased from 100 to 6400 Hz in 4 Hz steps.

Example resonance curves and fits of the viscoelastic form of Eq. A.1, as described in Chap. 2, to the data are shown in Fig. B.1. Data at  $T = 20$  °C, in the sol state, are shown in Fig. B.1 (a), while Fig. B.1 (b) shows data at  $T = 35$  °C, in the gel state. The data shown are representative of the measured resonance curves and the quality of the fits obtained at all temperatures within the sol and gel states. Details of the curve fitting procedure used for these data are discussed in more detail below. At both of the temperatures shown in Fig. B.1 the quality of the fits is excellent. At  $T = 20$  °C, in the low-temperature sol state (Fig. B.1 (a)), the frequency of the largest resonant peak is  $f_r \sim 770$  Hz. At least two additional resonance peaks can be seen at higher frequencies, however. These higher-frequency resonance peaks are seen more clearly in Fig. B.1 (c), where we have plotted the difference between the measured data and the fit,  $\delta V$ . The increase in  $\delta V$  seen for  $f > 6000$  Hz may be the start of a fourth resonance that peaks at a higher frequency. The second resonance peak occurs at approximately 2500 Hz, and the third at approximately 4500 Hz. These frequencies are not exactly integer multiples of  $f_r$ , but they are close to  $3f_r$  and  $6f_r$ , respectively, suggesting that they may be due to higher harmonics of the vibrating wire. The deviation from exact multiples of  $3f_r$  and  $6f_r$  may be a consequence of the clamped ends of the wire. Although we did not analyze these additional resonances, understanding their origin may be an interesting topic for future work. For example, they could be used to measure the viscosity or viscoelastic moduli of a fluid at multiple frequencies



using a single vibrating-wire rheometer.

At  $T = 35$  °C, in the gel state (Fig. B.1 (b)), the fit captures the measured broad resonance curve well, but there are significant deviations from the fit at lower frequencies.  $\delta V$  for these data is plotted in Fig. B.1 (d). Fig. B.1 (d) shows that the low-frequency scatter is not random, but is due to the presence of several small, narrow peaks superimposed on the broader resonance curve. Since these peaks were only observed when the Pluronic was in the gel state, they may be due to the elasticity of the gel. Again, we did not analyze these peaks in detail, and they may be an interesting topic for future research.

We initially tried fitting Eq. A.1 to the measured voltage using the same procedure as described in Chap. 2, but found that the curve fitting routine often returned unphysical results that depended significantly on the initial guesses for  $G'$  and  $G''$ . To resolve this, we modified the fitting routine so that the values of  $G'$  and  $G''$  were fixed, and fit for the other free parameters listed in Chap 2. We refer to this process as a restricted fitting routine below. We logarithmically varied  $G'$  from  $10^{-4}$  to  $10^6$  Pa, and  $G''$  from  $10^{-2}$  to  $10^6$  Pa and calculated the sum of the squared deviations  $\chi^2$  between the fit and the data for each pair of  $G'$  and  $G''$ . Surface plots of  $\chi^2$  vs.  $G'$  and  $G''$  for restricted fits of Eq. A.1 to the measured voltage resonance curves for  $T = 15$  to  $85$  °C are plotted in Fig. B.2. Darker blue indicates lower values of  $\chi^2$ , while the lighter yellow indicates higher values of  $\chi^2$ . At temperatures within the low and high-temperature sol states ( $T = 15, 20,$  and  $70 - 85$  °C),  $\chi^2$  reaches a global minimum for  $G' = 10^{-4}$  Pa and  $G'' \sim 100$  Pa, however there is a valley of low  $\chi^2$  that extends in the direction of increasing  $G'$  but for relatively constant  $G''$ . For  $T = 15$  °C, the valley changes direction and extends at relatively constant  $G' \sim 10^2$  Pa to lower  $G''$ . At the other temperatures, the  $\chi^2$  surface shows similar features as in the  $T = 15$  °C case; there is a valley that spans  $G' \sim 10^4$  Pa and  $10^{-2} < G'' \lesssim 10^5$  Pa, and  $G'' \sim 10^5$  Pa and  $10^{-4} < G' \lesssim 10^4$ . The complex topography of the  $\chi^2$  surfaces makes finding the global minimum with the curve fitting routine difficult. Poor initial guesses for  $G'$  and  $G''$  may trap the fitting algorithm in a local minimum. For all of the fits presented in this appendix, we first performed the restricted fitting routine and found

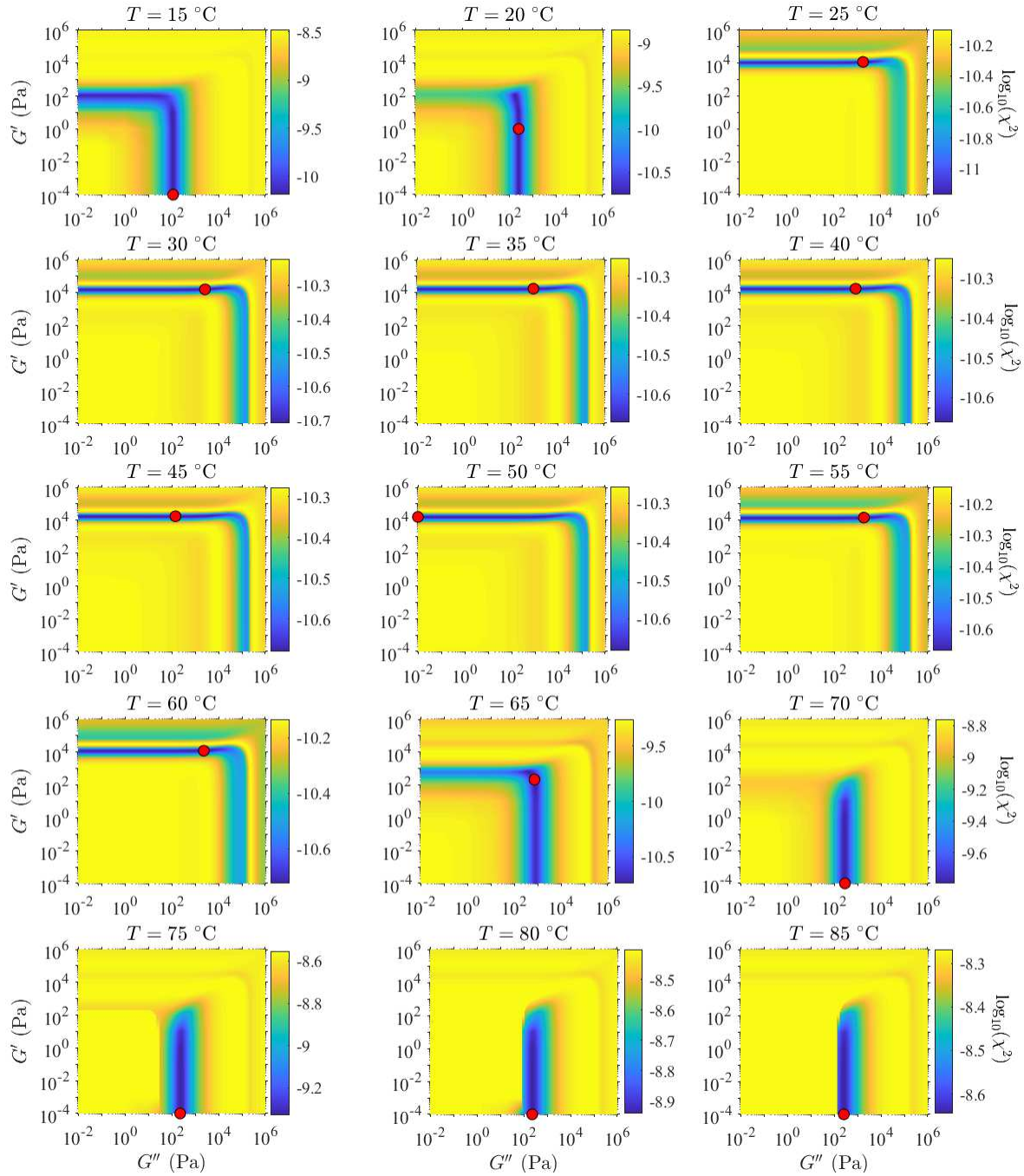


Figure B.2: Surface plots showing  $\chi^2$  vs.  $G'$  and  $G''$  from the restricted fitting routine described in the text of the imaginary component of Eq. A.1 to the imaginary component of the measured voltage of the 6 cm wire vibrating in the 18 wt.% Pluronic solution at temperatures spanning 15 to 85  $^\circ\text{C}$ , as labeled in the figure. The global minimum in each plot is marked with a red circle.

the global minimum. The values of  $G'$  and  $G''$  at the global minimum were then used as initial guesses in a subsequent unrestricted fit of Eq. A.1 to the data. In all cases, the value of  $\chi^2$

resulting from the unrestricted fitting process was less than or equal to the value of  $\chi^2$  obtained from the restricted fitting process.

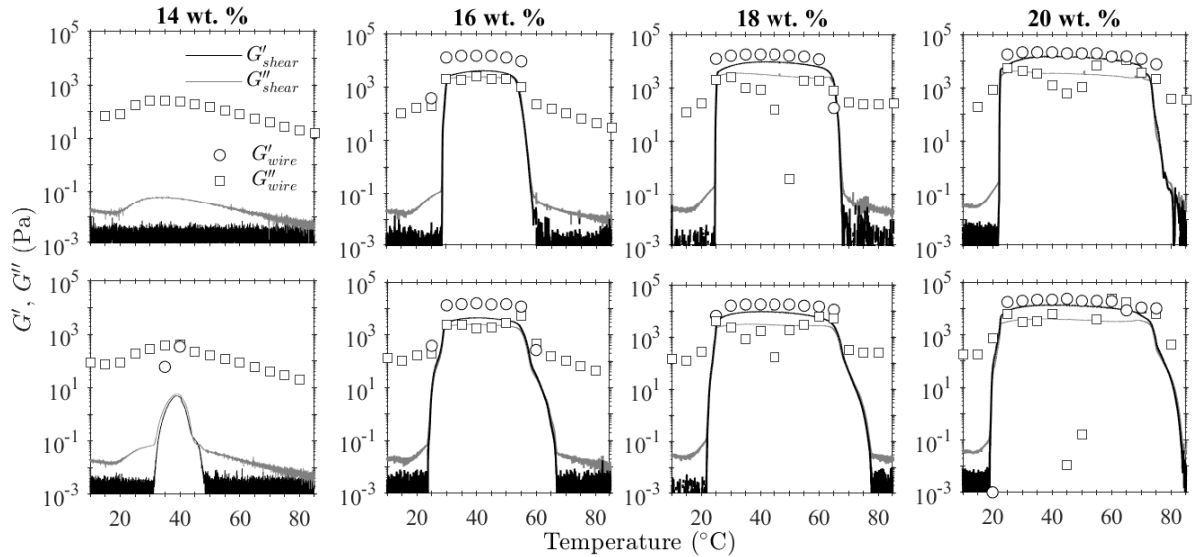


Figure B.3:  $G'_{wire}$  and  $G''_{wire}$  (symbols), measured using the vibrating wire as described in the text, and  $G'_{shear}$  and  $G''_{shear}$  (curves), measured using the shear rheometer as described in Chap 4, for aqueous solutions of Pluronic with concentrations 14, 16, 18, and 20 wt.%, increasing from left to right, while heating (top) and cooling (bottom).

The viscoelastic moduli measured using the shear rheometer,  $G'_{shear}$  and  $G''_{shear}$ , and the moduli measured using the vibrating-wire as described above, which we now denote  $G'_{wire}$  and  $G''_{wire}$ , are plotted against temperature and compared in Fig. B.3. The shear rheometer data in Fig. B.3 are the same data as presented in Chap. 4, with the addition of the data for 14 wt.%. As described in Chap. 4, the 14 wt.% solution does not gel on heating. Some elasticity is measured over a small range of temperature on cooling, but  $G'_{shear} < G''_{shear}$  at all temperatures. The moduli measured using the vibrating-wire rheometer show similar behaviour. On heating,  $G'_{wire} = 0$  and  $G''_{wire}$  follows a similar temperature dependence as  $G''_{shear}$ . On cooling,  $G'_{wire} = 0$  except at temperatures similar to where  $G'_{shear} > 0$ . At these temperatures,  $G'_{wire}$  is a few orders of magnitude larger than  $G'_{shear}$ . For concentrations greater than 14 wt.% and at temperatures where the Pluronic solutions are in the sol phase,  $G'_{shear}$  is small and  $G''_{shear} > 0$ . For the most part we find  $G'_{wire} = 0$  and  $G''_{wire}$  to be 3-4 orders of magnitude larger than  $G''_{shear}$  in these cases. The difference between  $G''_{shear}$  and  $G''_{wire}$  is likely due to the frequency dependence of  $G''$  and

is discussed more below. There is one exception to the above sol phase behaviour. For the 16 wt.% solution at  $T = 25$  °C when heating,  $G'_{wire} > G''_{wire}$  and both are smaller than in the gel phase. This may indicate that the Pluronic is undergoing a transition from sol to gel at this temperature, as discussed in Chap. 4. For the most part, at temperatures when the Pluronic solutions are a gel,  $G'_{wire} > G''_{wire}$  and  $G'_{wire} > G'_{shear}$ . For the 16 wt.% solution,  $G''_{wire}$  and  $G''_{shear}$  are similar. For the 18 and 20 wt.% solutions, there is some scatter in  $G''_{wire}$ , but for the most part the values are similar to  $G''_{shear}$ . The variability in  $G''_{wire}$  with temperature may be a fitting problem, resulting from the large regions of low  $\chi^2$  shown in Fig. B.2. The difficulty in finding the global minimum may be further affected by the additional peaks in the measured voltage when the Pluronic is a gel, as shown in Fig. B.1 (b) and (d).

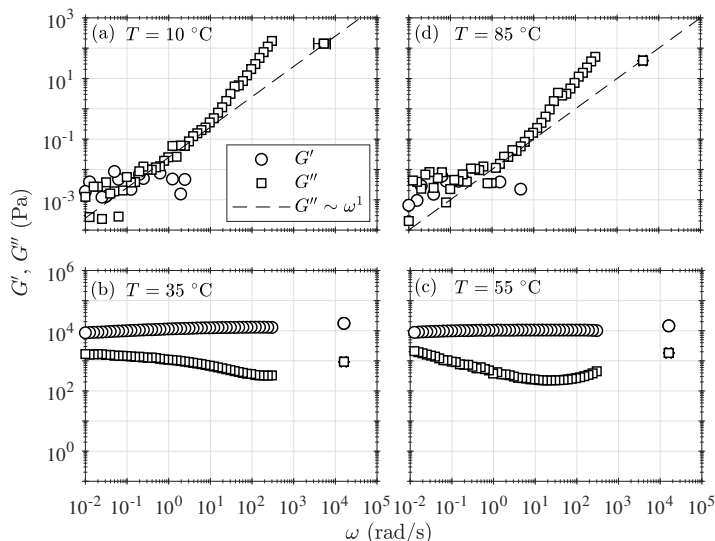


Figure B.4:  $G'$  and  $G''$  vs.  $\omega$  measured using the shear rheometer (data at  $\omega < 10^3$  rad/s) as described in Chap. 4, and the vibrating-wire rheometer (data at  $\omega > 10^3$  rad/s) at temperatures  $T =$  (a) 10, (b) 35, (c) 55, and (d) 85 °C. The error bars plotted for the high-frequency vibrating-wire data show the full width at half maximum of the resonance curves. Except in Fig. B.4 (a), the error bars are smaller than the data symbols. The dashed lines in (a) and (d) show  $G'' \sim \omega^1$ .

A comparison of the moduli measured using the vibrating-wire rheometer to the frequency dependence of  $G'$  and  $G''$  measured using the shear rheometer is shown in Fig. B.4 for  $T = 10, 35, 55,$  and  $85$  °C. The vibrating-wire data are plotted at the resonant frequency. The shear rheometer data in Fig. B.4 is the same data shown in Chap. 4. As discussed in Chap. 4, the

superlinear increase in  $G''_{shear}$  at higher frequency is due to the inertia limit of the rheometer and not the material properties. At low and high temperature, Pluronic solutions are expected to be Newtonian. For a Newtonian fluid,  $G' = 0$  and  $G'' \sim \omega^1$ . In Fig. B.4 (a) and (d),  $G'_{wire} = 0$  and  $G''_{wire}$  is consistent with a linear dependence on frequency extrapolated from the low-frequency shear rheometer data, which is plotted as a dashed line. In the gel phase (Fig. B.4 (b) and (c);  $T = 35$  and  $55$  °C,)  $G'_{wire}$  is slightly larger than what we would expect if  $G'$  was constant at high frequencies, but both  $G'_{wire}$  and  $G''_{wire}$  are consistent with what is expected based on an extrapolation of  $G'_{shear}$  and  $G''_{shear}$  to higher  $\omega$ .

# Curriculum Vitae

<b>Name:</b>	Cameron C. Hopkins	
<b>Post-Secondary Education and Degrees:</b>	University of Western Ontario London, Ontario, Canada, N6A3K7 2009 - 2013 B.Sc.	
	University of Western Ontario London, Ontario, Canada, N6A3K7 2013 - 2018 Ph.D.	
<b>Honours and Awards:</b>	Jackson Scholarship in Physics	2016
	NSERC PGS D	2016 – 2018
	Doctoral Excellence Research Award	2016 – 2018
	Ontario Graduate Scholarship	2015 – 2016
	Teaching Assistant Award of Excellence	2014 – 2015
	NSERC CGS M	2014 – 2015
	Queen Elizabeth II Graduate Scholarship	2013 – 2014
<b>Related Work Experience:</b>	Teaching Assistant The University of Western Ontario	2013 – 2018
<b>Conference Presentations:</b>	Cameron C. Hopkins, and John R. de Bruyn A transient study of the gelation of aqueous solutions of Pluronic F-127 using SAOS The Society of Rheology 89th Annual Meeting, Denver, Colorado, USA, 8-12 October 2017	

**Conference Presentations Continued:** Cameron C. Hopkins, Francesco del Giudice, John R. de Bruyn and Amy Q. Shen  
Vorticity Banding in Taylor-Couette flow of Graphene-Oxide Dispersions  
The Society of Rheology 89th Annual Meeting,  
Denver, Colorado, USA, 8-12 October 2017

Cameron C. Hopkins, and John R. de Bruyn  
Vibrating Wire Rheometry  
International Congress on Rheology,  
Kyoto Terrsa, Kyoto, Japan, 8-13 August 2016

John R. de Bruyn and Cameron C. Hopkins  
Vibrating Rheometry  
Viscoplastic fluids: from theory to application  
Banff International Research Station for Mathematical Innovation  
and Discovery,  
Banff, Alberta, Canada, 25-30 October 2015

John R. de Bruyn and Cameron C. Hopkins  
Development of a Vibrating Wire Rheometer  
CAP Congress  
University of Alberta, Edmonton, Alberta, Canada, 15-19 June 2015

Cameron C. Hopkins and John R. de Bruyn  
Development of a Vibrating Wire Rheometer  
CAMBR Distinguished Lecturer and Research Day  
University of Western Ontario, London, Ontario, Canada 27 April 2015

Cameron C. Hopkins and John R. de Bruyn  
An analytic solution to the problem of an oscillating plate in an  
Oldroyd-B fluid  
CAP Congress  
Université de Montréal, Montréal, Québec, Canada, 27-31 May 2013

## **Publications:**

Hopkins, C. C., de Bruyn, J. R. Numerical Simulations of the Forced Oscillations of a Wire in a Fluid. In Preparation.

Hopkins, C. C., Del Giudice, F., de Bruyn, J. R., and Shen, A. Q. Instability in Taylor-Couette flow of Graphene-Oxide Dispersions. In Preparation.

Hopkins, C. C., and de Bruyn, J. R. Gelation and Long-time Relaxation of Aqueous Solutions of Pluronic F127. In Preparation

Liu, Y., Hopkins, C. C., Handler, W. B., Chronik, B., de Bruyn, J. R. Rheology and heat transport properties of a polymer-based MRI tissue phantom. *Biomedical Physics & Engineering Express*, 3:045008, 2017

Hopkins, C. C., de Bruyn, J. R. Vibrating Wire Rheometry. *J. Non-Newtonian Fluid Mech.*, 238:205–211, 2016

Laschowski, B., Hopkins, C. C., de Bruyn, J. R., and Nolte, V. Modelling the deflection of rowing oar-shafts. *Sports Biomech.* 1:76–86 2017

Hopkins, C. C., and de Bruyn, J. R. The velocity field due to an oscillating plate in an Oldroyd-B fluid. *Can J. Phys.* 92:533–538 2014